Miniature Multiphoton Endoscopy Using Frequency-Doubled Er-Doped Fiber Laser

by

Lin Huang

B.Sc., Xi'an Jiaotong University, 2009

M.S., Xi'an Jiaotong University, 2012

A THESIS SUBMITTED IN PARTIAL FULFILLMENT OF

THE REQUIREMENTS FOR THE DEGREE OF

DOCTOR OF PHILOSOPHY

in

THE FACULTY OF GRADUATE AND POSTDOCTORAL STUDIES

(ELECTRICAL AND COMPUTER ENGINEERING)

THE UNIVERSITY OF BRITISH COLUMBIA

(Vancouver)

December 2018

The following individuals certify that they have read, and recommend to the Faculty of Graduate and Postdoctoral Studies for acceptance, the dissertation entitled:

Miniature Multiphoton Endoscopy Using Frequency-Doubled Er-Doped Fiber Laser

submitted by Lin Huang in partial fulfillment of the requirements for

the degree of Doctor of Philosophy

in The faculty of graduate and postdoctoral studies (Electrical & Computer Engineering)

Examining Committee:

Prof Shuo Tang

Supervisor

Prof Calum MacAulay

Supervisory Committee Member

Prof Lukas Chrostowski

Supervisory Committee Member

Prof Karen C. Cheung

University Examiner

Prof Keng Chou

University Examiner

Additional Supervisory Committee Members:

Prof Calum MacAulay

Supervisory Committee Member

Prof Lukas Chrostowski

Supervisory Committee Member

Abstract

Multiphoton microscopy (MPM) is a non-invasive, high-resolution imaging tool for visualizing tissues and organs. MPM uses femtosecond laser pulses to excite nonlinear signals from tissues and is capable of inherent optical sectioning. MPM systems have been mostly implemented using free-space optics and microscope platforms. For clinical applications, a compact fiber-optic MPM endoscopy with a miniature probe is needed for *in vivo* imaging.

In this thesis, I explore the potential of applying femtosecond fiber laser in MPM endoscopy. Femtosecond fiber laser has the advantages of compactness, robustness, and direct fiber-coupling. Challenges in developing the MPM endoscopy includes optimization of the laser source for highly efficient MPM excitation, managing femtosecond pulse delivery through optical fiber, and designing a miniature scanning probe. In this thesis, systematic design, optimization, and application of a miniature MPM endoscopy based on the frequency-doubled Er-doped fiber laser are conducted, and the challenges are addressed.

An Er-doped fiber laser operating at 1580 nm wavelength is developed and then frequency-doubled into ~790 nm wavelength to excite intrinsic two-photon excitation fluorescence signal from tissues. The frequency-doubling unit is integrated into the distal end of the miniature probe which is implemented by a miniature scanner and objective. The Er-doped fiber laser is directly fiber-coupled into the probe, making the system compact and portable.

Imaging speed of MPM endoscopy is critical for clinical applications. To increase the imaging speed, the laser is optimized to shorten its pulsewidth to 80 fs for increasing the multiphoton excitation efficiency. All-fiber dispersion compensation and pulse compression by single mode fiber are conducted. A fast MPM imaging speed at 4 frames/s is achieved.

Furthermore, the MPM endoscopy is applied for simultaneous two-photon and three-photon imaging. The fundamental laser pulse at 1580 nm and its frequency-doubled pulse at 790 nm are used as a dual-wavelength excitation source. Simultaneous imaging of two-photon excitation fluorescence, second harmonic generation, and third harmonic generation are achieved to acquire complementary information from tissues. Label-free multimodal imaging is demonstrated for biological tissues.

Through this study, the miniature MPM endoscopy using frequency-doubled Er-doped fiber laser is shown to have great potential for clinical applications.

Lay Summary

MPM is a non-invasive, high-resolution imaging tool for visualizing tissues and organs. However, benchtop MPM systems are bulky and costly. For *in vivo* imaging and clinical applications, a compact MPM endoscopy with a miniature probe is needed. Femtosecond fiber laser is a novel source for MPM endoscopy since it is compact, robust, and direct fiber-coupled. However, the potential of applying femtosecond fiber laser in MPM endoscopy has not been fully recognized.

Here a miniature MPM endoscopy with frequency-doubled Er-doped fiber laser is proposed. Systematic optimization of the laser is conducted to increase the imaging speed. All-fiber based pulse managing is conducted, making the laser and the miniature imaging head directly fiber-connected. Application of the MPM endoscopy with frequency-doubled Er-doped fiber laser for simultaneous, label-free two-photon and three-photon imaging is demonstrated. This study shows that miniature MPM endoscopy using frequency-doubled Er-doped fiber laser has great potential for clinical applications.

Preface

All the work presented henceforth was conducted in the Biophotonics Laboratory at the University of British Columbia (Vancouver campus). All the tissue imaging experiments were approved by the University of British Columbia's committees on human ethics and biosafety [certificate H16-02503 and B17-0066].

A version of Chapter 2 has been published in the following journal papers:

1. **Lin Huang**, Arthur K. Mills, Yuan Zhao, David J. Jones, and Shuo Tang, "Miniature fiber-optic multiphoton microscopy system using frequency-doubled femtosecond Er-doped fiber laser". Biomedical Optics Express **7**, 1948-1956 (2016).
2. Yuan Zhao, Mingyu Sheng, **Lin Huang**, and Shuo Tang, "Design of a fiber-optic multiphoton microscopy handheld probe". Biomedical Optics Express **7**, 3425-3437 (2016).

Materials in Chapter 2 have also been published in the following conference papers:

3. **Lin Huang**, Arthur K. Mills, David J. Jones, Yuan Zhao, and Shuo Tang, "Compact multiphoton microscopy system based on frequency-doubled femtosecond erbium-doped fiber laser". Optics in the Life Sciences (Optical Society of America 2015), JT3A-9 (2015).
4. **Lin Huang**, Shaupoh Chong, Arthur K. Mills, David J. Jones, Shuo Tang, "Multiphoton microscopy using frequency-doubled compact femtosecond erbium-doped fiber laser". Photonics West 2014, SPIE, 8948-26 (2014).

In the first-author journal paper and conference papers [1, 3, 4], I was the lead investigator, responsible for all major areas of concept formation, experiment, data collection, and analysis, as well as manuscript composition. Dr. Yuan Zhao was involved in the mechanical design of the handheld probe packaging. Dr. Shaupoh Chong, Dr. Arthur K. Mills, and Dr. David J. Jones were involved in the design of the laser oscillator. Dr. Shuo Tang was the supervisory author on this project and was involved throughout the project in concept formation and manuscript composition. In the third-author journal paper [2], I designed the optics setup and conducted the resolution test and also involved in assembling the handheld probe.

A version of Chapter 3 has been submitted in the following paper:

5. **Lin Huang**, Xin Zhou, and Shuo Tang, "Optimization of frequency-doubled Er-doped fiber laser for miniature multiphoton endoscopy". Journal of Biomedical Optics (Accepted).

I was the lead investigator, responsible for all major areas of concept formation, experiment, data collection, and analysis, as well as manuscript composition. Xin Zhou was also involved in the optical alignment. Dr. Shuo Tang was the supervisory author on this project and was involved throughout the project in concept formation and manuscript composition.

A conference abstract based on Chapter 4 has been accepted, and a full-length journal manuscript has been prepared.

6. **Lin Huang**, Min Ai, Xin Zhou, and Shuo Tang, "Simultaneous two-photon and three-photon microscopy imaging with a dual-wavelength Er-doped fiber laser". Photonics West 2019, SPIE, 10882-84 (2019).

I was the lead investigator, responsible for all major areas of concept formation, experiment, data collection, and analysis, as well as manuscript composition. Min Ai was also involved in the numerical simulation. Xin Zhou was also involved in the optical alignment. Dr. Shuo Tang was the supervisory author on this project and was involved throughout the project in concept formation and manuscript composition.

In addition, I also made contributions in the following joint publication:

- Spencer A. Freeman, Sonja Christian, Pamela Austin, Irene Iu, Marcia L. Graves, **Lin Huang**, Shuo Tang, Daniel Coombs, Michael R. Gold, and Calvin D. Roskelley. "Applied stretch initiates directional invasion through the action of Rap1 GTPase as a tension sensor". Journal of Cell Science **130**, 152-163 (2017).

In this project, I conducted nonlinear microscopy imaging of the samples using the benchtop MPM system in the Biophotonics Laboratory.

Table of Contents

List of Tables

List of Figures

List of Abbreviations

CM	Confocal microscopy
DCPCF	Double cladding photonic crystal fiber
DCF	Dispersion compensating fiber
EDF	Er-doped fiber
EDFA	Er-doped fiber amplifier
FAD	Flavin adenine dinucleotide
FOV	Field of view
FV	Fluorescence visualization
FWHM	Full-width-half-maximum
GFP	Green florescence protein
GRIN	Gradient-index
GVD	Group velocity dispersion
MEMS	Micro-electro-mechanical system
MMF	Multimode fiber
MPM	Multiphoton microscopy
NA	Numerical aperture
NADH	Nicotinamide adenine dinucleotide hydrogen
NIR	Near-infrared
OPO	Optical parametric oscillator
PBF	Photonic bandgap fiber
PBS	Polarization beam splitter

PM	Polarization-maintaining
PMT	Photomultiplier tube
PPLN	Periodically poled $MgO:LiNbO_3$
PSF	Point spread function
PZT	Piezoelectric tube
QPM	Quasi-phase matching
SHG	Second harmonic generation
SMF	Single mode fibers
SNR	Signal to noise ratio
SPM	Self-phase modulation
THG	Third harmonic generation
TPEF	Two-photon excited fluorescence
UV	Ultraviolet
2D	Two-dimensional
2PM	Two-photon microscopy
3D	Three-dimensional
3PEF	Three-photon excitation fluorescence
3PM	Three-photon microscopy

Acknowledgements

I offer my enduring gratitude to my supervisor Prof. Shuo Tang for giving me this opportunity to study at UBC ECE and her constant patience in providing guidance during my Ph.D career. She has enlarged my vision of science and provided coherent answers to my endless questions.

Special thanks to Prof. Alfred Leitenstorfer at the University of Konstanz for his valuable advice. I also thank Prof. David J. Jones and Dr. Arthur K. Mills for their tremendous help and discussion. I would also like to thank the Centre for Disease Modeling and Animal Care Services for providing the animal tissue samples.

I would like to thank my committee members, Prof. Calum MacAulay and Prof. Lukas Chrostowski for their helpful advices and suggestions on my dissertation.

In addition, I would like to thank all members (past and present) in the Biophotonics Laboratory at UBC for a pleasant time and excellent collaborations. The following listing order is based on the time sequence that I met with each of them. They are: Yifeng Zhou, Jiali Yu, Leo Pan, Tom Lai, Shaupoh Chong, Mengzhe Shen, Myeong Jin Ju, Min Ai, Weihang Shu, Yuan Zhao, Mingyu Sheng, Xin Zhou, Jiayi Cheng, Yonghan Zhou, and Ruochen Wen from UBC ECE.

I extend my thanks and gratitude to all the friends both in Canada and China for your genuine help and accompany. And most importantly, special thanks are owed to my parents and parents-in-law,

who have always been my eternal cheerleaders. Even though I was not able to company them, they have given me emotional support and financial assistance.

Finally, last but by no means least, I wish to thank my loving and supportive husband, Dr. Shu Lin, who has been in a long-distance relationship with me during the last six years and brought hope and expectation in my entire life.

Dedication

To all the people who help the little girls to pursue and achieve their own dreams.

To all the female who believe and pursue their abilities in science and engineering.

To everyone in my life who touches my heart.

Chapter 1: Introduction and Overview

1.1 Introduction of multiphoton microscopy

Optical imaging is capable of high-resolution imaging of cell morphology and metabolism. It can provide molecular specificity because tissue autofluorescence can be used to distinguish metabolic cellular components and proteins, such as nicotinamide adenine dinucleotide hydrogen (NADH), flavin adenine dinucleotide (FAD), and elastin. Normal tissue and cancerous tissue can be distinguished based on their biochemical and metabolic properties which can be measured by optical imaging. Therefore, optical imaging is a promising tool for diagnosing and treating cancer from the molecular level.

Multiphoton microscopy (MPM) is a non-invasive and high-resolution optical imaging technique, which is based on exciting and detecting nonlinear optical signals from biological tissues [1-5]. Typical MPM uses femtosecond laser pulses to excite nonlinear signals such as two-photon excited fluorescence (TPEF) and second harmonic generation (SHG) from tissue [2]. MPM is capable of depth-resolved imaging because the excitation of nonlinear signals happens only within the focal volume of the laser beam. It is a functional imaging technique in which the contrast from NADH, FAD, elastin, and collagen is biochemically specific. In 1931, the concept of two-photon absorption was first theoretically proposed by Goeppert-Mayer [6]. In 1990, the first TPEF microscope was developed by Winfried Denk *et al*. to demonstrate depth-resolved imaging on live cells [1]. SHG was first demonstrated by Peter Franken *et al*. in 1961 [7]. In 1986, the first biological SHG images were reported by Freund Isaac *et al*. to show the orientation of collagen fibers in rat tail tendon [8]. To date, MPM has been widely used in a variety of fields, featuring in neurology [9, 10] and cancer research [11, 12]. Current MPM systems have been mostly

implemented based on free-space optics and microscope platforms. Thus the overall size of the whole system is very bulky. Recently, new advances in MPM have demonstrated portable and miniaturized MPM endoscopes for *in vivo* imaging and clinical applications, where light can be delivered through a flexible fiber and images can be acquired using a miniature probe [13-18].

1.2 Basic principles of MPM

MPM excites nonlinear optical signals as an imaging contrast mechanism. When a material interacts with an intense laser beam, the material will generate a nonlinear response according to the strength of the applied electric field. In general, the induced polarization of the material subjected to the electric field can be expressed as [19]

$$P = \chi^{(1)}E^1 + \chi^{(2)}E^2 + \chi^{(3)}E^3 + ... \tag{1.1}$$

where P represents the induced polarization, E represents the electric field vector, $\chi^{(1)}$ is the first order susceptibility, and $\chi^{(n)}$ is the n^{th}-order nonlinear susceptibility for $n \geq 2$. The high-order nonlinear susceptibilities are usually very small.

TPEF is one type of multiphoton absorption where a molecule absorbs two low energy photons quasi-simultaneously ($10^{-15} \sim 10^{-18}$ s) and emits a single photon during relaxation from the excited state to the ground state. The time-averaged TPEF intensity excited by femtosecond pulse can be described by [20]

$$\langle I_{TPEF} \rangle \cong \delta_2 \eta \frac{P_{ave}^2}{\tau_p f_p} \left(\frac{\mathrm{NA}^2}{hc\lambda} \right)^2 \tag{1.2}$$

where δ_2 is the two-photon absorption cross-section, P_{ave} is the average laser power, τ_p is the pulse duration, f_p is the repetition rate of the laser, η is the fluorescence quantum yield, NA is the

numerical aperture of the objective lens, λ is the excitation wavelength, h and c are Planck's constant and the speed of light in vacuum, respectively. TPEF signal derives from intrinsic autofluorescence sources, such as elastin, NADH, and flavins, and exogenous fluorophores, such as various fluorescent dyes conjugated to molecular probes [21, 22]. The intrinsic TPEF signal can be observed from cells, collagen, and elastin fibers. Using exogenous probes, TPEF can image targeted subcellular components and specific proteins. TPEF is a major contrast signal in MPM. The one-photon absorption peak of NADH and elastin ranges from 340~360 nm, and the one-photon absorption peak of flavins ranges from 370~390 nm [23]. Their two-photon absorption spectra display flatter changes and the maximum absorption is usually between 700~800 nm [24]. Within this wavelength range, tissue scattering is lower than that in the visible range. Therefore, 700~800 nm is usually used as the excitation wavelength for intrinsic TPEF signal in tissue.

In SHG, two photons with the same frequency interact with a nonlinear material to induce frequency doubling and generate a photon with exactly twice the energy of the excitation photons. The second-harmonic intensity can be described by [3]

$$\langle I_{SHG} \rangle \propto \left(\chi^{(2)} \right)^2 \frac{P_{ave}^2}{\tau_p f_p} \tag{1.3}$$

where $\chi^{(2)}$ is the second-order nonlinear susceptibility as in Eq. (1.1), P_{ave} is the average laser power, τ_p is the pulse duration, and f_p is the repetition rate of the laser. SHG requires intense laser light passing through a highly polarizable material with a non-centrosymmetric molecular structure [3]. In tissue, collagen has been found to be a main tissue component that can generate SHG contrast. Therefore, SHG is especially useful for imaging cartilage, bone, tendon, skin and cornea [3, 4], where collagen is the most abundant extracellular matrix protein in the tissues.

Third harmonic generation (THG) is a nonlinear scattering process where three near-infrared (NIR) photons are converted into a single (visible) photon with exactly three times the incident photon energy. THG intensity depends on the third-order nonlinear susceptibility and cubically on the average laser power. It is a label-free imaging which is generated from optical heterogeneities [25], such as at the interface between an aqueous medium and a lipidic, mineralized, or absorbing structure [26]. THG signal is more versatile compared to SHG and TPEF signals since it does not require the non-centrosymmetric structure as in SHG or fluorescence molecule as in TPEF.

The energy diagrams of TPEF, SHG, and THG are illustrated in Figs. 1.1(a)-1.1(c). In TPEF, a susceptible molecule absorbs two low energy photons in the NIR region and is excited from ground state to a real excited state. When the molecule returns to the ground state, it emits a fluorescence photon, which has slightly lower energy than the sum of the two excitation photons due to the energy loss in the relaxation. Therefore, TPEF signal has a frequency that is less than the doubled-frequency of the incident light. In SHG, a molecule interacts with two photons simultaneously through nonlinear scattering and generates an SHG photon with exactly twice the energy of the excitation photon. Therefore, SHG signal has a frequency that is the exactly doubled-frequency of the incident light. THG is also a nonlinear scattering and its frequency is three-times that of the incident light. Since TPEF, SHG, and THG have different frequencies, they can be separated using dichroic mirrors and filters.

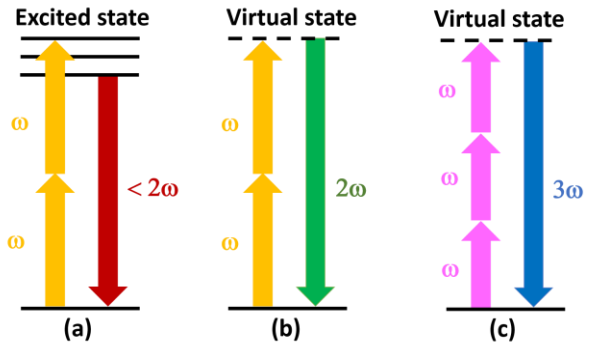

Figure 1.1 The energy diagrams of TPEF (a), SHG (b), and THG (c).

MPM is based on nonlinear excitation which offers a key advantage for imaging within strongly scattering biological tissue: depth sectioning without the use of confocal pinholes for rejecting out-of-focus signal (inherent optical sectioning) [27]. Such advantage gives MPM an indispensable role in high-resolution imaging of physiology, morphology and cell-cell interactions in intact tissues or live animals [2]. MPM requires high photon density for efficient excitation because the probability of a molecule absorbing two photons simultaneously is very low. A high numerical aperture (NA) objective lens is used to tightly focus the photons to a very high density within the focal volume. Efficient excitation only happens at the focal volume. Therefore, MPM has inherent optical sectioning capability and is capable of depth-resolved imaging.

Another important advantage of MPM comes from the use of NIR excitation. Using NIR excitation, photo-damage is highly reduced and cell viability is increased compared with ultraviolet (UV) or blue light excitation. Additionally, NIR light can penetrate deeper into scattering tissue than visible or UV light because of the reduced scattering. MPM has reduced background signal compared with one-photon imaging. In MPM, the excitation wavelength and emission wavelength are separated far apart. With dichroic mirrors and bandpass filters, the emitted photons can be separated from the excitation light. As such, MPM has a very low

background noise and high signal-to-noise ratio (SNR). In addition, MPM can detect intrinsic contrasts within biological tissues, allowing label-free imaging. Therefore, MPM has outstanding capability of high-resolution imaging of thick tissues and live cells.

1.3 MPM instrumentation

A typical configuration of MPM system is shown in Fig. 1.2. A Ti:Sapphire laser with femtosecond pulse output is used as the excitation source. The laser beam passes through a dispersion pre-compensation unit, which pre-compensates the dispersion from the objective lens and other optics in the delivery path. An XY scanner is used to perform raster scanning of the laser beam. The scanned laser beam is expanded by a pair of scan lens and tube lens to fill the back aperture of the high-NA objective lens. The objective lens delivers a tightly focused laser beam to the sample and also collects the MPM signals in the backward direction. The MPM signals are separated from the excitation beam by a dichroic mirror. The MPM signals can be further separated into different channels, such as TPEF and SHG channels by dichroic mirrors and bandpass filters. The TPEF and SHG signals are finally detected by photomultiplier tubes (PMT).

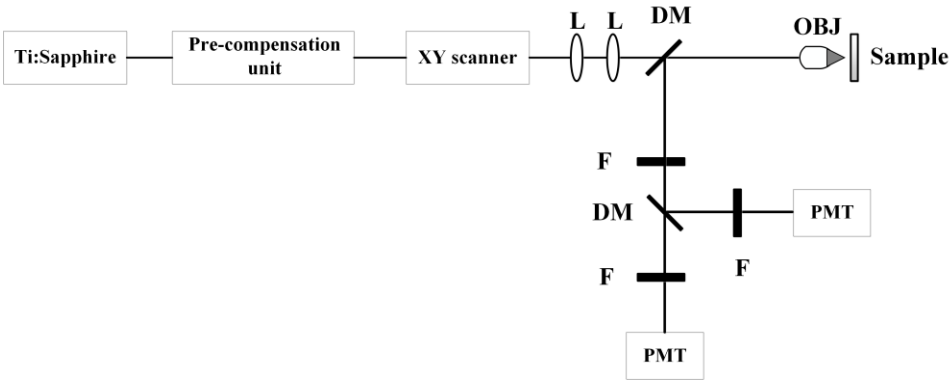

Figure 1.2 A typical configuration of an MPM system. L: lens; DM: dichroic mirror; F: filter; OBJ: objective lens; PMT: photomultiplier tube.

Since the excitation efficiency of TPEF and SHG is very low [19], femtosecond pulsed lasers with high peak power are used to excite the nonlinear signals. Usually, femtosecond lasers with 100-200 fs pulse duration are used as the excitation source. The femtosecond pulses can be broadened due to dispersion introduced by thick optical components in the beam path, including the beam expander lenses and an objective lens. Dispersion is more critical for shorter pulses. A dispersion pre-compensation unit is applied to achieve femtosecond pulse at the sample location for efficient MPM excitation. Dispersion pre-compensation can be achieved by prisms, gratings, and chirped mirrors [19].

An XY scanner performs raster scanning of the focal spot and acquires a 2D image. By scanning the objective lens up and down, depth scanning can be performed and 3D image stacks can be acquired. Raster scanning of the laser beam is usually achieved by galvanometer scanners. Resonant galvanometer scanner is capable for *in vivo* video rate MPM imaging due to its high scanning speed [28].

In MPM system, the spatial resolution including lateral and axial resolution is determined by the focusing capability. In general, the lateral resolution of one-photon microcopy based on Rayleigh criterion is $0.61\frac{\lambda}{NA}$ [29], where NA is the numerical aperture of the objective lens and λ is the excitation wavelength. The axial resolution of one-photon microcopy is $0.88\frac{\lambda}{n-\sqrt{n^2-NA^2}}$ [29], where n is the refractive index of the immersion medium (n = 1 for air and n = 1.33 for water immersion). In two-photon microscopy (2PM) and three-photon microscopy (3PM), due to the two-photon and three-photon interaction, the focal spot can be tighter. The resolution (both lateral

and axial resolution) of 2PM and 3PM could be $1/\sqrt{2}$ and $1/\sqrt{3}$ times better than the one-photon resolution, respectively [30, 31].

1.4 MPM endoscopy

MPM systems have been mostly developed based on free-space optics and microscope platforms, where the whole system is very bulky. Bench-top systems are not suitable for clinical applications due to their bulky size and non-flexible free-space optical design. For *in vivo* imaging and clinical applications, a fiber-optic based MPM endoscopy is needed where light can be delivered through a flexible fiber and images can be acquired using a miniature probe [32-34]. To translate the benchtop MPM into MPM endoscopy, the major challenges include designing a compact laser source for efficient MPM excitation, managing femtosecond pulse delivery through optical fiber, and designing a miniature scanning probe.

1.4.1 Laser source

The most commonly-used femtosecond laser in MPM is the solid-state mode-locked Ti:Sapphire laser [32-41]. The wavelength of Ti:Sapphire lasers can be tuned from 680-1080 nm to excite different fluorophores at their absorption peak [28]. The typical pulsewidth of a Ti:Sapphire laser is 100-200 fs. MPM excitation efficiency increases inversely with the pulsewidth [42]. Therefore, shorter pulses can excite MPM signals more efficiently than longer pulses. Ti:Sapphire laser outputs into free space and thus needs to be coupled into an optical fiber for developing MPM endoscopy. Furthermore, Ti:Sapphire laser is expensive, bulky, and requires precise alignment, which is not suitable for MPM endoscopy in clinical application.

Recently, femtosecond fiber lasers have also been used in MPM. The active gain medium in femtosecond fiber laser is an optical fiber doped with rare-earth elements such as erbium or ytterbium. The laser system consists of a fiber oscillator based on a ring fiber cavity and fiber amplifier pumped by laser diodes [43]. Femtosecond fiber laser is not only directly fiber connected, but also compact, not susceptible to alignment issues, and less costly. Two types of fiber laser, Yb-doped fiber laser operating at the 1030 nm region [44-46] and Er-doped fiber laser operating at the 1550 nm region [47], have emerged as promising excitation sources for MPM endoscopy. The advantage of the relatively long excitation wavelength is deep penetration due to considerably reduced scattering [40]. However, due to the relatively long excitation wavelengths of the fiber lasers, they cannot excite intrinsic TPEF signal from native tissue constituents, such as NADH and FAD. Fluorescence staining is usually required to generate TPEF contrast at the long excitation wavelength [24], which is not suitable for *in vivo* imaging. More detailed review of the relevant MPM endoscopy systems using Ti:Sapphire laser and femtosecond fiber lasers is described in Chapters 2 and 3.

1.4.2 Pulse delivery

Delivering femtosecond pulses through optical fiber is challenging because the femtosecond pulses inevitably suffer from temporal and spectral distortion due to dispersion and self-phase modulation (SPM). Dispersion happens when light propagates through optical materials, such as optical fiber or optical lenses. It could broaden femtosecond pulses into picosecond pulses. SPM is a nonlinear effect where a varying refractive index is induced by high-intensity pulses [48]. SPM depends on the intensity and is inversely proportional to the square of the fiber diameter. Therefore, increasing the fiber diameter could dramatically reduce the effect of SPM.

Several groups have used double cladding photonic crystal fiber (DCPCF) in MPM endoscopy systems [17, 18, 45]. In DCPCF, femtosecond pulses are delivered by the single mode core and MPM signals are collected by the multimode inner cladding. The large core diameter of DCPCF greatly reduces SPM, and its high NA cladding provides high collection efficiency. However, similar to single mode fiber (SMF) which has normal dispersion of +0.036 ps^2/m at 800 nm, DCPCF also suffers from severe pulse broadening. For an unchirped Gaussian input pulse of the form $\exp\left\{-t^2/t_p^2\right\}$, the group velocity dispersion (GVD) of a dispersive medium is $\psi_2 = \beta_2 L$ which is second-order dispersion, and here β_2 is the GVD parameter and L is the length. The pulsewidth broadening induced by GVD is $\frac{t_{out}}{t_p} = \sqrt{1+\frac{4\psi_2^2}{t_p^4}}$ [49]. Anomalous dispersion ($\beta_2 < 0$) is introduced by a free-space pre-compensation unit such as grating pair to balance the normal dispersion ($\beta_2 > 0$) from DCPCF. However, this approach limits the compactness and portability of such MPM systems.

Other groups have used hollow core photonic bandgap fiber (PBF) for femtosecond pulse delivery [18, 41, 44]. It relies on strict photonic bandgap created by micro-structured cladding to confine light in a low-refractive-index air core. Since light propagates in the air core, the effect of material nonlinearities is insignificant and the material dispersion in PBF is almost negligible at the design wavelength. A typical commercial hollow core PBF (HC-800-02, Thorlabs) has nearly zero dispersion at ~775 nm. However, the propagation bandwidth of PBF is limited which is not suitable for delivering broadband ultrashort pulses. More detailed review of the relevant MPM endoscopy systems using different delivery fibers is described in Chapters 2 and 3.

1.4.3 Probe miniaturization

To perform MPM imaging on patient, an endoscope or handheld imaging probe is needed. Several groups have developed MPM endomicroscopes or compact systems. JenLab (Germany) has developed MPTflex, a system using articulated mirror arm for imaging skin [50]. It was the first commercial MPM system used on patients. The imaging speed was 0.2 frames/s, and magnetic ring and double-sided tape to reduce skin movement were utilized to reduce motion artifacts. However, the articulated mirror arm is rigid and bulky, which limits its application in imaging the oral mucosa or internal organs.

The Xingde Li group at Johns Hopkins University has built a small imaging head with piezoelectric tube (PZT) scanner [32]. They achieved imaging speed of 2.7 frames/s and applied the device to image *ex vivo* cervical tissues for studying premature birth. PZT scanner has a small diameter, but it has a long and rigid length. The overall dimension of their probe is 2 mm × 32 mm (diameter × length), with a peak-to-peak driving voltage of approximately 50–140 V.

The Chris Xu group at Cornell University used piezoelectric actuators or bimorphs and gradient-index (GRIN) lens to build a small imaging head, which has an outside diameter of 3 mm and a rigid length of 4 cm [33]. They achieved a speed of 4.1 frames/s. GRIN lens has a small diameter and cylindrical geometry. However, it suffers from severe chromatic aberration and causes a considerable focal shift between the excitation wavelength (NIR) and the MPM signal wavelength (visible).

Other groups including our group have developed MPM endomicroscope using micro-electro-mechanical system (MEMS) scanners [18, 34, 51]. MEMS scanners have a small size and high-quality beam steering. Typically, a MEMS mirror has a diameter of 0.5 mm to a few millimeters, which has great potential to be integrated into a compact imaging probe. MEMS can

be operated in a raster scanning mode where the beam position is determined by the driving voltage. When the MEMS scanner is driven by raster scanning, the speed is limited to several hundred Hertz. The scanning speed can be increased at the cost of reduced MEMS mirror size or scanning angle, which then reduces the field-of-view (FOV).

1.5 Clinical application

A potential application of MPM endoscopy is to detect oral cancer. Oral cancer involves abnormal cell growth within the mouth, with the potential to invade or spread to other body locations. Each year 4,600 new cases in Canada and 300,000 cases worldwide are identified, and half of the patients, on average, die within 5 years of diagnosis [52-54]. In the current practice, clinicians check the oral mucosa for suspicious lesions using white light illumination and take biopsy samples from a suspicious region. Histopathologic analysis is then carried out to determine the presence and stage of oral cancer. Even though histopathology is regarded as the gold standard of cancer diagnosis, the biopsy procedure is time-consuming, uncomfortable, and expensive, and frequently the biopsied lesions are benign lesions.

A technology for oral cancer screening is fluorescence visualization (FV), such as VELscope (LED Dental Inc., BC, Canada), which can obtain direct visual impression of oral cavity fluorescence [54, 55]. Autofluorescence originates from a variety of fluorophores in the oral cavity, while oral cancer and precancer display a loss of autofluorescence. However, confounders, such as inflammatory lesions, also display a loss of autofluorescence. Therefore, FV has shown relatively high false positive rates from inflammation, infection, and trauma [56].

Confocal microscopy (CM) has also been applied to *in vivo* imaging of oral mucosa [57-59]. CM can perform depth-resolved imaging by using pinholes to reject out-of-focus light. In

reflectance CM [57, 58], scattered light is detected from the heterogeneity of optical refractive index. However, scattering is not biochemically specific and many structures in tissue can scatter light. In fluorescence CM [59], fluorescence signal is usually detected from exogenous staining. However, for *in vivo* imaging, the toxicity of staining is a big concern and only very limited dyes could be used on patients. Staining also limits the imaging depth because the dye can only penetrate ~50 μm from epithelium [60].

Due to its capability of imaging cells and extracellular matrix, MPM has been shown to be promising to detect oral cancer on animal models using hamster cheek pouch [61, 62]. However, there has been no MPM system that can be used on patients for detecting oral cancer. To check the capability of MPM on imaging oral mucosa, preliminary *ex vivo* imaging on human oral tissues are conducted on a benchtop MPM system [63]. Frozen sections of human normal and cancerous oral tissues are obtained from BC Cancer Agency Tumor Tissue Repository (BCCA-TTR). Fig. 1.3 shows the MPM images of normal tissue and invasive squamous cell carcinoma (SCC) from the floor of the mouth. The normal tissue is shown in the top row, which shows an intact basement membrane between epithelium cells and collagen fibers in the stroma. The tumor tissue is shown in the bottom row, which shows the invasion of cancer cells into stromal collagen. The preliminary study shows that normal and cancerous human oral tissues can be differentiated by MPM. To fulfill the capability and potential of MPM technology for clinical oral cancer detection, the benchtop MPM system needs to be translated into an MPM endoscopy.

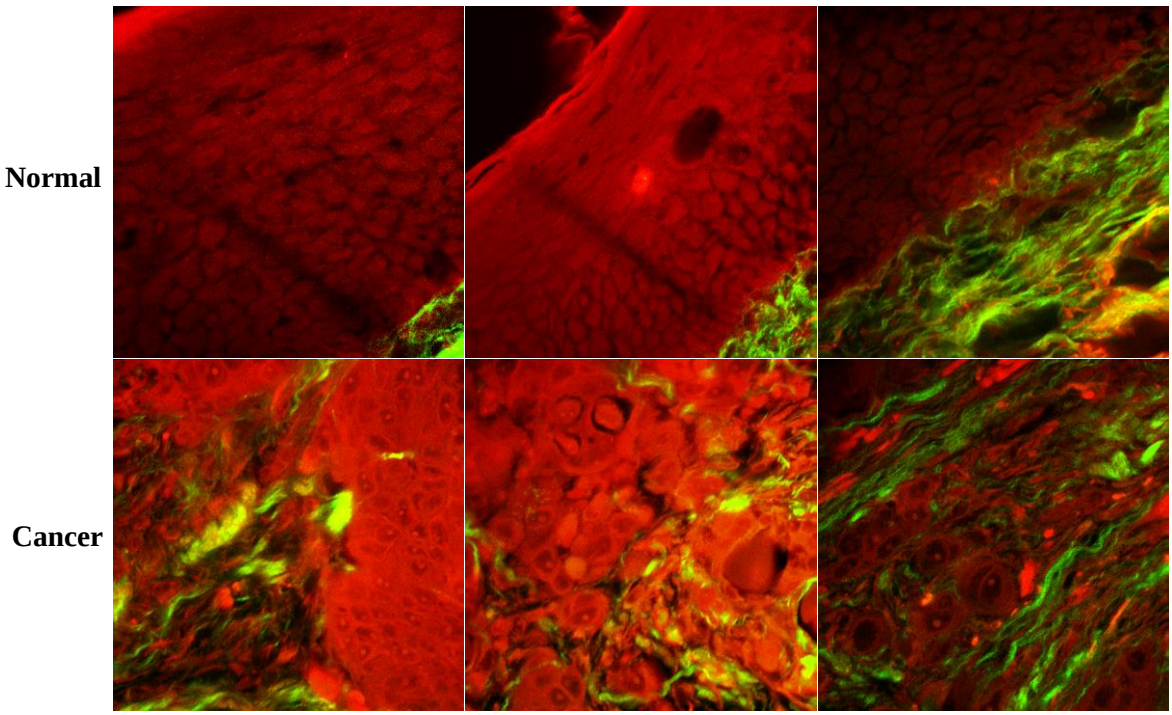

Figure 1.3 Multiphoton images of human oral tissue sections from the floor of mouth. TEPF in red and SHG in green. Top row, normal tissue, shows clear boundary between epithelium cells (red) and collagen fibers in stroma (green). Bottom row, invasive squamous cell carcinoma (SCC), shows invasion of cancer cells (red) into stromal collagen (green). FOV = 130 μm×130 μm.

1.6 Laser safety

Laser safety is an important issue when performing *in vivo* MPM imaging on patients. The American National Standards Institute (ANSI) laser safety [64] standards do not provide sufficient information on tissue damage when using focused femtosecond pulses. In this section, laser safety assessment based on photo-thermal damage [65] and photo-chemical damage [66] will be carried out.

To estimate the thermal damage due to the optical-thermal response of laser-irradiated tissue, the temperature rise can be determined by calculating the volumetric absorbed energy density. For a single pulse, the temperature rise is given by [65]

$$\Delta T = \frac{\mu_a E_p}{\rho C A} \tag{1.4}$$

where E_p is the energy per pulse, μ_a is absorption coefficient, ρ is mass density (1000 kg·m^{-3} for water), C is the heat capacity (4187 J·˚C^{-1}·kg for water), and A is the focal spot area. Since biological tissue is mostly composed of water, the mass density and heat capacity of water can be used to estimate the temperature rise in tissue. Blood is a major absorber in tissue and it has an μ_a of ~10 cm^{-1} at 800 nm wavelength [67]. For a series of pulses deposited into the focal volume, an equilibrium temperature is determined by energy deposition and heat diffusion. In the investigation by Vogel *et al*. [66], repeated pulses generate 6.8 times higher temperature rise in a tightly focused volume (NA = 1.3), and a 45-fold temperature increase when NA = 0.6, compared to a single pulse.

According to Eq. (1.4), the temperature rises from a single pulse at 800 nm wavelength are calculated for a typical benchtop MPM system with a high-NA microscope objective (NA = 1.3), and an MPM endoscopy with a moderate-NA, single-element, miniature objective (NA = 0.5). The results are shown in Table 1.1. Since the diffraction-limited spot radius estimated by Rayleigh criterion is $0.61\frac{\lambda}{\mathrm{NA}}$, the benchtop MPM has a focal spot radius of 0.38 μm, and the MPM endoscopy has a focal spot radius of 0.98 μm. Based on Eq. (1.4), at 50 mW average power on tissue and assuming μ_a =10 cm^{-1}, the temperature rise caused by a single pulse is calculated to be 0.34 ˚C and 0.08 ˚C for the benchtop MPM and MPM endoscopy, respectively. The benchtop MPM produces a higher temperature rise after a single pulse because the deposited energy is

focused tightly by a high-NA objective (a smaller focal spot area). Additionally, for a series of pulses, a 6.8-fold and 45-fold temperature rise than a single pulse is estimated for the NA = 1.3 and NA = 0.5 objectives, respectively [66]. When the focal volume is smaller, it allows faster heat diffusion in all directions. Considering the equilibrium between energy deposition and heat diffusion, the corresponding multiplication number for series of pulses with the high-NA objective is smaller than that with the moderate-NA objective. Thus, the temperature increase caused by a series of pulses is estimated to be 2.3 ˚C and 3.6 ˚C for the benchtop MPM and MPM endoscopy, respectively. Additionally, severe pain can be induced in human skin when the tissue temperature is elevated to 45 ˚C [68]. Therefore, focused femtosecond NIR pulses used in MPM hardly cause thermal damage, which matches with Vogel's calculation and conclusion that thermal damage can be ruled out at the power level used in MPM imaging [66]. Additionally, it can be seen from Eq. (1.4) that the temperature rise grows linearly with the pulse energy and absorption coefficient, and inversely with the focal spot area. When an Er-doped fiber laser at 1550 nm is directly used as the excitation wavelength in MPM, water is the main absorber which has an absorption coefficient of ~30 cm^{-1} at its absorption peak in the 1-2 μm region [64]. However, the focal spot radius will be nearly doubled due to the doubled wavelength compared to 800 nm. Therefore, the temperature rise at the 1550 nm wavelength should not be higher than that estimated for the 800 nm when the other conditions are the same.

When laser irradiates on tissue, photo-chemical damage could happen before photo-thermal damage occurs. According to Vogel *et al*. in Ref. [66], free-electrons and low-density plasma are generated in tissue when illuminated by high laser irradiance. Photo-chemical damage in tissue mainly includes: 1. Creation of reactive oxygen species through changes of the water molecules. Reactive oxygen species are known to cause cell damage. 2. Fragmentation of

biomolecules initiated by capturing of electrons into an antibonding molecular orbital. An optical breakdown irradiance threshold is defined, and in water the threshold is found to be $I_{th} = 6.54\times10^{12}$ W/cm^2 for 100 fs pulses [66]. Based on the irradiance level, different types of tissue damage could be induced as shown in Fig. 1.4. For example, the irradiance required for generating different types of damage is found to be ~0.067I_{th} for cell damage after scanning irradiation, and ~0.15I_{th} for intracellular dissection [66].

Table 1.1 Laser safety estimation for a typical benchtop MPM and MPM endoscopy.

	Benchtop MPM	**MPM endoscopy**
NA	1.3	0.5
Wavelength λ (nm)	800	800
Average power P_{ave} (mW)	50	50
Pulsewidth τ_p (fs)	100	100
Repetition rate f_p (MHz)	80	50
Temperature rise for single pulse ΔT (˚C)	0.34	0.08
Multiplication number for series of pulses	6.8	45
Temperature rise for series of pulses $\Delta T'$ (˚C)	**2.3**	**3.6**
Irradiance I_r (W/cm^2)	1.42×10^{12}	4.18×10^{11}
Irradiance threshold I_{th} (W/cm^2)	6.54×10^{12}	
$\boldsymbol{I_r / I_{th}}$	**0.22**	**0.06**

In Table 1.1, the laser irradiance at the focal volume is calculated and compared with the threshold. Irradiance is calculated as the peak power divided by the focal spot area *A*. For the benchtop MPM with 50 mW average power and NA = 1.3, the irradiance is found to be $0.22I_{th}$ which is larger than the values for cell damage and intracellular dissection. Thus, the average power in the MPM benchtop system should be kept below 15 mW to avoid cell damage. In the MPM endoscopy with 50 mW average power and NA = 0.5, the irradiance is found to be $0.06I_{th}$ which is close to the level for cell damage. The average power in the MPM endoscopy system (800 nm) should be kept below 50 mW to avoid cell damage. Higher average power can be applied to tissue at longer wavelength because the focal spot is larger and the irradiance is lower. When an Er-doped fiber laser at 1550 nm wavelength is directly used in MPM endoscopy, the average power in the MPM endoscopy system (1550 nm) should be kept below 200 mW to avoid cell damage.

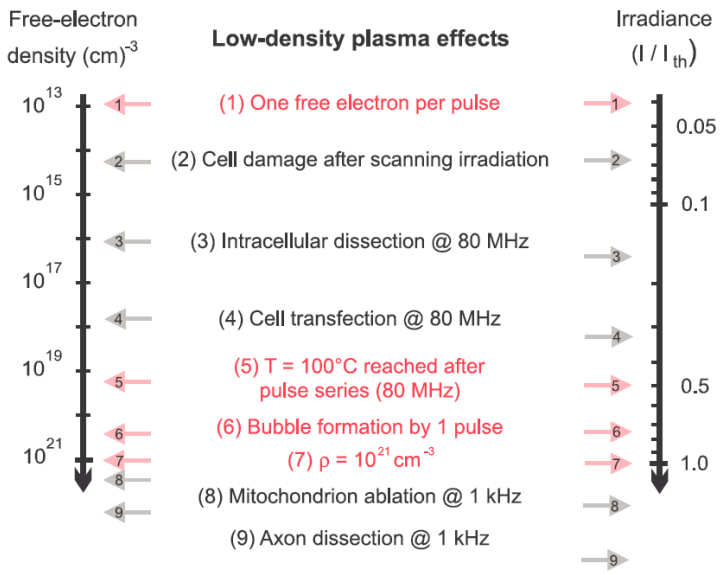

Figure 1.4 Variety types of tissue damage caused by high laser irradiance from femtosecond laser pulses [66].

1.7 Objectives and contributions

MPM is considered as one of the best noninvasive high-resolution imaging techniques for imaging thick tissues and live animals. Traditional MPM systems have been mostly implemented using free-space optics and microscope platforms. To translate the MPM technology for *in vivo* imaging and clinical applications, a compact fiber-optic MPM endoscopy with a miniature imaging probe is needed.

The main objective of this thesis is to investigate the potential of applying femtosecond fiber lasers to develop MPM endoscopy. There are several challenges in developing MPM endoscopy based on femtosecond fiber laser, including optimization of the laser source for high efficient MPM excitation, managing femtosecond pulse delivery through optical fiber, and designing a miniature imaging probe. In this thesis, systematic design, optimization, and application of miniature MPM endoscopy based on frequency-doubled Er-doped fiber laser are carried out, and the challenges are addressed.

The main contributions I have made include: (1) developed a novel MPM endoscopy based on frequency-doubled Er-doped fiber laser; (2) improved the imaging speed of the MPM endoscopy by systematic optimization of the frequency-doubling process of the fiber laser; (3) applied the optimized MPM endoscopy to simultaneous label-free two-photon and three-photon imaging.

First, we proposed a novel MPM endoscopy design based on frequency-doubled Er-doped fiber laser. An Er-doped fiber laser operating at 1580 nm was developed and then frequency-doubled into 790 nm to excite MPM signals. The 790 nm wavelength can excite intrinsic TPEF and SHG signals and no staining of tissue is required, which is critical for *in vivo* patient imaging. Frequency-doubling was achieved through a periodically poled MgO:$LiNbO_3$ (PPLN) which was

integrated inside the distal end of the imaging head. Thus the fiber laser was directly connected with the imaging probe via a SMF and there was no need for fiber re-coupling. By delivering the femtosecond pulse at 1580 nm, traditional SMF which has anomalous dispersion at this wavelength can be utilized to compensate the normal dispersion from Er-doped fiber (EDF). The length of the EDF and SMF were optimized to achieve all-fiber based dispersion control, and a compressed pulse was obtained at the output of the SMF. Our design enabled all-fiber connection and dispersion management, which made the system highly compact and portable.

Second, the fiber laser system and MPM endoscopy were optimized to increase the imaging speed which is critical for clinical applications. We optimized the laser system for reduced pulsewidth in order to increase the MPM excitation efficiency. Systematic optimization included investigation on the dependence of the PPLN length on the MPM excitation efficiency and manipulating the Er-doped fiber laser to match its bandwidth with the acceptance bandwidth of the PPLN. Through the optimization, pulsewidth of 80 fs was achieved for both the fundamental and frequency-doubted pulses. A 10-times increase of MPM imaging speed to 4 frames/s was demonstrated.

Third, we demonstrated multimodal MPM imaging including simultaneous two-photon microscopy and three-photon microscopy using the frequency-doubled fiber laser system. Dual excitation wavelengths at 1580 nm and 790 nm were obtained from the fundamental and frequency-doubled pulses of the laser system, and used to excite TPEF, SHG, and THG. The label-free multimodal MPM imaging can acquire multiple contrasts simultaneously for obtaining comprehensive information about cells and tissues, which has great significance in clinical application. Label-free imaging on *ex vivo* biological samples was carried out, which showed

multiple imaging contrasts obtained from different tissue constituents. Those results demonstrated the capability and potential of the multimodal MPM endoscopy for future clinical applications.

1.8 Outline

The dissertation is organized as follows:

In Chapter 2, a miniature fiber-optic MPM endoscopy system based on a frequency-doubled femtosecond Er-doped fiber laser is demonstrated. The femtosecond pulse from the laser source is delivered to the miniature imaging probe where the pulse is frequency-doubled to excite intrinsic TPEF from tissue. A MEMS scanner, miniature objective, and multimode collection fiber are used to make the probe compact. *Ex vivo* multiphoton imaging of mammalian skin shows the capability of the system in imaging biological tissues.

In Chapter 3, the imaging speed of the MPM endoscopy is further improved by optimizing the excitation laser source. The dependence of the PPLN length on the MPM excitation efficiency is investigated. The Er-doped fiber laser is then manipulated to match its bandwidth with the acceptance bandwidth of the PPLN. Through this optimization, the pulsewidth of the frequency-doubled pulse is reduced. The imaging speed is largely increased and e*x vivo* imaging of unstained biological tissues are conducted.

In Chapter 4, a multimodal MPM endoscopy is demonstrated to acquire two-photon microscopy and three-photon microscopy signals simultaneously, including TPEF, SHG, and THG. The Er-doped fiber laser provides dual wavelengths to excite the nonlinear signals, which includes the fundamental pulse to excite THG and the frequency-doubled pulse to excite intrinsic TPEF and SHG, in biological tissues. Using the multimodal MPM endoscopy, label-free imaging by TPEF, SHG, and THG are demonstrated on unprocessed biological tissues.

Finally, Chapter 5 summarizes our achievements and presents several suggestions for future work.

Chapter 2: Miniature fiber-optic multiphoton endoscopy using frequency-doubled femtosecond Er-doped fiber laser

2.1 Introduction

Multiphoton microscopy (MPM) is an important tool for non-invasive and high-resolution imaging, featuring in neurology [9, 10] and cancer research [11, 12]. It utilizes femtosecond lasers to excite nonlinear contrast signals including two-photon excitation fluorescence (TPEF) and second harmonic generation (SHG) [2, 3]. TPEF can be detected from intrinsic sources and exogenous fluorophores, while strong SHG signals can be detected from non-centrosymmetric molecules such as collagen. As such, MPM is capable of imaging and distinguishing cellular and extracellular matrix structures simultaneously. The small footprint and flexibility of a compact fiber-optic MPM system using a miniaturized probe, have great potential to transform the powerful MPM technology for *in vivo* studies and clinical applications of epithelial tissues and internal organs [69, 70]. However, most of the current MPM systems have a bulky overall size due to the use of a Ti:Sapphire laser which is expensive, not portable, and requires precise alignment.

Currently, femtosecond fiber lasers have emerged as a promising excitation source for compact MPM systems [44, 45, 47], because they are more compact, robust, not susceptible to misalignment, and direct coupling with fiber. By using a commercial Yb-doped fiber laser, Tang *et al*. developed a compact MPM system, where a hollow core photonic bandgap fiber (PBF) was used to deliver 150 fs pulses without any dispersion compensation scheme [44]. The hollow-core PBF can nearly completely eliminate pulse broadening without prechirping at the zero-dispersion wavelength [71]; however, it can significantly broaden the output pulses above or below the exact

zero-dispersion wavelength, and thus dispersion compensation is still needed when using broadband ultrashort lasers or tunable lasers [72]. A home-built Yb-doped fiber laser reported by Liu *et al*. was used in an MPM system with a handheld probe [45]. The output pulse had a pulsewidth of 125 fs and was delivered to a dispersion compensation unit which consisted of a grating pair and then coupled to a double cladding photonic crystal fiber (DCPCF). The DCPCF can deliver the excitation beam in the inner core and collects the signal with a larger cladding and thus its detection efficiency is much higher than the single mode fiber (SMF). However, DCPCF suffers severe pulse broadening and it needs to be compensated by tuning the gratings, which makes the whole system bulky and sensitive to alignment. Furthermore, since the Yb-doped fiber laser works at 1030 nm, fluorescence staining of samples is required to generate TPEF signals.

Murari *et al.* reported a fiber-optic multiphoton endomicroscopy based on a customized Er-doped fiber laser, which included a seed laser, a fiber-based pulse stretcher, an Er-doped fiber amplifier (EDFA), and a fiber-based pulse compressor [47]. The seed pulses were launched into a pulse stretcher which was a customized dispersion-shifted SMF with normal dispersion at 1550 nm, while a standard SMF has anomalous dispersion at 1550 nm. The stretched pulses were amplified by the EDFA and then compressed through a SMF-28 fiber. A customized double cladding fiber was used to deliver the pulses to the endoscope probe. Since the double cladding fiber had similar dispersion and mode field diameter as the fiber compressor, it could be considered as part of the compressor. The benefit of a longer excitation wavelength is deep penetration due to considerably reduced scattering [47]. However, the disadvantages of using 1550 nm excitation wavelength are the need of sample staining and reduced resolution.

Many intrinsic biological molecules have maximal two-photon excitation cross sections at shorter than 800 nm wavelength [24], thus highlighting the importance of laser sources with a

central wavelength in the region of 700~800 nm for *in vivo* multiphoton imaging. Frequency doubling of commercial Er-doped fiber lasers at 780 nm have been utilized in bench-top MPM systems [73, 74]. In the reported work, the frequency-doubled commercial fiber laser had a free-space output and the fiber laser was simply utilized as a free-space source. A commercial frequency-doubled Er-doped fiber laser has been utilized in a fiber-optic MPM endoscope system [75]. The frequency-doubled output was also in free space. The free-space output was then coupled into a hollow core PBF to deliver the pulses to the endoscope. Since the pulses entered the free space and needed to be coupled into fiber again, the fiber laser lost the capability of all-fiber delivery to the distal end of the endoscope.

In this chapter, we propose a miniature fiber-optic MPM probe system based on a frequency-doubled femtosecond Er-doped fiber laser. The laser is directly coupled to the probe through a SMF-28 fiber, which makes the entire system plug-and-play. A frequency-doubling crystal is mounted inside the distal end of the probe and optimized together with the laser to obtain a frequency-doubled beam with relatively high power and short pulsewidth. The frequency-doubled beam at 786 nm is used as the excitation beam to excite intrinsic MPM signals from biological samples, which eliminates the need of staining the samples. Micro-electro-mechanical system (MEMS) scanner, miniature objective, and multimode fiber are further used to make the MPM probe compact. *Ex vivo* images of mammalian skin are obtained to demonstrate the capability of the miniature fiber-optic MPM probe in imaging biological tissues. The preliminary results demonstrate the potential of the miniature fiberoptic MPM system for clinical *in vivo* imaging.

2.2 System design

2.2.1 Er-doped fiber design

The schematic diagram of the MPM system is shown in Fig. 2.1. It includes two major parts – an Er-doped fiber laser and a compact MPM probe, which are shown in the two rectangle boxes in Fig. 2.1, respectively. The fiber laser system comprises an Er-doped fiber oscillator mode-locked via nonlinear polarization rotation [76, 77]. The oscillator has a net dispersion D_T of slightly negative (i.e. D_T at about -0.005 ps^2) [77]. It is driven by a laser diode chip emitting 500 mW at 980 nm. It provides 20 mW of average power at a repetition rate of 67 MHz. The oscillator delivers approximately 80 fs pulses (assuming a sech pulse) centered at ~1580 nm with a spectral full-width-half-maximum (FWHM) bandwidth of 62 nm, resulting in a time-bandwidth-product of 0.6, which indicates nearly transform-limited pulse. The output from the oscillator is then amplified by a bi-directional pumping setup comprised of two 980 nm laser diodes with an overall cw-power of 1 W. The output power after the amplifier is around 250 mW.

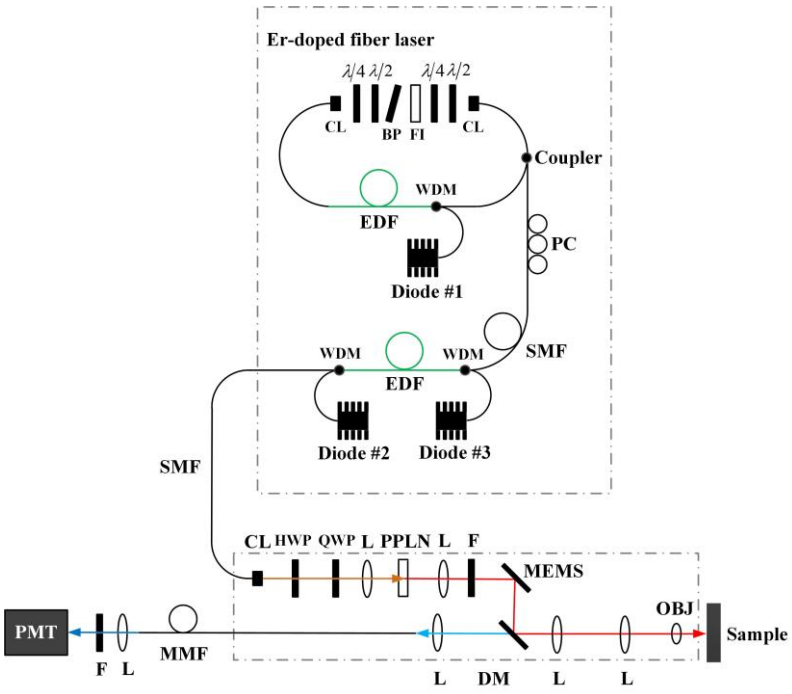

Figure 2.1 Schematic the compact fiber laser based MPM system. EDF: Er-doped fiber; HWP: half-wave plate; QWP: quarter-wave plate; BP: birefringent plate; FI: Faraday isolator; CL: collimating lens; WDM: wavelength division multiplexer; PC: polarization controller; SMF: single mode fiber; L: lens; PPLN: periodically poled MgO:$LiNbO_3$ crystal; F: filter; MEMS: micro-electro-mechanical system mirror; DM: dichroic mirror; OBJ: objective lens; MMF: multimode fiber; PMT: photomultiplier tube.

2.2.2 Frequency doubling

A 110-cm-long SMF-28 fiber delivers the pulses from the Er-doped fiber laser system to the MPM probe, where the fundamental beam is frequency-doubled by a 1-mm-long periodically poled MgO:$LiNbO_3$ (PPLN) crystal (MSHG1550-0.5-1, Covesion Ltd). A half-wave plate and a quarter-wave plate are used to maximize the power of vertically polarized fundamental beam available to be frequency-doubled by the PPLN. Maximum output power can be achieved by linearly translating the crystal to the proper grating period in order to ensure quasi-phase matching (QPM) [78]. An AR-coated focusing lens with a focal length of 7.5 mm (A375TM-C, Thorlabs) is chosen

to focus the vertically polarized fundamental pulse. This lens ensures that the ratio between the crystal length and the confocal parameter of the lens is close to 2, where the conversion efficiency is maximum [79].

The characteristics of the fundamental beam and frequency-doubled beam are shown in Fig. 2.2. The fundamental beam has a spectral FWHM bandwidth of nearly 8 nm in the main peak centered at ~1580 nm as shown in Fig. 2.2(a) and has reasonably small pulsewidth of 250 fs as shown in Fig. 2.2(b), albeit with satellite peaks in the autocorrelation trace. The spectrum and autocorrelation trace of the frequency-doubled pulse are shown in Figs. 2.2(c) and 2.2(d), respectively. The frequency-doubled beam has a pulsewidth of 150 fs, a central wavelength of 786 nm and a spectral FWHM bandwidth of nearly 5 nm in the main peak. With 200 mW of the amplifier output in the vertical polarization that contributes to the frequency doubling, a maximum power of 80 mW is obtained in the frequency-doubled beam, which corresponds to conversion efficiency 40%. Although the fundamental beam and frequency-doubled beam show some pulse structure and pedestals, our preliminary MPM imaging show reasonable signal-to-noise ratio (SNR). Further improvement on SNR can be achieved by eliminating the pulse structure and pedestals by using custom fibers for dispersion compensation, which will be investigated in our future study.

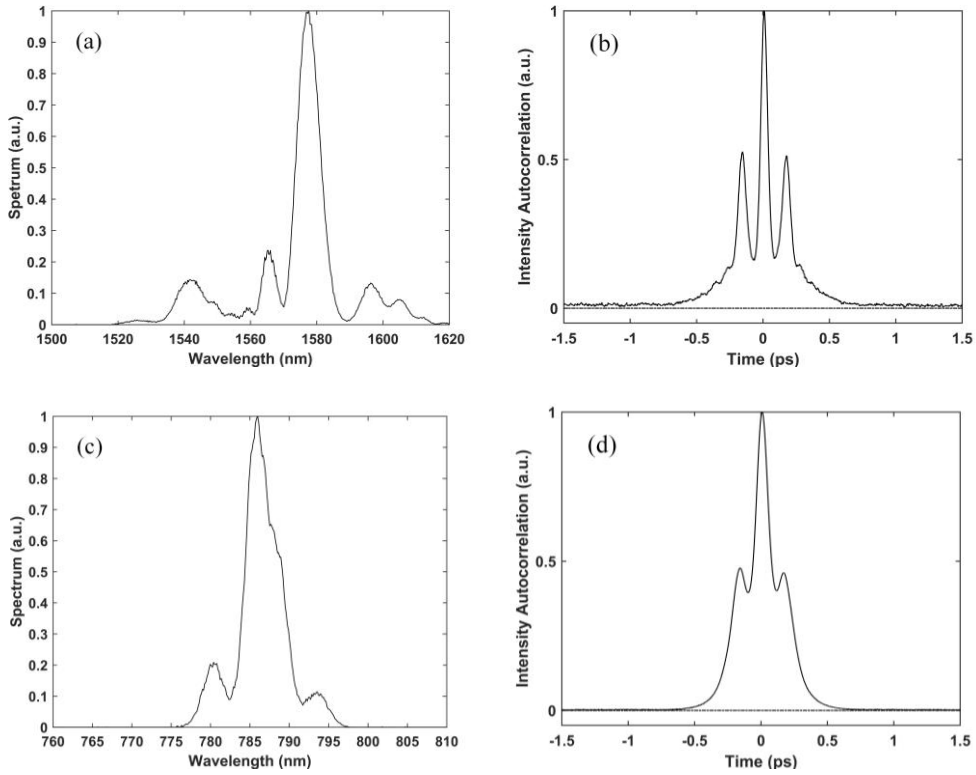

Figure 2.2 Spectra of the (a) fundamental and the (c) frequency-doubled pulse and their corresponding autocorrelation traces in (b) and (d).

An important consideration in frequency doubling is the acceptance bandwidth of the nonlinear crystal. If the fundamental pulse has excessively larger spectral bandwidth than the acceptance bandwidth, the energy outside of the acceptance bandwidth will not convert to the frequency-doubled pulse. Theoretically the maximum bandwidth of the frequency-doubled beam is approximately half of the acceptance bandwidth of the PPLN [80]. The acceptance bandwidth of the 1-mm-long PPLN is 13 nm when the fundamental wavelength is 1580 nm and it increases when the crystal length reduces. Therefore, a broader bandwidth (thus relatively a shorter pulsewidth) of the frequency-doubled beam can be achieved by the use of a shorter PPLN crystal and a fundamental beam with a bandwidth close to the corresponding acceptance bandwidth. For example, a 0.3-mm-long PPLN has an acceptance bandwidth of about 44 nm when the

fundamental wavelength is 1580 nm. If the bandwidth of the fundamental beam can be increased to 44 nm, we can obtain shorter frequency-doubled pulses by using the 0.3-mm-long PPLN compared to the 1-mm-long crystal. Shorter pulses can potentially increase the efficiency of MPM which is inversely proportional to the pulsewidth of the excitation beam. Meanwhile, the conversion efficiency may reduce when the crystal length is shortened. Thus optimization of the MPM system will consider the fiber laser bandwidth, the PPLN thickness, the pulsewidth and power at the sample location etc., which will be a topic for future study.

In our system, the femtosecond pulses are delivered to the distal end of the probe at the 1580 nm wavelength by the standard SMF and the frequency-doubling to 786 nm is performed inside the probe. Delivering femtosecond pulses at 1580 nm has several advantages. First, the absolute value of group velocity dispersion (GVD) is lower at 1580 nm than at 786 nm in SMF. Second, standard SMF has anomalous dispersion at 1580 nm which can be used for fiber-based dispersion compensation. Thus the pulsewidth can be minimized by adjusting the length of the output SMF to compensate for the normal dispersion from the Er-doped fiber. Furthermore, at 1580 nm wavelength band, there are various types of dispersion compensation fibers [81] available that can precisely manage both the GVD and its slope for optimum dispersion compensation. Therefore, with our approach, we can achieve all-fiber-based dispersion compensation and also be able to operate the system at 786 nm to excite intrinsic MPM signals without the need for staining.

2.2.3 Miniature fiber-optic MPM probe design

The schematic of the MPM probe is indicated in the bottom rectangle box in Fig. 2.1, and a photograph of the assembled probe is shown in Fig. 2.3. After the PPLN, an aspheric lens (C220TMD-B, Thorlabs) is used to collimate the frequency-doubled beam and a glass filter (Schott

RG9) is used to block the residual fundamental beam. The beam is then directed to a MEMS 2D scanner (Mirrocle Tech., Inc.) to perform raster scanning. Two identical Ø1/2" achromatic doublets (AC127-019-A, f = 19.0 mm, Thorlabs) are used to relay the beam to a miniature objective lens, where the beam fills its entire back aperture. An aspheric lens C150TME-A (f = 2.0 mm, NA = 0.50, Thorlabs) is used as the objective lens. The emitted multiphoton signals are separated from the back-reflected excitation light by a short-pass dichroic mirror (FF670-SDi01, Semrock). The MPM signals are coupled by an achromatic doublet (AC050-008-A, f = 7.5 mm, Thorlabs) into a multimode fiber (MMF) patch cable (Ø1500 μm, NA = 0.39, Thorlabs) and sent to a photomultiplier tube (PMT) (H9305-03, Hamamatsu), followed by a photon counting unit (C9744, Hamamatsu). A blocking filter with a passband from 350 to 650 nm (FF01-680/SP-25, Semrock) is placed in front of the PMT in order to remove the residual of the back-reflected excitation light. The field of view (FOV) of the system is 151 μm × 236 μm (328 pixels × 512 pixels) and the maximum power from the probe is 50 mW. The frame rate is 0.4 frames/s when the pixel dwell time is 10 μs. While the slow Y-axis of the MEMS scanner is driven by a sawtooth waveform, the fast X-axis is driven by a sinusoidal waveform to maximize its speed. Image distortion due to the sinusoidal scanning is corrected by data processing, resulting in different final image size in X and Y axis. The housing of the compact probe [82] is made by 3D printing technology and the overall size of the packaged probe is 40 mm (height) × 45 mm (width) × 165 mm (length). The prototype of the MPM handheld probe has a relatively large size. To further reduce the size of the MPM probe, a customized MEMS with a smaller circuit board is required. The housing of the probe can be reduced by using metal. Based on those approaches, the cross-sectional dimension of the MPM probe could be reduced to ~20 mm. Furthermore, the scan lens,

tube lens, and objective lens section could be reduced to a cross-sectional dimension of ~10 mm. This type of MPM probe can potentially be applied to image skin, oral cavity, and cervix.

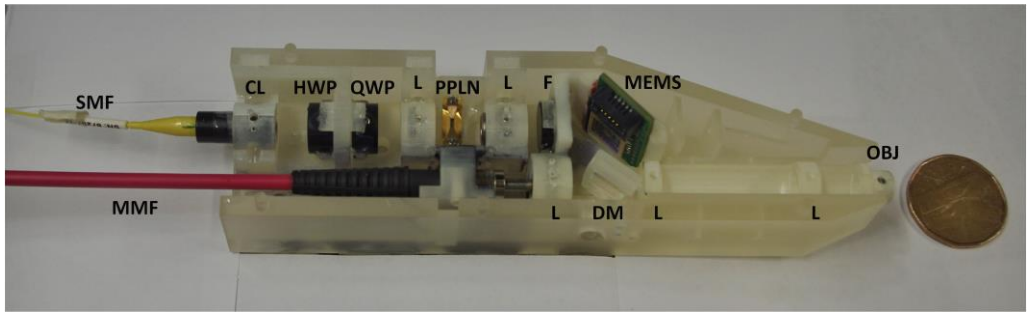

Figure 2.3 A photograph of the miniature fiber-optic MPM probe. SMF: single mode fiber; CL: collimating lens; HWP: half-wave plate; QWP: quarter-wave plate; L: lens; PPLN: periodically poled MgO:$LiNbO_3$ crystal; F: filter; MEMS: micro-electro-mechanical system mirror; DM: dichroic mirror; OBJ: objective; MMF: multimode fiber. The Loonie shown has a diameter of 26.5 mm.

2.3 Results and discussion

While the PPLN is used for frequency doubling, it also produces third harmonic generation (THG) output. The THG output of PPLN is centered at 530 nm as shown in Fig. 2.4. Thus the THG output of the PPLN can overlap with the TPEF signal from the sample. Generally, the TPEF signal of nicotinamide adenine dinucleotide hydrogen (NADH), which is a typical native biological fluorophore, peaks around 450 nm and extends to 600 nm [83]. Thus the THG output of the PPLN can potentially reduce the SNR in the MPM system. A glass bandpass filter (RG9, Schott) which has the transmission window of 700-1050 nm can block the THG output in the main beam path. However, in our study, we have observed that scattered THG output could still reach the collection fiber from the side. To reduce the effect of the THG output, the side walls of the MPM probe need to be fully blocked. Using highly opaque materials in 3D printing can block it from entering into the collection fiber.

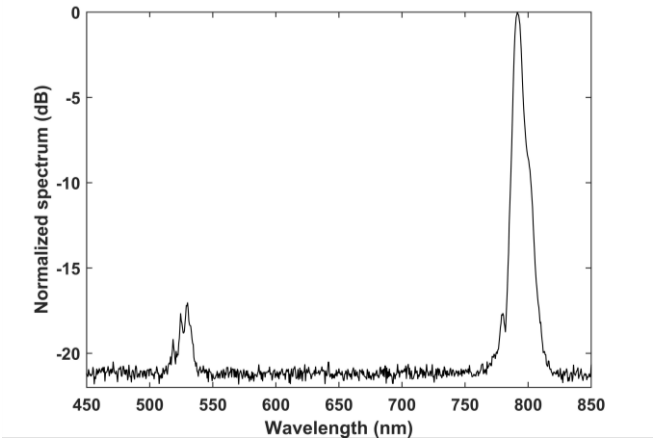

Figure 2.4 The normalized spectrum of the second order generation signal and third order generation signal of PPLN.

The lateral resolution of the miniature fiber-optic MPM system is quantified by investigating the two-photon point spread function (PSF) of the 0.1-μm-diameter fluorescent beads (Fluoresbrite® Calibration Grade Size Range Kit, Polysciences, Inc.). The intensity measured across a single bead and its Gaussian fitting curve are shown in Fig. 2.5. The FWHM of the two-photon PSF is about 1.3 μm, which corresponds to the lateral resolution of the MPM system.

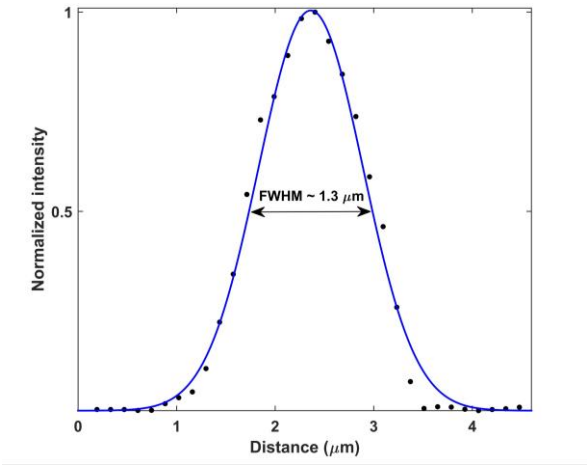

Figure 2.5 The lateral two-photon PSF plot for a 0.1-μm-diameter fluorescent bead. Experimental data (black dots) and results of the Gaussian fit (in blue) are shown.

The miniature fiber-optic MPM system is applied to image several biological tissue samples. The tissues are kept in saline and imaged within two hours postmortem. The power on sample is ~50 mW. The penetration depth in biological tissue is estimated to be around 50-100 μm. The SHG image of a skin sample from a Yucatan swine is shown in Fig. 2.6(a), and the SHG image of a skin sample from a Zealand white rabbit is shown in Fig. 2.6(b). These SHG images show clear collagen structures in the dermal layer. The collagen fiber structures seem to be finer in the leporine skin than that in the porcine skin. The TPEF image of a skin sample from a CD-1 mouse is shown in Fig. 2.6(c), in which the cells in the epidermal layer are observed. The intrinsic TPEF signals are observed to be much weaker than the SHG signals in our samples and Fig. 2.6(c) is averaged over 10 frames. For all the images, the pixel dwell time is 10 μs and the FOV is 151 μm × 236 μm. All these *ex vivo* images are staining-free, showing that the miniature fiber-optic MPM probe system has the capability of imaging intrinsic signals from biological tissues. The current imaging speed is limited by the relatively low SNR. Increasing the system SNR is possible by optimizing the fiber laser and the frequency doubling process to achieve shorter pulses, and designing a compound miniature objective to focus the laser beam into a smaller focal volume on the sample. Such investigations will be carried out in Chapter 3.

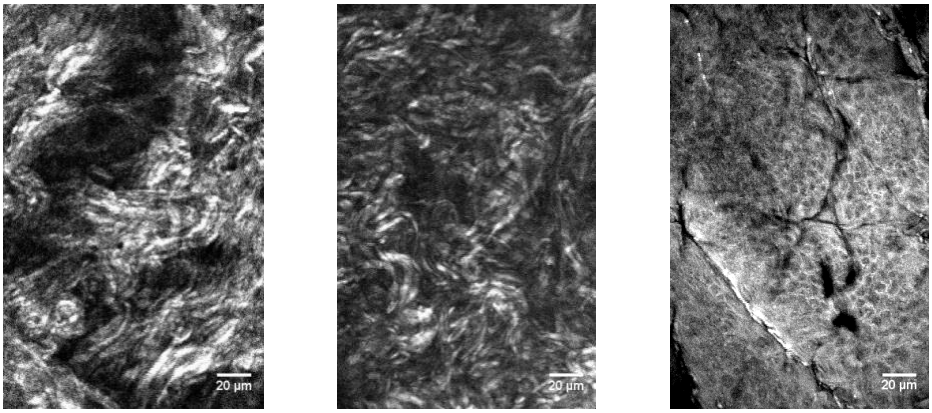

(a) (b) (c)

Figure 2.6 Images acquired by the miniature fiber-optic MPM probe system. (a) SHG image of a porcine skin. (b) SHG image of a leporine skin. (c) TPEF image of a murine skin averaged over 10 frames. Scale bar is 20 μm.

2.4 Conclusions

In summary, we have developed a miniature fiber-optic MPM system based on frequency-doubled femtosecond Er-doped fiber laser. The laser is directly coupled to the MPM probe through a SMF-28 fiber and the emitted signals are collected through a MMF patch cable, making the whole setup fiber connected. The miniature fiber-optic MPM system is compact, portable, and robust. *Ex vivo* SHG/TPEF images of unstained skin samples are acquired to verify the imaging capability of the miniature fiber-optic MPM system. With the compact femtosecond fiber laser and the MPM probe, *in vivo* imaging will become possible and different locations in the samples can become easier to be accessed.

Chapter 3: Optimization of frequency-doubled Er-doped fiber laser for miniature multiphoton endoscopy

3.1 Introduction

Multiphoton microscopy (MPM) is a laser-scanning microscopy technique based on exciting and detecting nonlinear optical signals from tissues [21, 22]. It is considered as one of the best noninvasive means of biological imaging microscopy in tissues and live animals [2] In MPM, near-infrared (NIR) femtosecond lasers are used to excite nonlinear contrast signals such as two-photon excitation fluorescence (TPEF) and second harmonic generation (SHG) [2, 3]. In order to utilize MPM in clinical applications, miniature MPM endoscopy needs to be developed. In MPM endoscopy, the excitation laser light and the MPM signals can be guided through flexible optical fiber, and thus various tissue locations can be conveniently imaged via a miniature probe [39-41]. To date, many different groups proposed MPM endoscopy systems and applied them for different applications [32-38].

Currently, the most commonly-used femtosecond laser in MPM endoscopy is the solid-state mode-locked Ti:Sapphire laser [32-41]. An early miniature MPM endoscopy system was reported by Helmchen *et al*. for imaging the brain of freely moving mice [39]. A Ti:Sapphire laser was coupled into a single mode fiber (SMF) after double passing a pair of diffraction gratings for group velocity dispersion (GVD) pre-compensation. The system had a relatively bulky prototype and the imaging speed was only 0.5 frames/s. Huland *et al*. developed an MPM endoscopy system where the pulse from a Ti:Sapphire laser was delivered by a hollow core photonic bandgap fiber (PBF) [41]. *In vivo* imaging was conducted on unstained tissue in anesthetized rats at 4 frames/s.

However, Ti:Sapphire lasers are costly and bulky, output into free-space, and require precise alignment, which limits their clinical applications in the MPM endoscopy systems.

Compared to Ti:Sapphire lasers, femtosecond fiber lasers are compact, robust, insusceptible to misalignment, and offer direct coupling into optical fiber. Two types of fiber lasers -- Yb-doped fiber laser operating at the 1030 nm region, and Er-doped fiber laser operating at the 1550 nm region, have emerged as promising excitation sources for MPM endoscopy [45-47]. Two compact MPM endoscopy systems were reported using Yb-doped fiber lasers, in which a grating pair was used before the MPM handheld probe for pre-compensating the dispersion to achieve a pulsewidth of 125 fs [45] and sub-500 fs [46], respectively. Murari *et al*. reported a fiber-optic MPM endoscopy with a customized Er-doped fiber laser, where a 700-m-long SMF was used to compress the laser pulse from ~290 ps to ~300 fs [47]. Due to the relatively long excitation wavelengths of the fiber lasers, they cannot efficiently excite intrinsic TPEF signal from native tissue constituents, such as nicotinamide adenine dinucleotide hydrogen (NADH) and flavin adenine dinucleotide (FAD). Fluorescence staining is usually required to generate TPEF contrast [24]. Instead of TPEF, Horton *et al*. used an Er-doped fiber laser at 1700 nm for exciting intrinsic three-photon fluorescence imaging *in vivo* [84]. However, the excitation efficiency of three-photon excitation fluorescence is much lower than TPEF.

The frequency-doubled Er-doped fiber laser centers around 780 nm, which can be utilized as the excitation source for staining-free MPM imaging [73-75]. Unruh *et al*. [73] and Chun *et al*. [74] used commercial Er-doped fiber lasers with a frequency-doubled output as the excitation source in benchtop MPM systems, where the fiber lasers were used as a free-space laser source. Recently, a miniature MPM endoscopy system was reported by Huland *et al*., which utilized a commercial Er-doped fiber laser with a frequency-doubled output [75]. The fiber laser was output

into free-space and then re-coupled into a photonic crystal fiber to deliver 780 nm pulse to an MPM endoscope. This process required precise alignment for fiber re-coupling, introduced coupling loss, and lost the convenience of direct fiber connection.

A miniature fiber-optic MPM endoscopy system based on frequency-doubled Er-doped fiber laser was demonstrated in our previous work [85]. The laser pulse was directly coupled via an SMF to the imaging probe where the pulse was frequency-doubled in the distal end of the probe. Femtosecond pulses at 780 nm wavelength were obtained and used to excite intrinsic TPEF signal from tissues. *Ex vivo* MPM imaging of unstained biological tissues was demonstrated at 0.4 frames/s. However, the imaging speed was relatively low and the frequency-doubled pulse had side lobes which reduced the temporal quality of the excitation source. The imaging speed was mainly limited by the low MPM excitation efficiency. To increase the imaging speed, the MPM signal level needs to be increased by improving the MPM excitation efficiency.

In this chapter, a systematic optimization of the frequency-doubled Er-doped fiber laser to increase the MPM excitation efficiency is carried out. The effect of the frequency-doubling process on the MPM excitation and the factors that affect the characteristics of the frequency-doubled pulse are analyzed. Optimization on the laser source and its frequency-doubling process is also carried out experimentally. Using the optimized frequency-doubled pulse as the excitation source, MPM imaging with significantly increased speed is demonstrated by *ex vivo* imaging of unstained biological tissues. It is shown that the miniature MPM endoscopy with the frequency-doubled Er-doped fiber laser has great potential in translating MPM imaging into clinical applications.

3.2 System optimization

3.2.1 System configuration

Figure 3.1 shows the schematic diagram of the miniature MPM endoscopy system with the frequency-doubled Er-doped fiber laser. The system contains four major parts, 1) Er-doped fiber oscillator, 2) bi-directionally pumped Er-doped fiber amplifier, 3) frequency-doubling unit, and 4) MPM endoscopy imaging head. Details about the four parts are described below, respectively.

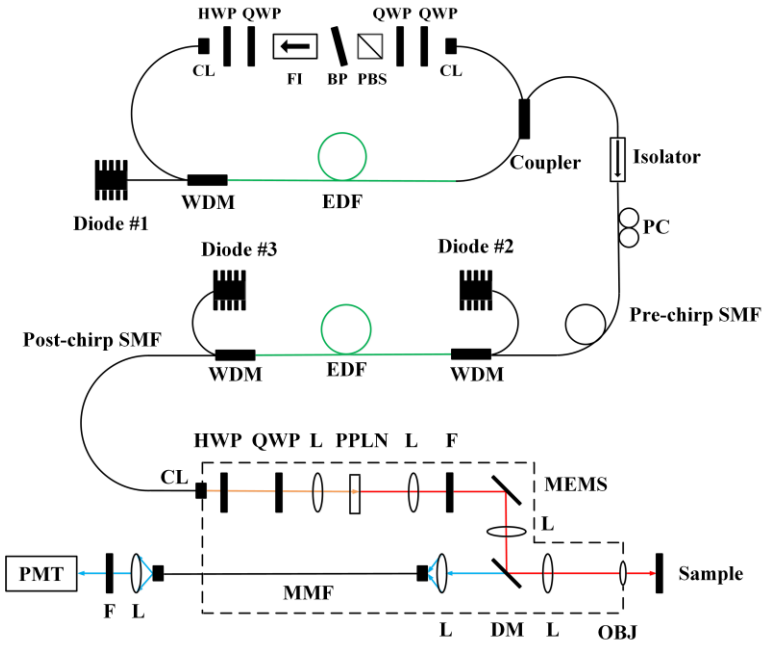

Figure 3.1 Schematic of the miniature MPM endoscopy system with the frequency-doubled Er-doped fiber laser. The dashed box indicates the MPM endoscopy imaging head. EDF: Er-doped fiber; HWP: half-wave plate; QWP: quarter-wave plate; BP: birefringent plate; FI: Faraday isolator; PBS: polarization beam splitter; CL: collimating lens; WDM: wavelength division multiplexer; PC: polarization controller; SMF: single mode fiber; M: mirror; L: lens; PPLN: periodically poled MgO:$LiNbO_3$ crystal; F: filter; MEMS: micro-electro-mechanical system mirror; DM: dichroic mirror; OBJ: objective lens; MMF: multimode fiber; PMT: photomultiplier tube.

1) Er-doped fiber oscillator

An Er-doped fiber oscillator, mode-locked via nonlinear polarization rotation [76, 77], is used as the seed laser. The oscillator is pumped by a diode laser at 980 nm. The optical fiber section of the oscillator cavity contains 0.96-m-long Er-doped fiber (EDF) (EDF80, OFS) with GVD of +0.061 ps^2/m at 1560 nm. The total length of SMF (SMF-28, Corning) in the oscillator is 2.4 m, with GVD of -0.023 ps^2/m at 1560 nm. The net dispersion of the oscillator is designed to be slightly positive by adjusting the lengths of the SMF and EDF, respectively. The net dispersion based on the fiber lengths is approximately +0.003 ps^2 at 1560 nm.

2) Bi-directionally pumped Er-doped fiber amplifier

The fiber amplifier contains a piece of EDF which is bi-directionally pumped by two 980 nm laser diodes with an overall CW-power of 1.2 W. The seed pulse from the oscillator first propagates through a section of pre-chirp fiber, mostly composed by SMF. After the pre-chirp fiber, the pulse enters a 1.65-m-long EDF. Finally, the amplified pulse is delivered via a pigtailed collimator with a piece of post-chirp SMF. The post-chirp SMF has anomalous dispersion at 1560 nm and thus it compensates the dispersion and compresses the pulse after the EDF. The amplified output power is around 260 mW.

3) Frequency-doubling unit

Frequency-doubling is achieved through a periodically poled MgO:$LiNbO_3$ (PPLN) crystal (MSHG1550-0.5-0.3, Covesion Ltd.). A half-wave plate and a quarter-wave plate are used to adjust the polarization for efficient frequency-doubling in the PPLN. The fundamental beam is focused into the PPLN by an aspheric lens with a focal length of 7.5 mm (A375TM-C, f = 7.5 mm, NA = 0.3, Thorlabs). Another aspheric lens (A397TM-B, f = 11.0 mm, NA = 0.3, Thorlabs) is

used to collimate the frequency-doubled beam and a filter (RG9, Schott) is used to block the residual fundamental power.

4) MPM endoscopy imaging head

The dashed box in Fig. 3.1 indicates the MPM endoscopy imaging head, which includes the frequency-doubling unit. Therefore, there is no need to re-couple the light into fiber again after the frequency-doubling. After the frequency-doubling unit, the beam is directed to a 2.4-mm-diameter 2D micro-electro-mechanical system (MEMS) mirror (Mirrocle Tech., Inc.) to raster scan the beam. Two identical Ø1/2" achromatic doublets (AC127-019-A, f = 19.0 mm, Thorlabs) are used to relay the beam from the MEMS scanner to a miniature objective lens. An aspheric lens C150TME-A (f = 2.0 mm, NA = 0.50, Thorlabs) is used as the objective lens. The emitted MPM signals are collected in the backward direction and separated from the excitation light by a dichroic mirror (FF670-SDi01, Semrock). The MPM signals are coupled by an achromatic doublet (AC050-008-A, f = 7.5 mm, Thorlabs) into a multimode fiber (MMF) patch cable (Ø1500 μm, NA = 0.39, Thorlabs), and sent to a photomultiplier tube (PMT) (H9305-03, Hamamatsu). A blocking filter with a passband from 350-650 nm (FF01-680/SP-25, Semrock) is placed in front of the PMT to remove the residual of the back-reflected excitation light. Since the Er-doped fiber laser is directly coupled into the imaging head through a standard SMF and the emitted MPM signal is directed to the PMT by a MMF, the MPM endoscopy system is compact and fiber connected. The field-of-view (FOV) of the MPM system is 160 μm × 250 μm (328 pixels × 512 pixels). The lateral resolution is 1.2 μm and the axial resolution is 16 μm.

3.2.2 MPM intensity

To optimize the system, the influence of the excitation laser properties on the MPM intensity is analyzed. The time-averaged TPEF intensity excited by a femtosecond pulse can be described by [20]

$$\langle I_{TPEF} \rangle \cong \delta_2 \eta \frac{P_{ave}^2}{\tau_p f_p} \left(\frac{\mathrm{NA}^2}{hc\lambda} \right)^2 \tag{3.1}$$

where, τ_p is the pulse duration, P_{ave} is the average laser power, f_p is the repetition rate of the laser, δ_2 is the two-photon absorption cross-section, η is the fluorescence quantum yield, NA is the numerical aperture of the objective lens, λ is the excitation wavelength, h and c are Planck's constant and the speed of light in vacuum, respectively. As we can see, the TPEF intensity depends quadratically on the average laser power, and inversely on the pulse duration and repetition rate of the excitation light. The SHG intensity has a similar dependence. Increasing the average laser power can increase the MPM intensity. Nevertheless, the laser power needs to be kept below the safety limit in order not to cause tissue damage and loss of cell viability [42]. MPM intensity can also be increased by shortening the pulse duration. In this study, we will improve the MPM intensity by optimizing the Er-doped fiber laser system.

3.2.3 Frequency-doubling by PPLN

To increase the MPM intensity, the frequency-doubled pulse needs to be optimized for shorter pulsewidth and higher average power within the laser safety limit. The design considerations on frequency-doubling by PPLN will be discussed. The frequency-doubling process depends on the input pulsewidth, bandwidth, and phase matching. The related theory is explained below.

In the classical theory of second harmonic generation in a nonlinear crystal, assuming plane-wave and nondepleted pump, the electric field of the frequency-doubled output is described by [49]

$$\tilde{E}_{2\omega}(L) = \frac{-j\omega_0 d_{eff}}{n_2 c}\tilde{E}_{\omega}^2(0)L\exp(j\Delta kL/2)\mathrm{sinc}(\Delta kL/2) \tag{3.2}$$

where $\tilde{E}_{\omega}$ is the electric field of the fundamental beam, L is the crystal length, d_{eff} is the nonlinear coefficient, n_2 is the refractive index associated with the frequency-doubled frequency $2\omega_0$. The difference in the propagation constants of the fundamental and frequency double beams, $\Delta k = k_2 - 2k_1$, is the phase mismatch. The conversion from the fundamental beam to the frequency-doubled beam is most efficient when the phase mismatch is zero.

When there is phase mismatch as $\Delta k \neq 0$, the power is only efficiently converted from the fundamental beam to the frequency-doubled beam within the coherent buildup length $l_c = \pi/\Delta k$. On the other hand, PPLN relies on quasi-phase-matching (QPM) to increase the interaction length and conversion efficiency. In QPM, the sign of d_{eff} alternates periodically with a period Λ. Thus a structural periodicity is built into the nonlinear crystal, to repeatedly correct the relative phase between the ω_0 and $2\omega_0$ fields. This periodic modulation on the nonlinear coefficient acts as a grating which introduces a momentum and modifies the phase matching parameter in 1st-order QPM as [49]

$$\Delta k' = \Delta k + \frac{2\pi}{\Lambda} \tag{3.3}$$

With the modified phase matching parameter, the electric field of the frequency-doubled output in QPM is given by [49]

$$\tilde{E}_{2\omega}(L) = \frac{-j\omega_0 d_{eff}}{n_2 c}\tilde{E}_{\omega}^2(0)LG\exp(j\Delta k' L/2)\mathrm{sinc}(\Delta k' L/2) \tag{3.4}$$

Comparing Eqs. (3.2) and (3.4), Δk is replaced by $\Delta k'$ in QPM, where the momentum from the grating assists the phase matching condition. Although QPM can increase the interaction length between the fundamental and frequency-doubled beams, the conversion efficiency is lower than that in a single crystal with perfect phase matching. This efficiency reduction is described by the factor $G = 2/\pi$ [49].

From the electric field, intensity can be calculated by $I_{(i)} = \frac{1}{2}\varepsilon_0 c n_{(i)}\left|\tilde{E}_{(i)}\right|^2$, where ε_0 is the permittivity of free space [49]. The subscript *i* stands for either ω or 2ω. For frequency-doubling of femtosecond pulse in a thin PPLN, the time dependence of intensity is introduced and quasi-continuous-wave limit is applied. Assuming phase matching as $\Delta k' = 0$, a time-averaged intensity for pulsed excitation can be obtained as

$$\left\langle I_{2\omega}(t)\right\rangle = G^2\Gamma^2 g\left\langle I_{\omega}(t)\right\rangle^2 L^2 \tag{3.5}$$

where $\Gamma^2 = \frac{2\omega_0^2 d_{eff}^2}{\varepsilon_0 c^3 n_1^2 n_2}$ (n_1 is the refractive index associated with the fundamental frequency ω_0), and $g = \left\langle I_{\omega}^2(\mathrm{t})\right\rangle \Big/ \left\langle I_{\omega}(t)\right\rangle^2$ is a measure of the second-order temporal coherence of the excitation source. For a repetitively pulsed laser, g can be expressed as $g = g_p/\tau_p f_p$, where g_p is a dimensionless quantity. For a Gaussian pulse, $g_p = 0.664$ [86].

To increase the conversion efficiency, the laser beam is focused into the PPLN. The averaged power of the fundamental and frequency-doubled beams can be calculated by integrating the averaged intensity over the beam cross section [49]:

$$P_{(i)} = \left\langle I_{(i)}(t)\right\rangle \int dA\left|u_{(i)}\right|^2 \tag{3.6}$$

where $u_{(i)}$ is the corresponding Gaussian beam function. By combining Eqs. (3.5) and (3.6), the averaged power of the frequency-doubled beam is obtained as [49]:

$$P_{2\omega} = \frac{g_p}{\tau_p f_p} G^2 \Gamma^2 \left\langle I_\omega(t) \right\rangle^2 L^2 \int dA \left| u_{2\omega} \right|^2 = \frac{g_p G^2 \Gamma^2 P_\omega^2 L^2}{\tau_p f_p A_{eff}} \tag{3.7}$$

where $A_{eff} = \frac{\left(\int dA \left| u_\omega \right|^2 \right)^2}{\int dA \left| u_{2\omega} \right|^2}$. For the fundamental and frequency-doubled beams, $\left| u_{2\omega} \right| = \left| u_\omega \right|^2$ can be applied. For a Gaussian beam, $A_{eff} = \pi w_{0(\omega)}^2$, where $w_{0(\omega)}$ is the beam waist of the fundamental beam. Optimum focusing is obtained when the depth of focus $b \cong L$ [49], where $b = 2n_1 \pi w_{0(\omega)}^2 / \lambda$. Thus, the output power of the frequency-doubled beam can be obtained as

$$P_{2\omega} = \frac{2n_1 g_p L G^2 \Gamma^2 P_\omega^2}{\lambda \tau_p f_p} \tag{3.8}$$

As we can see in Eq. (3.8), the output power of the frequency-doubled beam in PPLN depends linearly on the PPLN length and inversely on the input pulsewidth under the perfect phase matching condition.

Nevertheless, the perfect phase matching condition $\Delta k' = 0$ in QPM is only achieved at a specific wavelength. For a femtosecond pulse with a broad bandwidth, an acceptance bandwidth is defined for a particular length of PPLN, where phase matching is approximately achieved within the acceptance bandwidth. The acceptance bandwidth is determined by the dispersion property of the crystal. For a Gaussian pulse, it is given by [87]

$$\delta\lambda = \frac{0.4429\lambda}{L} \left| \frac{n_2 - n_1}{\lambda} + \frac{\partial n_1}{\partial \lambda} - \frac{1}{2} \frac{\partial n_2}{\partial \lambda} \right|^{-1} \tag{3.9}$$

It shows that the acceptance bandwidth is inversely dependent on the crystal length *L*. For shorter PPLN length, its acceptance bandwidth $\delta\lambda$ is broader. In order to efficiently convert the input pulse

into frequency-doubled pulse, the bandwidth of the input fundamental beam $\Delta\lambda$ should match with the acceptance bandwidth of the PPLN so that $\Delta\lambda = \delta\lambda$. For transform-limited pulse, the product of the bandwidth and pulsewidth is a constant. For a Gaussian pulse, the transform-limited pulsewidth $\tau_p = 0.4429\lambda^2/c\delta\lambda$ can be calculated from Eq. (3.9) as

$$\tau_p = \frac{\lambda L}{c}\left|\frac{n_2 - n_1}{\lambda} + \frac{\partial n_1}{\partial \lambda} - \frac{1}{2}\frac{\partial n_2}{\partial \lambda}\right| \tag{3.10}$$

Therefore, the pulsewidth is linearly proportional to the PPLN length as limited by its acceptance bandwidth. Substituting Eq. (3.10) into Eq. (3.8), we get

$$P_{2\omega} \cong \frac{2n_1 c g_p G^2 \Gamma^2 P_\omega^2}{f_p \lambda^2}\left|\frac{n_2 - n_1}{\lambda} + \frac{\partial n_1}{\partial \lambda} - \frac{1}{2}\frac{\partial n_2}{\partial \lambda}\right|^{-1} \tag{3.11}$$

When the full-width-half-maximum (FWHM) bandwidth of the fundamental beam matches the acceptance bandwidth of the PPLN, the power of the frequency-doubled output is irrelevant to the PPLN length. In the quasi-continuous-wave limit, the pulsewidth of the frequency-doubled pulse equals $\tau_p/\sqrt{2}$ for a Gaussian beam, where τ_p is the fundamental pulsewidth [49].

Figure 3.2 shows the theoretically transform-limited pulsewidth as a function of the PPLN length. The solid line and dashed line represent how the transform-limited pulsewidth of the fundamental beam at 1560 nm and the frequency-doubled beam at 780 nm, respectively, change with the PPLN length, which both show a linear relationship.

From Eq. (3.1), the MPM intensity depends quadratically on the average power and inversely on the pulsewidth of the excitation laser beam. Here the frequency-doubled beam is used as the excitation source for the MPM imaging. When the spectral bandwidth of the fundamental beam matches with the acceptance bandwidth of the PPLN, the average power of the frequency-doubled beam does not depend on the PPLN length but the pulsewidth of the frequency-doubled

beam depends linearly on the PPLN length. Therefore, the relationship between the time-averaged MPM intensity and the PPLN length L is simply $\langle I_{MPM} \rangle \propto \frac{1}{L}$. The MPM intensity versus the PPLN length is also plotted in Fig. 3.2 as the dash-dotted line.

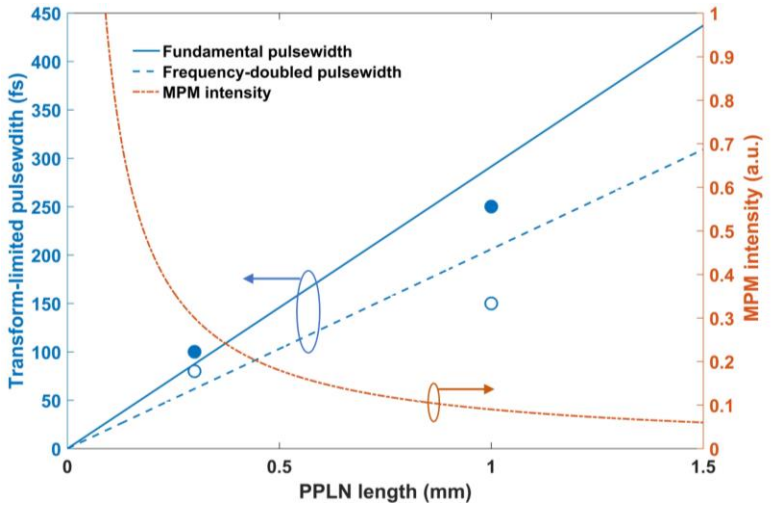

Figure 3.2 Dependence of the pulsewidth and MPM intensity on the PPLN length. The experimentally measured pulsewidths at PPLN length 0.3 mm and 1.0 mm are marked by the solid circles for the fundamental beam and open circles for the frequency-doubled beam. The ellipses with arrows indicate the corresponding Y-axis of the curves.

In principle, the MPM intensity can be increased by choosing a shorter PPLN length, which can provide a shorter frequency-doubled pulsewidth without affecting its output power. However, there are practical challenges when the PPLN length is very short due to the high nonlinear effects at very short pulsewidth. For example, a 0.1-mm-long PPLN has an acceptance bandwidth of 123 nm at 1560 nm and a corresponding transform-limited pulsewidth of 29 fs. At 29 fs pulsewidth, the peak power will be extremely high and the fiber nonlinearity will be significant. It will also be challenging to compensate the dispersion and find components that can cover this broad bandwidth. Considering the trade-off between the advantages of short-pulse and the practical challenges, a PPLN length of 0.3 mm is selected as the optimum design under the current

experimental condition. It has an acceptance bandwidth of 42 nm at 1560 nm and a transform-limited fundamental pulsewidth of 87 fs. In our previous study [85], a 1-mm-long PPLN was used, which had an acceptance bandwidth of 12 nm at 1560 nm and a transform-limited fundamental pulsewidth of 291 fs. Compared to the 1-mm-long PPLN, the 0.3-mm-long PPLN can potentially reduce the pulsewidth to 1/3 of the pulsewidth of the 1-mm-long PPLN.

3.2.4 Er-doped fiber laser optimization

The design consideration on the fiber laser oscillator and the amplifier is to achieve a clean spectrum that matches the acceptance bandwidth of the PPLN and obtain a nearly transform-limited pulsewidth. For the selected 0.3-mm-long PPLN, the targeted FWHM bandwidth of the Er-doped fiber laser should be 42 nm. Figure 3.3 shows the spectrum and the intensity autocorrelation of the oscillator measured at the reflection port of the polarization beam splitter (PBS). The central wavelength is ~1560 nm, the FWHM spectral bandwidth is 47 nm, and the -10 dB spectral bandwidth is 77 nm. The FWHM spectral bandwidth of the oscillator is close to the acceptance bandwidth of the 0.3-mm-long PPLN. The pulsewidth is 247 fs assuming a Gaussian pulse. Here the pulse is not compressed and is slightly chirped. The average power of the oscillator through the output port of the coupler is 4 mW and the repetition rate is 47 MHz.

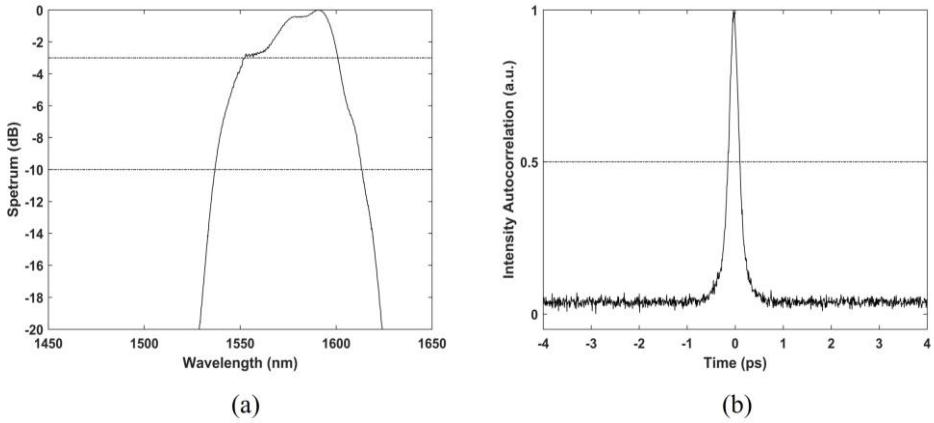

Figure 3.3 The spectrum (a) and the intensity autocorrelation (b) of the oscillator output.

The seed pulse from the oscillator is then sent to the fiber amplifier which boosts the output power to 260 mW. At this power level, the interplay between GVD and self-phase modulation (SPM) is significant, which determines the characteristics of the amplified pulse. Figure 3.4 compares the results obtained at several pre-chirp fiber lengths. The spectrum and intensity autocorrelation of the amplified fundamental pulse, and the spectrum of the frequency-doubled pulse after PPLN are shown. The fundamental pulsewidth is measured at the output of the post-chirp SMF before pulse compression is applied. Gaussian pulse shape is assumed for all the pulsewidth calculation in this paper. Since the output spectrum is not smooth and contains multiple peaks for some cases, -10 dB spectral bandwidth is used for comparison.

Figure 3.4(a) shows the case when the pre-chirp SMF is 12.8 m, corresponding to a pre-chirp dispersion of -0.30 ps^2. The post-chirp SMF fiber is 0.9 m. It shows a narrowed spectrum with the -10 dB spectral bandwidth of 11 nm, and a broad pulsewidth of 1.9 ps. Since the spectral bandwidth is too narrow, no frequency-doubling is performed. From Eq. (3.3), the theoretical grating period Λ for achieving QPM at 1560 nm wavelength at room temperature (30 ˚C) is calculated to be 19.70 μm, which matches with the optimal period found in the experiment. The

PPLN has multiple periods which can be selected by translating the PPLN horizontally. Under different pre-chirp fiber lengths, the actual central wavelength shifts slightly. The optimal grating period is found by maximizing the frequency-doubled power when translating the PPLN to the proper period.

Figure 3.4(b) shows the case when the pre-chirp SMF is 6.3 m, corresponding to a pre-chirp dispersion of -0.14 ps^2. The post-chirp SMF is reduced to 0.25 m from now on. The spectrum contains multiple peaks and the -10 dB spectral bandwidth is 66 nm. Pulse break-up occurs and multiple peaks appear in the autocorrelation trace. The pulsewidth is estimated as 346 fs. The spectrum of the frequency-doubled beam also has multiple peaks and the -10 dB spectral bandwidth is about 21 nm. Because of pulse break-up, the fundamental pulse cannot be compressed to transform-limited pulsewidth.

Figure 3.4(c) is the case when the pre-chirp SMF is 3.5 m, corresponding to a pre-chirp dispersion of -0.08 ps^2. The -10 dB spectral bandwidth of the fundamental beam is 90 nm and pulse break-up also exists. The pulsewidth is estimated as 328 fs. The spectrum of the frequency-doubled beam has multiple peaks and the -10 dB spectral bandwidth is about 27 nm.

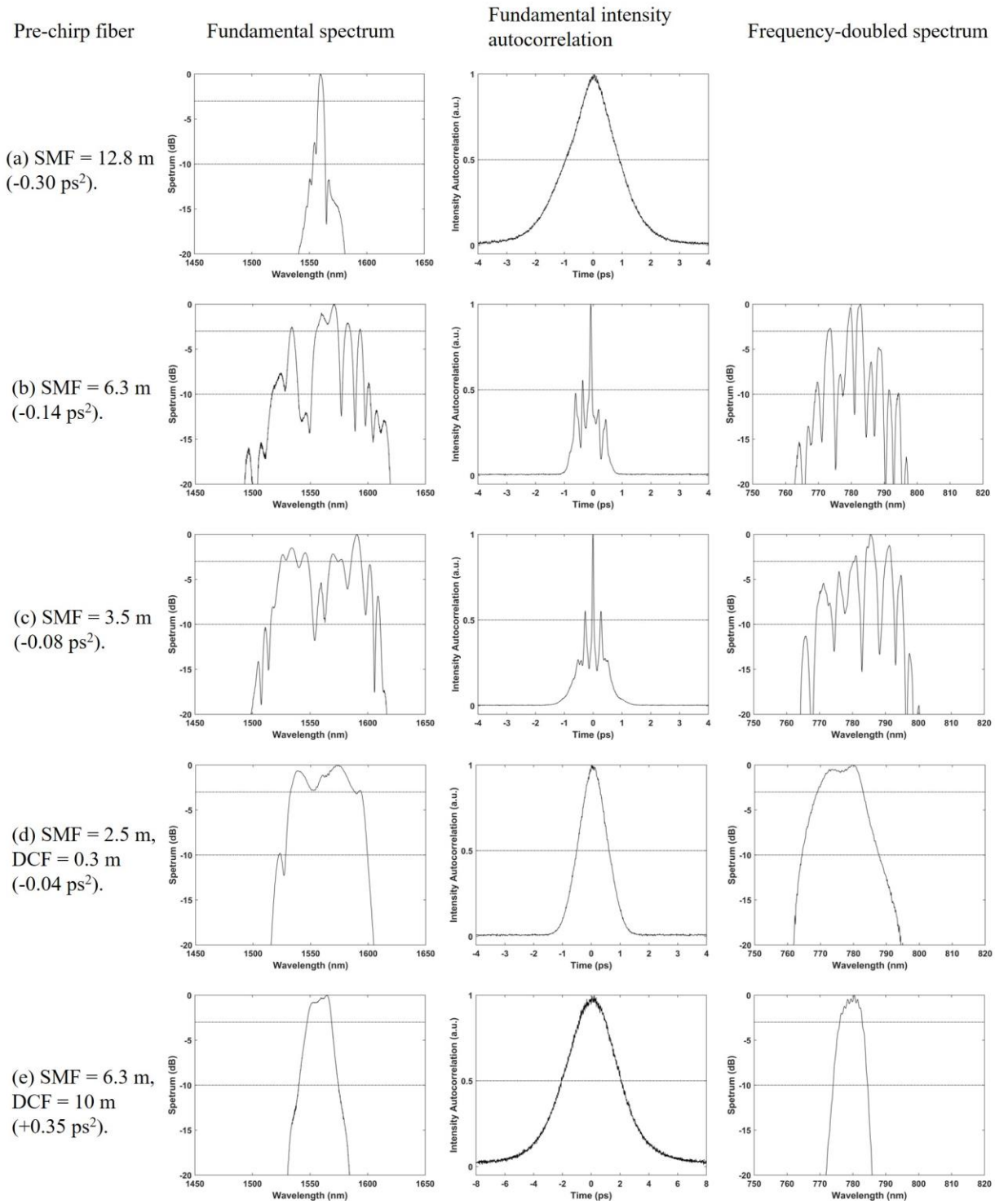

Figure 3.4 The spectra and intensity autocorrelation traces of the fundamental beam, and the corresponding spectra of the frequency-doubled beam, at different pre-chirp fiber lengths. (a) SMF = 12.8 m. (b) SMF = 6.3 m. (c) SMF = 3.5 m. (d) SMF = 2.5 m and DCF = 0.3 m. (e) SMF = 6.3 m and DCF = 10 m.

Figure 3.4(d) is the case when the pre-chirp fiber includes 2.5 m SMF and 0.3 m dispersion compensating fiber (DCF), corresponding to the pre-chirp dispersion of -0.04 ps^2. DCF (DCF38, Thorlabs) with GVD of +0.049 ps^2/m at 1560 nm is used to introduce positive dispersion in the pre-chirp part, because the SMF in the fiber-based components (such as isolator and coupler) cannot be too short in practice. The spectrum of the fundamental beam, in this case, is cleaner compared to the previous cases. The -10 dB spectral bandwidth is 82 nm and the FWHM spectral bandwidth is 53 nm, which is close to the acceptance bandwidth of the 0.3-mm-long PPLN. The pulsewidth of the fundamental beam is 1.1 ps. No pulse break-up is observed. The corresponding spectrum of the frequency-doubled beam is relatively smooth and the -10 dB spectral bandwidth is 25 nm. This is the optimal case for the 0.3-mm-long PPLN because it has no pulse break-up and has a clean spectrum which is close to the acceptance bandwidth of the PPLN. The optimal period found in the experiment is 19.70 μm which matches with the theoretical grating period at 1560 nm wavelength at room temperature (30 ˚C).

Figure 3.4(e) shows the case when the pre-chirp fiber includes 6.3 m SMF and 10 m DCF, corresponding to the pre-chirp dispersion of +0.35 ps^2. The -10 dB spectral bandwidth is narrowed to 34 nm. This spectrum is too narrow to fully use the PPLN. The amplified pulse has a broad pulsewidth of 4.1 ps. The -10 dB spectral bandwidth of the frequency-doubled beam is 11 nm.

Figure 3.5 summarizes the relationship between the pre-chirp dispersion and the properties of the amplified fundamental pulse and frequency-doubled pulse, respectively. The spectral bandwidth (circle) and pulsewidth (triangle) of the amplified fundamental pulse, and the spectral bandwidth of the frequency-doubled pulse (cross) are plotted as a function of the pre-chirp dispersion, which is calculated based on the lengths of the pre-chirp SMF and DCF. Two different post-chirp SMF lengths are used in the experiment. For pre-chirp $\leq$ -0.20 ps^2, the post-chirp SMF

is 0.9 m (data marked by open symbols). For pre-chirp ≥ -0.20 ps^2, the post-chirp SMF is 0.25 m (data marked by solid symbols). To investigate the effect of pre-chirp fiber on the amplified pulse, it is desirable to minimize the nonlinear broadening from the post-chirp fiber by shortening the post-chirp SMF.

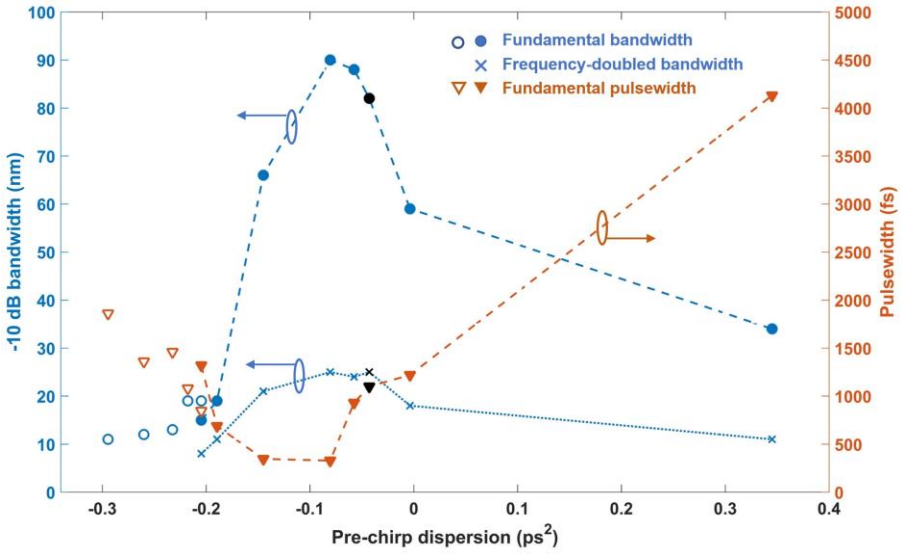

Figure 3.5 The spectral bandwidth (circle) and pulsewidth (triangle) of the amplified fundamental pulse, and the spectral bandwidth of the frequency-doubled pulse (cross**)**, at different pre-chirp dispersions. Solid symbols represent the data points with post-chirp SMF=0.25 m, and open symbols represent the data points with post-chirp SMF=0.9 m. The black symbols indicate the optimum case. The ellipses with arrows indicate the corresponding Y-axis of the curves.

In the EDF amplifier, the interplay between GVD and SPM determines the characteristics of the amplified pulse. For an initially negatively chirped pulse (acquired from the pre-chirp SMF), the negative chirp will be gradually compensated as the pulse propagates in the EDF. Thus, the pulse is compressed to reach a minimal pulsewidth when the pre-chirp is fully compensated, and afterward the pulse broadens again as it propagates in the remaining EDF. SPM induced spectral broadening is significant near the zero chirp position where minimal pulsewidth is reached.

Adjusting the pre-chirp fiber length can vary the position where the minimal pulsewidth occurs and thus controls the spectrum and pulsewidth of the amplified pulse. Several regions can be observed in Fig. 3.5.

When the pre-chirp dispersion is largely negative (< -0.2 ps^2), the amount of negative pre-chirp dispersion is much larger than the amount of positive dispersion in the EDF. The amplified pulse has broad pulsewidth (in the ps regime) during the passage through the entire EDF, and thus GVD dominates over SPM [88]. As a result, the spectral bandwidth of the amplified pulse is reduced due to gain narrowing and the pulsewidth is largely stretched.

When the pre-chirp dispersion is less negative (-0.2 ps^2 ~ -0.08 ps^2), the effect of SPM increases, which induces significant nonlinear phase shift. The fundamental spectrum becomes very broad and highly structured. In this regime, with 1.2 W pump power in total, the nonlinear phase shift becomes extremely high and pulse break-up occurs [48].

When the pre-chirp dispersion is slightly negative (-0.08 ps^2 ~ 0 ps^2), the minimal pulsewidth occurs in the first half of the EDF where the power is low or moderate. Thus the nonlinear phase shift is reduced and the amplified pulse has a spectrum with minimum structures, and pulse break-up is eliminated. This regime is close to parabolic amplification [89, 90]. This is the optimal operating region of the fiber amplifier and this case is highlighted by the black markers in Fig. 3.5.

When the pre-chirp dispersion is in the largely positive domain, it is in the parabolic amplification regime [89]. The pulsewidth is stretched into ps due to positive chirp, and thus GVD dominates over SPM [88]. The spectral bandwidth is significantly reduced due to gain narrowing. For all the cases, the bandwidth of the frequency-doubled beam shows a similar trend as the bandwidth of the fundamental beam.

3.2.5 Pulse compression

Based on the investigation above, the optimal pre-chirp is found for 2.5-m-long SMF and 0.3-m-long DCF. The corresponding spectra for the fundamental and frequency-doubled beams are shown in Fig. 3.4(d). The FWHM spectral bandwidth of the fundamental beam is 53 nm, which is close to the acceptance bandwidth of the 0.3-mm-long PPLN (42 nm FWHM). The amplified fundamental pulse is positively chirped with a broad pulsewidth of 1.1 ps.

For an initially linearly chirped Gaussian pulse, the incident filed can be written as $U(0,T)=\exp\left(-\frac{(1+iC)}{2}\frac{T^2}{T_0^2}\right)$, where T_0 is the half-width at 1/*e*-intensity point and *C* is the chirp parameter. The pulsewidth change due to GVD after propagating a distance *z* is given by [48]

$$\frac{T_1}{T_0}=\left[\left(1+\frac{C\beta_2 z}{T_0^2}\right)^2+\left(\frac{\beta_2 z}{T_0^2}\right)^2\right]^{1/2} \tag{3.12}$$

Here β_2 is the GVD parameter. Thus, the GVD-induced pulse broadening depends on the relative signs of β_2 and *C*. If $\beta_2 C>0$, a Gaussian pulse broadens monotonically. If $\beta_2 C<0$, the incident pulse goes through an initial narrowing stage. Since SMF has anomalous GVD at 1560 nm, it can be used to compress the fundamental pulse coming from the EDF amplifier. By adjusting the length of the post-chirp SMF and monitoring the pulsewidth, the optimum length of the post-chirp SMF is found to be 1.4 m when the minimal pulsewidth is achieved. Figure 3.6(a) shows the intensity autocorrelation of the fundamental pulse after SMF compression and it shows the FWHM pulsewidth of ~80 fs. Nevertheless, the autocorrelation trace also shows strong side peaks. The spectrum of the fundamental pulse after SMF compression is shown in Fig. 3.6(c) and the -10 dB bandwidth is 118 nm. Compared with the spectrum before SMF compression, the SPM introduced

by the post-chirp SMF broadens the fundamental spectrum and causes uneven structures. The central wavelength is slightly shifted to longer wavelength.

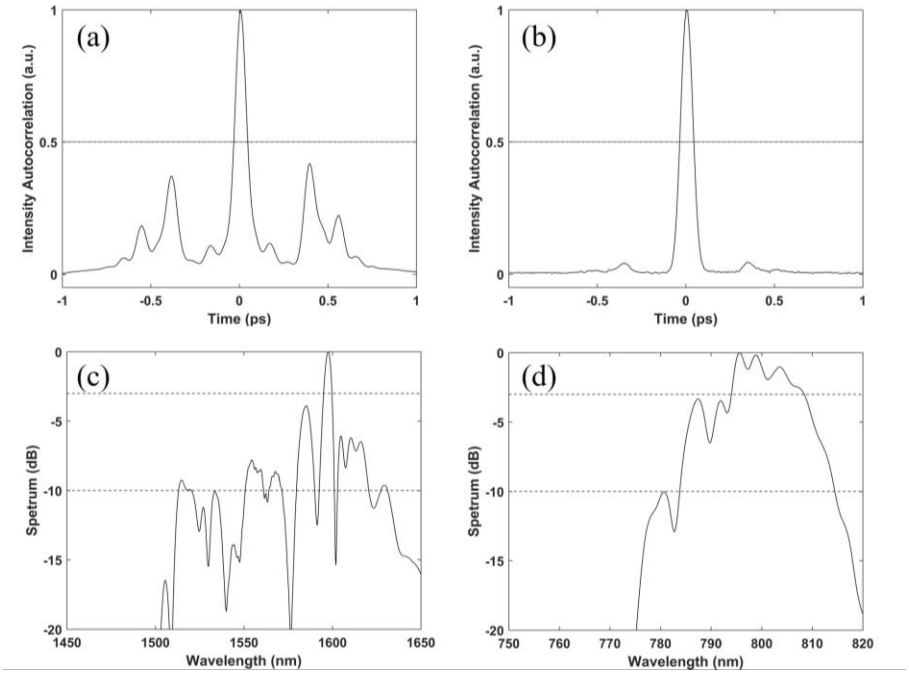

Figure 3.6 Characteristics of the pulse compressed by SMF. Intensity autocorrelation trace of the fundamental pulse (a) and frequency-doubled pulse (b). Spectrum of the fundamental pulse (c) and frequency-doubled pulse (d).

The intensity autocorrelation of the corresponding frequency-doubled pulse is shown in Fig. 3.6(b) and it shows the FWHM pulsewidth of 80 fs. A relatively clean autocorrelation trace with minimal side peaks is observed. The spectrum of the frequency-doubled pulse is shown in Fig. 3.6(d) and it shows the FWHM bandwidth of 15 nm. Comparing the frequency-doubled pulse with the fundamental pulse, both the autocorrelation trace and the spectrum are much cleaner without complicate structures. This is likely due to the limited acceptance bandwidth of the PPLN, which limits the bandwidth of the frequency-doubled pulse and cleans its pulse shape. The frequency-doubled pulse has a time-bandwidth-product of 0.59, which is nearly transform-limited. With SMF as the pulse compressor, effective pulse compression is achieved. The laser power right

before the PPLN is 170 mW and the output power of the frequency-doubled beam is 66 mW, and the power conversion efficiency is 39%.

To compare the pulse quality after SMF compression with the compression method of free-space optics, the pulse is also compressed by a silicon prism pair (Crystran). The intensity autocorrelation and spectrum of the compressed fundamental pulse and the corresponding frequency-doubled pulse are shown in Fig. 3.7. The pulsewidth of the compressed fundamental pulse and frequency-doubled pulse are 100 fs and 80 fs, respectively. The FWHM bandwidth of the compressed fundamental pulse and frequency-doubled pulse are 52 nm and 12 nm, respectively. The spectrum of the compressed fundamental pulse is similar to the pulse spectrum before compression. The laser power right before the PPLN is 150 mW and the output power of the frequency-doubled beam is 60 mW, and the power conversion efficiency is 42%.

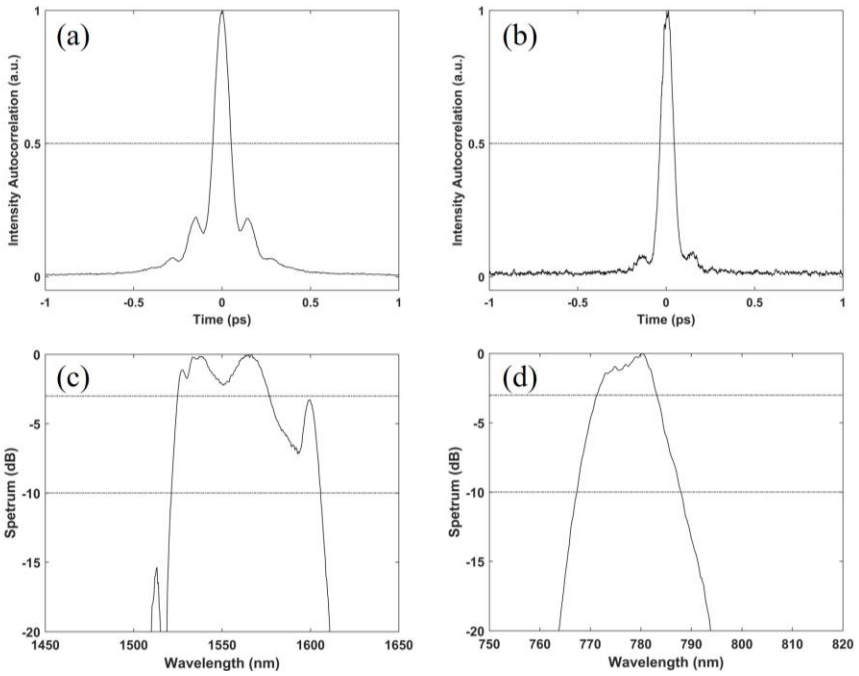

Figure 3.7 Characteristics of the pulse compressed by silicon prism pair. Intensity autocorrelation trace of the fundamental pulse (a) and frequency-doubled pulse (b). Spectrum of the fundamental pulse (c) and frequency-doubled pulse (d).

Comparing the pulse compression by SMF versus prism pair, SMF introduces a significant amount of nonlinearity due to SPM, and the prism-pair compression is almost linear with no additional nonlinearity. Nevertheless, as the frequency-doubling only happens within the acceptance bandwidth of the PPLN, the frequency-doubled pulse can still achieve a similar pulsewidth and bandwidth as the results achieved by prism pair. Furthermore, using SMF compression, the Er-doped fiber laser and the MPM endoscopy imaging head can be connected directly via the post-chirp SMF, which makes the whole system highly compact and portable.

Table 3.1 summarizes the characteristics of the fundamental and frequency-doubled pulses using the 0.3-mm-long PPLN and 1-mm-long PPLN [85]. The pulsewidth of the frequency-doubled pulse is reduced from 150 fs to 80 fs when the PPLN length is reduced from 1 mm to 0.3 mm. However, the conversion efficiency is nearly equal. The similar conversion efficiency is consistent with our theoretical analysis that the output power of the PPLN does not depend on the PPLN length. Since the MPM intensity is inversely proportional to the excitation pulsewidth, the MPM intensity is expected to increase by 2-3 times when the PPLN length is reduced from 1 mm to 0.3 mm, under the same average power. The experimental pulsewidth of the fundamental and frequency-doubled pulses using the 0.3-mm-long and 1-mm-long PPLN [85], respectively, are also compared with the theoretical results in Fig. 3.2 (marked by solid and open circles for the fundamental pulse and the frequency-doubled pulse, respectively). For the 0.3-mm-long PPLN, the measured pulsewidth matches reasonably well with the theoretical estimation. In our previous study using the 1-mm-long PPLN in Ref. [85] shown as the last row in Table 3.1, both the fundamental and frequency-doubled pulses had large side peaks. The measured pulsewidths only considered the main peak. Therefore, the measured pulsewidths were underestimations of the actual pulsewidths.

Table 3.1 Summary of pulse characteristics obtained by the 0.3-mm and 1-mm PPLN.

PPLN length (mm)	Acceptance bandwidth (nm)	Pulse compression	Fundamental beam			Frequency-doubled beam		Power conversion efficiency
			Bandwidth (nm)		Pulsewidth (fs)	FWHM Bandwidth (nm)	Pulsewidth (fs)	
			FWHM	-10 dB				
0.3	42	Silicon prism	52	84	100	12	80	42%
		SMF		118	80	15	80	39%
1.0 (**[85]**)	12	SMF	8	60	250	5	150	40%

3.3 MPM imaging

The optimized fiber laser system is used as the excitation source for the miniature MPM endoscopy system shown in Fig. 3.1. To characterize the imaging uniformity, MPM imaging of fluorescent solution (Fluorescein, ThermoFisher) is acquired where the sample is assumed to be uniform. Figs. 3.8(a)-3.8(d) show the MPM images obtained at 0.4, 0.8, 2, and 4 frames/s, respectively. When the frame rate is 0.4, 0.8, and 2 frames/s, the images show good uniformity over the entire FOV. When the frame rate is increased to 4 frames/s (1 μs/pixel dwell time), the image is slightly darker due to reduced signal-to-noise ratio (SNR). The scanning speed of the fast axis (X-axis) in the MEMS mirror is increased to 977 Hz. Since the resonant frequency of the MEMS mirror is ~1500 Hz, the scanner is operated close to resonant scanning. Thus, the image displays a slightly larger FOV, which could slightly reduce the power throughput in the illumination path and/or reduce the collection efficiency. Therefore, the image at 4 frames/s shown in Fig. 3.8(d) displays slight non-uniform at the corners.

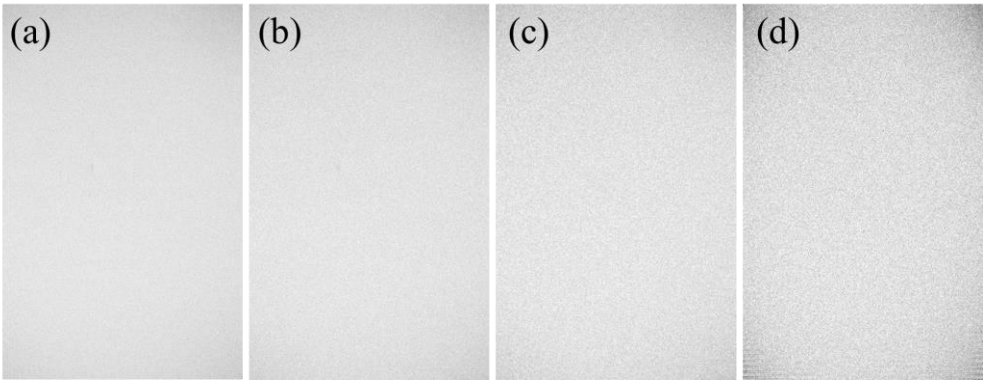

Figure 3.8 (a)-(d) MPM images of fluorescent solution at 0.4, 0.8, 2, and 4 frames/s, respectively. With the uniform fluorescent solution sample, the uniformity of the FOV is evaluated. FOV in (a)-(c) is 160 μm × 250 μm. The FOV in (d) is slightly larger due to the higher scanning speed which is close to resonance scanning.

The system is applied to image *ex vivo*, unprocessed (unstained and unfixed) biological tissue samples. With shorter pulse, higher MPM excitation efficiency can be obtained, which is critical for MPM imaging of native signals in tissues. With higher MPM excitation efficiency, the pixel dwell time can be reduced and the imaging speed can be increased, correspondingly. To test this, four different pixel dwell times of 10, 5, 2, and 1 μs/pixel, which corresponds to four different frame rates of 0.4, 0.8, 2, and 4 frames/s, are applied to image the tissue samples. The MPM images of the mouse (CD-1 strain) skin and kidney are shown in Fig. 3.9. The average excitation power at the sample is about 40 mW. Figs. 3.9(a)-3.9(d) display the MPM images of the dermal layer in the murine skin, in which the hair follicle and collagen fibers can be distinguished clearly. Figs. 3.9(e)-3.9(h) display the MPM images of intracellular flavins of epithelial cells of the murine kidney tubules [37], in which the epithelial cells can be clearly seen.

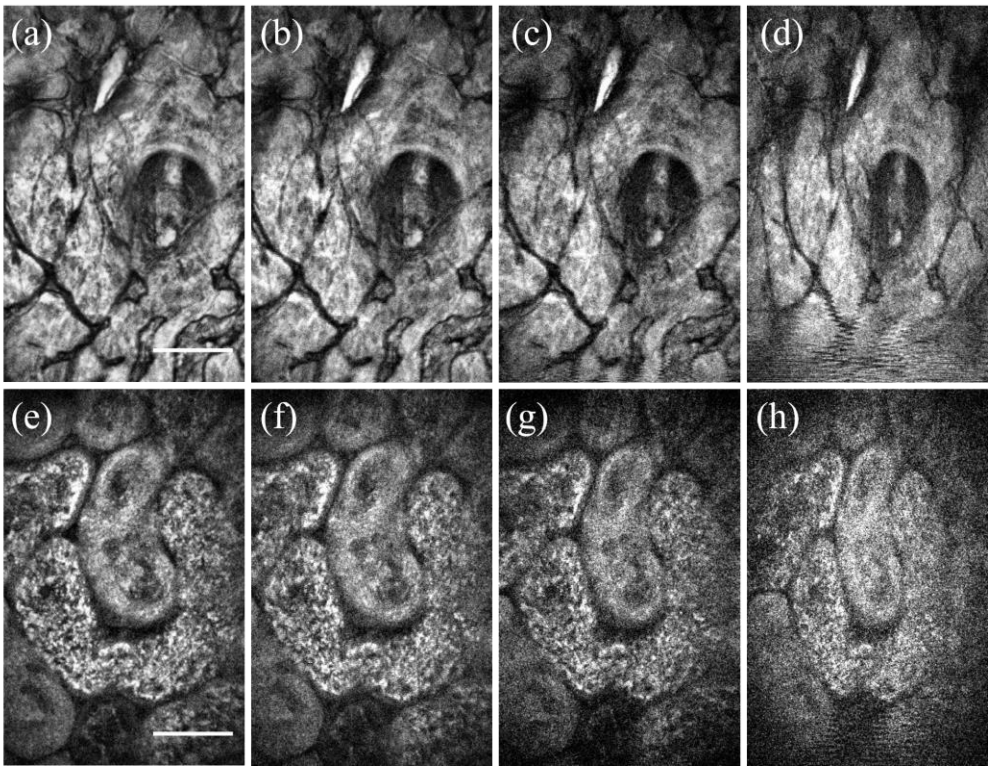

Figure 3.9 (a)-(d) MPM images of the murine skin at 0.4, 0.8, 2, and 4 frames/s, respectively. (e)-(h) MPM images of the murine kidney at 0.4, 0.8, 2, and 4 frames/s, respectively. FOV in (a)-(c) and (e)-(g) is 160 μm × 250 μm. The FOV in (d) and (h) is slightly larger due to the higher scanning speed which is close to resonance scanning. Scale bar is 50 μm.

When the pixel dwell time is reduced from 10 μs/pixel to 1 μs/pixel, there are still reasonable MPM signals to show the tissue structures. In our previous work on MPM endoscopy with 1-mm-long PPLN [85], the imaging speed is limited to 0.4 frames/s (10 μs/pixel) due to the relatively low MPM excitation efficiency. After optimizing the laser system to reduce the pulsewidth and improve the temporal quality of the pulse, the imaging speed is significantly increased by almost 10 times and an imaging speed of 4 frames/s (1 μs/pixel) is achieved. Figs. 3.9(d) and 3.9(h) display distortions induced by the MEMS scanner near the bottom of the images and show slightly larger imaging range along the fast axis since the scanner is operated close to

resonant scanning. In the future, in order to achieve real-time imaging, MEMS scanner with a higher scanning speed will be required.

Figure 3.10 shows the averaged MPM intensity versus pixel dwell time. Here the averaged intensity is calculated from a murine skin sample. The MPM intensity (in photon counts) is calculated by averaging over the pixels which have the intensity value higher than 10% of the maximum intensity. It shows that the MPM intensity is almost linearly proportional to the pixel dwell time. Correspondingly, the MPM intensity is almost inversely proportional to the frame rate because the pixel dwell time and frame rate are reciprocal. Although the MPM intensity drops to 10% when the pixel dwell time is reduced from 10 μs/pixel to 1 μs/pixel, the average MPM intensity is still around 14 counts which is four times higher than the average noise background (~3 counts). Thus, there are still reasonable MPM signals to show the tissue structure.

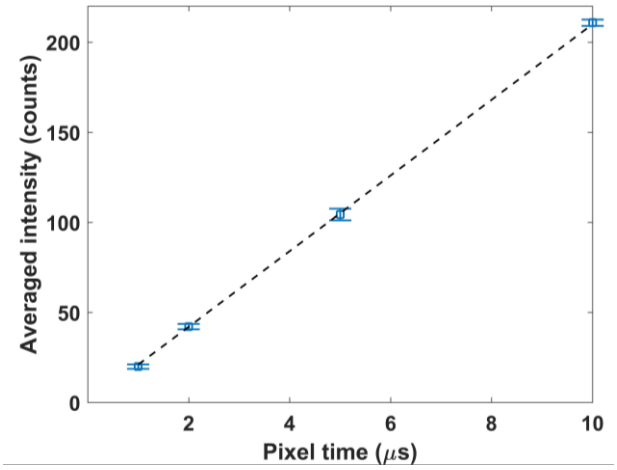

Figure 3.10 Averaged MPM intensity versus pixel dwell time. The dashed line represents a linear fitting.

In this chapter, the reported system optimization is on the laser source and particularly shortening the pulsewidth. As the pulsewidth gets shorter, the nonlinear effect becomes more significant. Thus other optimization approaches also need to be considered to further increase the imaging speed. Improving the focusing quality of the miniature objective lens will be an important

approach. Objective lens with higher NA and lower distortion can potentially reduce the spot size and thus increase the MPM excitation efficiency. From Eq. (3.1), the MPM intensity is proportional to the fourth power of NA. The current objective lens is a single-element aspherical lens with NA = 0.5. The NA could be increased to 1.0 by using custom-designed, multiple-element apochromatic lens. Therefore, the MPM intensity can be potentially increased by 16 times, and the imaging speed can be largely increased and potentially reach video rate at 24 frames/s. This will enable our MPM endoscopy system for *in vivo* imaging and clinical applications.

3.4 Conclusions

Developing miniature MPM endoscopy that can be used for clinical applications requires compact laser source and fast imaging speed. The frequency-doubled Er-doped fiber laser is shown to be a great choice for such purpose. To increase the imaging speed, system optimization is carried out by reducing the pulsewidth of the excitation source. It is found that the pulsewidth of the frequency-doubled output depends linearly on the PPLN length while the output power is irrelevant with the PPLN length. By choosing a 0.3 mm thickness of the PPLN and matching the bandwidth of the fundamental beam with the acceptance bandwidth of the PPLN, frequency-doubled pulse with the pulsewidth of 80 fs is achieved. Through the systematic optimization, high MPM excitation efficiency is obtained and imaging speed at 4 frames/s is demonstrated on e*x vivo* imaging of unstained biological tissues. This speed is 10 times faster than our previously reported study. Furthermore, pulse compression with SMF is achieved, which makes the system highly compact. The results show that miniature MPM endoscopy with the frequency-doubled Er-doped fiber laser can potentially translate MPM imaging technology for clinical applications.

Chapter 4: Miniature multiphoton endoscopy with dual-wavelength Er-doped fiber laser for simultaneous label-free two-photon and three-photon imaging

4.1 Introduction

Multiphoton microscopy (MPM) is a laser-scanning microscopy technique based on exciting and detecting nonlinear optical signals from tissues [1, 2]. It is considered as one of the best noninvasive means of biological imaging microscopy in tissues and live animals [2], and it has been widely used in cancer detection and brain imaging [91, 92]. Typical MPM performs two-photon microscopy (2PM) imaging, including two-photon excitation fluorescence (TPEF) [1] and second harmonic generation (SHG) [93]. TPEF is a primary signal source in MPM [2], which originates from the intrinsic fluorophores of tissues, such as nicotinamide adenine dinucleotide hydrogen (NADH), flavin adenine dinucleotide (FAD), and elastin, and exogenous fluorophores by staining the tissue using various fluorescent dyes [1]. SHG, on the other hand, is an intrinsic signal induced by nonlinear scattering and does not involve the absorption of photons. Therefore, SHG imaging should not suffer from photo-toxicity or photo-bleaching, while both of those could affect TPEF imaging in live specimens [3]. However, SHG occurs only in ordered non-centrosymmetric structures, which limits SHG signal generation mostly to fibrillar collagen and striated muscle myosin in mammalian soft tissues [93]. Three-photon microscopy (3PM) imaging, such as three-photon excitation fluorescence (3PEF) and third harmonic generation (THG), has also been developed. 3PM uses longer excitation wavelength than 2PM in the near-infrared (NIR) region, which exhibits deeper penetration depth due to reduced scattering. 3PEF has the same origin as TPEF but lower excitation efficiency [94]. THG is another type of label-free imaging and

is generated from optical heterogeneities [25], such as at the interface between an aqueous medium and a lipidic, mineralized, or absorbing structure [26]. THG does not require the non-centrosymmetric structure as in SHG or fluorescence molecule as in TPEF. Thus, THG signal is more versatile compared to SHG and TPEF signals, and THG can be obtained from many structures in cells and tissues. In general, 3PM has lower excitation efficiency than 2PM due to its higher order nonlinear effects. For *in vivo* imaging on patients and imaging live cells and tissues, label-free imaging, such as TPEF, SHG and THG, is very important.

Multimodal MPM, which combines 2PM and 3PM, is currently a new trend for *in vivo* imaging and clinical applications because it can acquire complementary information about tissues simultaneously. N. Olivier *et al*. designed a multimodal MPM including TPEF, SHG, and THG as a novel tool for investigating cellular behavior in developmental biology [26]. Using transgenic embryo, TPEF from cell nuclei, SHG from mitotic spindles, and THG from cell walls were imaged and correlated with cell mitosis phases. Multimodal MPM combining TPEF, SHG, and THG, was also demonstrated by B. Weigelin *et al*. to investigative cancer cell invasion [95]. SHG showed collagen fibers and striated muscle myosin. THG detected cell and tissue interfaces, including adipocytes, nerve fibers, and blood vessels. TPEF was excited from fluorescence staining and green fluorescence protein (GFP), which labeled tumor cytoplasm, tumor nuclei, and blood vessels. Thus, the multimodal MPM allowed a comprehensive study of cancer cell invasion. Multimodal MPM combining SHG and THG was reported by S. Dietzel *et al*. to characterize microcirculation in animal models [31]. In their work, SHG from striated muscle myosin and collagen fibers in arterioles, and THG from nerve fibers and red blood cells in arterioles and venules, were detected for intravital determination of hemodynamic parameters. Therefore, multimodal MPM with both 2PM and 3PM is a powerful tool for label-free imaging, which can

acquire multiple contrasts simultaneous for obtaining comprehensive information about cells and tissues.

Laser system design is a primary challenge in multimodal MPM instrumentation. Two types of laser systems have been used in multimodal MPM. The first type is a single wavelength femtosecond laser in the 1.0-1.7 μm range for exciting 2PM and 3PM signals simultaneously [95-97]. Benchtop multimodal MPM systems with excitation wavelength at 1180 nm were developed to investigate bone [95] and skin [96]. Fluorescence staining was required for TPEF imaging due to the long excitation wavelength. The single excitation wavelength was achieved by a Ti:Sapphire laser pumping an optical parametric oscillator (OPO), which was bulky and costly [95, 96]. K. Kieu *et al.* demonstrated a multimodal MPM using Er-doped fiber laser with a single excitation wavelength of 1560 nm, where the fiber laser was fiber-coupled to a multiphoton microscope [97]. However, the major limitation of those single wavelength laser in the 1.0-1.7 μm range is that intrinsic TPEF signal from tissues such as NADH and elastin cannot be excited due to the long wavelength. To excite intrinsic TPEF signal in tissues, a shorter than 900 nm wavelength is required [24]. The second type of laser system used in multimodal MPM is dual-wavelength laser source [98-101]. In dual-wavelength laser source, a longer wavelength (>1 μm) excites 3PM signals such as 3PEF and THG, and a shorter wavelength (<1 μm) excites 2PM signals such as TPEF and SHG. Dual-wavelength laser excitation has been achieved by tuning a Ti:Sapphire laser with OPO to two different wavelengths [98-100]. For example, previously reported dual-wavelength sources used tunable wavelengths at 1180-nm for 3PM and 860-nm for 2PM [99]; 1300-nm for 3PM and 920-nm for 2PM [98]; and 1200-nm for 3PM and 800-nm for 2PM [100]. Alternatively, dual-wavelength laser source has also been achieved by using two lasers with different working wavelengths [101]. D. Small *et al.* reported a multimodal MPM system based

on two lasers – a Ti:Sapphire laser at 810 nm for 2PM and a soliton self-frequency shift of fiber laser at 1700 nm for 3PM [101]. However, a major challenge of the current dual-wavelength excitation sources (a laser plus OPO or two lasers) is that the whole laser system is highly complicated and bulky, which limits the clinic application of multimodal MPM.

For clinical application and *in vivo* imaging, a compact multimodal MPM endoscopy is needed. Recently, a multimodal MPM endoscopy with an excitation wavelength at 1700 nm was presented by F. Akhoundi *et al*. [102]. The laser system was designed by applying soliton self-frequency shift to an Er-doped fiber laser. Inside the MPM endoscope, a miniature objective lens was attached to and scanned by a piezoelectric tube. The imaging speed was limited to 15 seconds per frame due to the heavy load of the objective lens, which was very slow and not suitable for *in vivo* imaging. Moreover, the 1700 nm wavelength could not excite intrinsic TPEF from tissues.

In this chapter, we propose a multimodal MPM endoscopy based on a dual-wavelength Er-doped fiber laser. The dual-wavelength laser provides fundamental pulse from the fiber laser at 1580 nm and frequency-doubled pulse at 790 nm. The 1580-nm pulse is used to excite THG, and the 790-nm pulse is used to excite TPEF and SHG. Since most intrinsic fluorophores in tissue have a two-photon absorption peak at shorter than 900 nm wavelength [24], this system can excite intrinsic TPEF signals from biological tissues, such as NADH and elastin. The Er-doped fiber laser is directly coupled via a single mode fiber (SMF) to the MPM endoscopy imaging head and the frequency-doubling of the pulse is achieved inside the distal end of the probe, which makes the entire system highly compact and portable. Label-free imaging on *ex vivo* samples of murine skin and femur bone, and rabbit femur bone are carried out, which demonstrate multiple imaging contrasts, including TPEF, SHG, and THG. These results demonstrate the capability and potential of the multimodal MPM endoscopy for future clinical applications.

4.2 System design

4.2.1 System configuration

Figure 4.1 shows the schematic diagram of the miniature multimodal MPM endoscopy. The details of the MPM endoscopy for 2PM can be found in Chapter 3. An Er-doped fiber laser delivers femtosecond pulse at 1580-nm to the miniature MPM endoscopy through a SMF. The 1580 nm pulse is frequency-doubled into 790 nm pulse by a periodically poled MgO:$LiNbO_3$ (PPLN) in the distal end of the endoscope. Dual-wavelength source is obtained after the PPLN, which includes the frequency-doubled pulse at 790 nm, and the residual fundamental pulse at 1580 nm. For 2PM including intrinsic TPEF and SHG imaging, 790-nm pulse is utilized as the excitation source. It is selected by a glass bandpass filter (RG9, Schott) which has the transmission window of 700-1050 nm. For 3PM such as THG imaging, the residual 1580-nm pulse is utilized as the excitation source. It is selected by a glass longpass filter (FGL1000, Thorlabs) which has the edge wavelength of 1000 nm. The glass filters RG9 and FGL1000 are switched when performing 2PM and 3PM sequentially. A 2.4-mm-diameter 2D micro-electro-mechanical system (MEMS) mirror (Mirrocle Tech., Inc.) is used to raster scan the beam. Two identical Ø1/2" achromatic doublets (AC127-019-A, f = 19.0 mm, Thorlabs) are used to relay the beam from the MEMS scanner to the miniature objective lens. An aspheric lens C150TME-A (f = 2.0 mm, NA = 0.50, Thorlabs) is used as the objective lens.

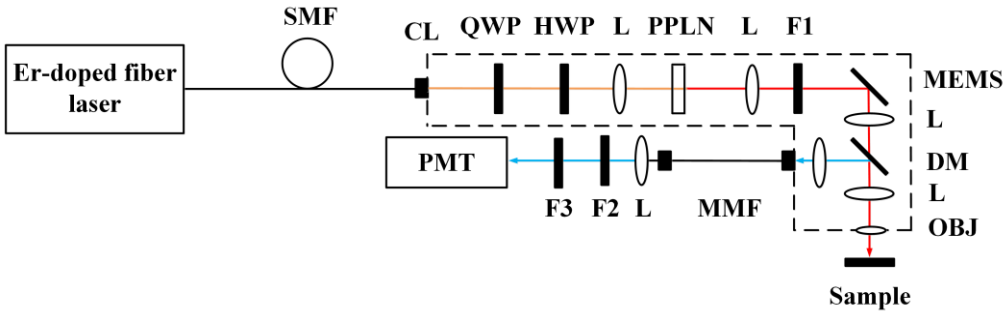

Figure 4.1 Schematic of the miniature multiphoton endoscopy with a dual-wavelength Er-doped fiber laser. SMF: single mode fiber; CL: collimating lens; HWP: half-wave plate; QWP: quarter-wave plate; L: lens; PPLN: periodically poled MgO:$LiNbO_3$ crystal; F: filter; MEMS: micro-electro-mechanical system mirror; DM: dichroic mirror; OBJ: objective lens; MMF: multimode fiber; PMT: photomultiplier tube.

The emitted TPEF/SHG/THG signals are collected in the backward direction and separated from the excitation light by a longpass dichroic mirror with the edge wavelength of 665 nm (FF665-Di02, Semrock). The signals are coupled by an achromatic doublet (AC050-008-A, f = 7.5 mm, Thorlabs) into a multimode fiber (MMF) patch cable (Ø1500 μm, NA = 0.39, Thorlabs), and sent to a photomultiplier tube (PMT) (H9305-03, Hamamatsu). A blocking filter with a passband from 350-650 nm (FF01-680/SP, Semrock) is placed in front of the PMT to remove the residual back-reflected excitation light. To select the different signals, another filter is placed in front of the PMT. TPEF signal is selected by a bandpass filter of 550 ± 44 nm (FF01-550/88, Semrock). SHG signal is selected by a bandpass filter of 390 ± 20 nm (FF01-390/40, Semrock). THG signal is selected by a bandpass filter of 520 ± 17.5 nm (FF01-520/35, Semrock). The field of view (FOV) of the MPM system is 160 μm × 250 μm (328 pixels × 512 pixels).

4.2.2 Design considerations

The spectral relationship among the two excitation wavelengths and the emitted TPEF, SHG and THG signals are illustrated in Fig. 4.2. The insert in Fig. 4.2 shows the measured spectrum (ANDO AQ6317B) of the dual-wavelength source, which includes the residual fundamental beam at 1580 nm and the frequency-doubled beam at 790 nm. Light delivered by the SMF is usually elliptically polarized. Controlled by the half-wave plate (HWP) and quarter-wave plate (QWP), the polarization of the 1580 nm pulse is adjusted to be linearly polarized (e-polarization) to achieve a maximum power conversion efficiency in the PPLN crystal. The 790 nm pulse has the same linear polarization as the 1580 nm pulse. The 790-nm pulse is utilized to excite TPEF from 450-650 nm and SHG at 395 nm, and the 1580-nm pulse is utilized to excite THG at 527 nm. The THG wavelength overlaps with the TPEF wavelength range. In sequential excitation by switching on the 790 and 1580 nm light respectively, the THG and TPEF do not occur at the same time. In the current experiment, SHG and THG signals are excited by a fixed linear polarization. Polarization-sensitive SHG and THG can potentially be achieved by adding a corresponding HWP before the objective lens to rotate the polarization state of the laser beams.

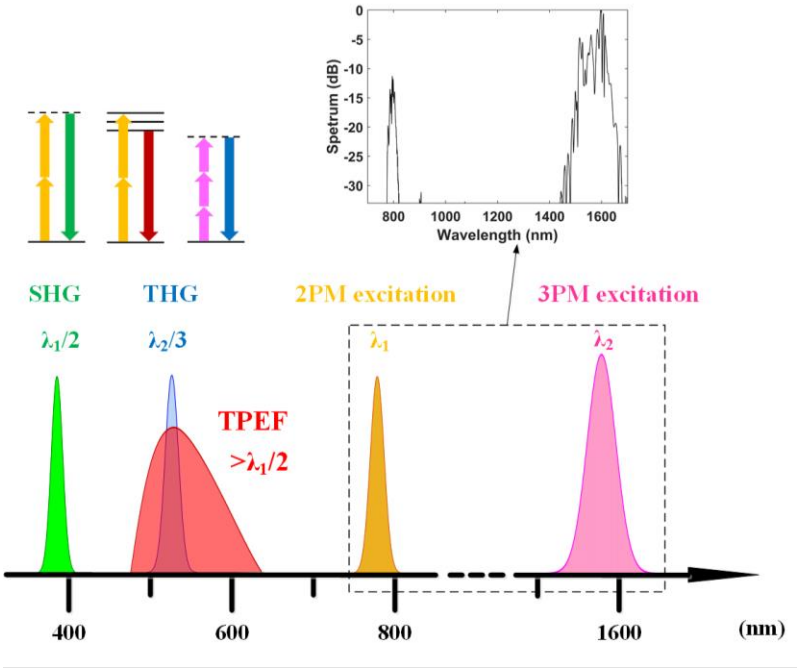

Figure 4.2 Illustration of the spectral relationship of the excitation and emission wavelengths involved in the multimodal MPM imaging. Top left insert shows the energy diagrams of SHG, TPEF, and THG processes. Top right insert is the measured spectrum of the dual-wavelength laser source.

The characteristics of the dual-wavelength source at 1580-nm and 790-nm are shown in Table 4.1. The output power of 790-nm pulse after the PPLN is ~66 mW. The residual power of 1580-nm pulse after the PPLN is ~75 mW. The pulsewidth of the 1580-nm and 790-nm pulses are both 80 fs. The short pulsewidth is achieved after using a piece of SMF to compensate the dispersion in the Er-doped fiber laser system. The -10 dB bandwidth is characterized due to the multiple-peak structure in the spectrum. The -10 dB bandwidth of the 1580-nm and 790-nm pulses are 118 nm and 34 nm, respectively.

Table 4.1 Comparison of laser specifications.

	Frequency-doubled beam	**Residual fundamental beam**
Excitation wavelength (nm)	790	1580
Power after PPLN	66	75
Pulsewidth (fs)	80	80
-10 dB bandwidth	34	118

The dual-wavelength source passes through multiple optical components, including MEMS scanner, scan lens, dichroic mirror, tube lens, and objective lens. Those components introduce transmission loss due to surface reflectivity which is wavelength dependent. Table 4.2 shows the power budget calculation for the 1580-nm and 790-nm pulses based on the component reflectivity and transmission from their specifications. The MEMS mirror includes a gold mirror (96% reflectance) and an A-coating glass window. A-coating provides low reflectance for the 350-700 nm range. For 790 nm and 1580 nm, 4% reflectance at each glass/air interface is assumed. Similarly, the scan lens, tube lens, and objective lens all have A-coating, and 4% reflectance at each glass/air interface is assumed. The dichroic mirror has a transmission of 94% and 96% at 790 nm and 1580 nm, respectively. Therefore, the estimated total power throughput due to reflection loss is 60% for 790-nm and 61% for 1580-nm, respectively. The power throughput is also characterized by measuring the power after the objective lens. The experimentally measured total power throughput is 61% for 790-nm and 40% for 1580-nm, respectively. For the 790-nm pulse, the experimentally measured power throughput matches with the estimated power throughput.

However, for the 1580-nm pulse, the experimentally measured power throughput is much lower than the estimated power throughput. It is found that the 1580-nm beam has a larger beam size than the 790-nm beam. When the beam size of the 790 nm pulse is designed to match with the size of the MEMS mirror (2.4 mm diameter), the 1580 nm beam would suffer from higher power loss due to clipping of the beam by the limited size of the MEMS mirror.

Table 4.2 Power throughput calculation for 1580-nm and 790-nm beams.

	Transmission of 790-nm pulse	**Transmission of 1580-nm pulse**
MEMS mirror (Au mirror, A-coating glass window)	0.96^5	0.96^5
Scan lens (A-coating)	0.96^2	0.96^2
Dichroic mirror	0.94	0.96
Tube lens (A-coating)	0.96^2	0.96^2
Objective lens (A-coating)	0.96^2	0.96^2
Theoretical total power throughput	**0.60**	**0.61**
Measured total power throughput	**0.61**	**0.40**

To investigate the beam size variation of the 1580-nm and 790-nm beams, theoretical calculation is carried out to consider frequency-doubling in the PPLN and Gaussian beam propagation in the lens system. The optical layout of the frequency-doubling unit is illustrated in Fig. 4.3. The 1580-nm beam is focused into the PPLN by the focusing lens. The 790-nm beam is

generated by frequency-doubling of the fundamental beam in the PPLN. The 790 and 1580 nm beams are collimated by the collimation lens and then shine on the MEMS mirror.

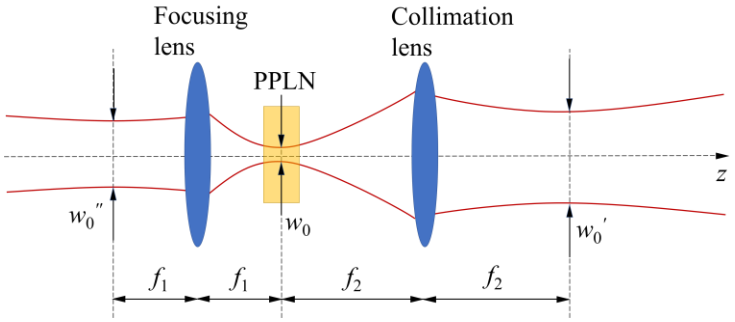

Figure 4.3 Optical layout of the frequency-doubling showing Gaussian beam propagation.

Based on the theory of frequency-doubling, the frequency-doubled beam has a smaller beam waist than the fundamental beam by a factor of $1/\sqrt{2}$ [49]

$$w_{0(2\omega)} = \frac{w_{0(\omega)}}{\sqrt{2}} \tag{4.1}$$

The beam waist w_0 is obtained at the focal plane of f_1 inside the PPLN. After the collimation lens, the beam waist w_0' at the position of f_2 can be obtained by ABCD matrix and the complex beam parameter of Gaussian beam. The complex beam parameter at the beam waist w_0 position is $q_0 = \frac{i\pi w_0^2}{\lambda}$ [103]. The complex beam parameter at the beam waist w_0' position is q_0'.

According to the ABCD rule [103], the ABCD matrix from position w_0 to position w_0' is given by

$$\begin{pmatrix} A & B \\ C & D \end{pmatrix} = \begin{pmatrix} 1 & f_2 \\ 0 & 1 \end{pmatrix} \begin{pmatrix} 1 & 0 \\ -\frac{1}{f_2} & 1 \end{pmatrix} \begin{pmatrix} 1 & f_2 \\ 0 & 1 \end{pmatrix} = \begin{pmatrix} 0 & f_2 \\ -\frac{1}{f_2} & 0 \end{pmatrix} \tag{4.2}$$

Therefore, at the position of the new beam waist w_0' after the collimation lens, we can get

$$q_0^{'} = \frac{Aq_0 + B}{Cq_0 + D} = \frac{f_2}{-q_0 / f_2} = i\frac{\lambda f_2^2}{\pi w_0^2} \tag{4.3}$$

Since $q_0^{'} \equiv \frac{i\pi w_0^{'2}}{\lambda}$, the beam waist after the collimation lens is

$$w_0^{'} = \frac{\lambda f_2}{\pi w_0} \tag{4.4}$$

The beam waist after the collimation lens is linearly proportional to λ and inversely proportional to the beam waist at the focal point in the PPLN.

Similarly, the beam waist $w_0^{"}$ at the input side can be obtained and we get the following relationship

$$w_0^{'} = \frac{f_2}{f_1} w_0^{"} \tag{4.5}$$

In our experiment, the input fundamental beam has a beam waist $w_{0(\omega)}^{"}$ =1 mm, f_1 = 7.5 mm, and f_2 = 11 mm. Thus, the beam waist of the fundamental beam inside the PPLN is $w_{0(\omega)} = 3.77\ \mu m$, and after the collimation lens is $w_{0(\omega)}^{'} = 1.47\ mm$. The beam waist of the frequency-doubled beam inside the PPLN should be $1/\sqrt{2}$ smaller than that of the fundamental beam and thus we can get $w_{0(2\omega)} = 2.67\ \mu m$. The beam waist of the frequency-doubled beam after the collimation lens should be $w_{0(2\omega)}^{'} = 1.04\ mm$. The Rayleigh range of the Gaussian beam after the collimation lens is $z_R^{'} = \frac{\pi w_0^{'2}}{\lambda}$. Both the fundamental and frequency-doubled beams have the same Rayleigh range.

The beam radius after a distance *z* from the beam waist can be calculated by [103]

$$w'(z) = w_0' \left[1 + \left(\frac{z}{z_R'} \right)^2 \right]^{1/2} \tag{4.6}$$

At far field where $z \gg z_R'$, the beam radius is $w'(z) = w_0' \frac{z}{z_R'} = \frac{\lambda}{\pi w_0'} z$. The divergence angle is $\theta = \frac{\lambda}{\pi w_0'}$ [104], which is linearly proportional to λ and inversely proportional to w_0'. Thus, for the fundamental beam and frequency-doubled beam, the divergence angle has a relationship of $\frac{\theta_{(\omega)}}{\theta_{(2\omega)}} = \sqrt{2}$, which indicates that the fundamental beam diverges faster than the frequency-doubled beam at far field. The Gaussian beam width of the fundamental beam and frequency-doubled beam versus the axial distance *z* are plotted in Fig. 4.4. The beam radius of the fundamental beam (blue line) is $\sqrt{2}$ times larger than that of the frequency-doubled beam (red line) at the beam waist position and at far field position.

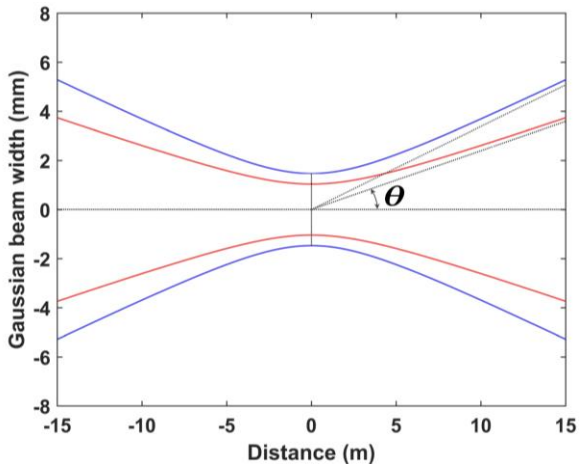

Figure 4.4 Gaussian beams of the fundamental beam (blue) and frequency-doubled beam (red).

In the experiment, the MEMS mirror is positioned near z = 30 cm, which is within the calculated Rayleigh range $z'_{R(\omega,2\omega)} = 4.3\ \mathrm{m}$. At the MEMS mirror position, the frequency-doubled beam is calculated to have a diameter of 2.08 mm, and the fundamental beam has a diameter of 2.94 mm. Compared with the MEMS mirror diameter of 2.4 mm, the fundamental beam is partially clipped by the MEMS mirror and thus higher loss is introduced. The power throughput due to clipping of the fundamental beam is estimated as $1-e^{-2(\frac{2.4}{2.94})^2} = 74.0\%$. Therefore, the theoretical total power throughput for the fundamental beam should be revised as $74\% \times 61\% = 45\%$, which is close to the experimentally measured total power throughput.

The insufficient power of the residual 1580-nm beam for THG imaging is a limitation of the current multimodal MPM endoscopy. Since the 1580-nm beam has a slightly larger beam size based on the above analysis of the frequency doubling process and the optical lens system of imaging, it suffers from higher power loss when passing through the imaging system. To improve the output power of the 1580-nm beam so that there will be sufficient residual power for 3PM imaging, several approaches can be taken. A larger MEMS mirror can be used to reduce the power loss with the trade-off of lower scanning speed. Alternatively, a smaller beam size can be designed to reduce the power loss, which also has a trade-off of smaller FOV. Those two approaches both have pros and cons. The MEMS scanner and the miniature optics inside the MPM imaging head will need further improvements in the future. Furthermore, the power of the 1580-nm pulse from the fiber laser could be increased by increasing the pump power of the diode pump lasers in the laser amplifier. Due to fiber nonlinearity, the spectrum and pulsewidth of the laser output could change and should be optimized again under the increased pump power condition. Through those

approaches, both the 790-nm beam and residual 1580-nm beam after the frequency-doubling unit will provide sufficient power to excite 2PM and 3PM imaging in biological tissue simultaneously.

4.2.3 Performance characterization

To characterize the performance of the miniature multiphoton endoscopy system with dual-wavelength excitation, the signal dependence on the input power, resolution, and focal shift are investigated. Figures 4.5(a)-4.5(c) show the TPEF, SHG, and THG images, respectively, of a silicon nano-chip which contains different nano-structures. The pseudocolor used is red for TPEF, green for SHG, and blue for THG. The merged image of the TPEF, SHG, and THG images is shown in Fig. 4.5(d), which shows good co-registration of the three contrasts.

The silicon nano-chip has a three-layer structure: the bottom is a 2-μm-thick buried oxide layer which is the SiO_2 underneath, the middle layer is a 220-nm-thick silicon wafer in which different nano-structures are fabricated by electron beam lithography, and the top is a 2.35-μm-thick SiO_2 cladding. The TPEF, SHG, and THG signals all come from the silicon wafer layer whose layout is shown in Fig. 4.5(e). Here bulk silicon forms the nano-wires and the nano-receivers labeled as part A, part B includes nano-gratings (spacing is around 100 nm), and part C is photonic crystal structure which contains dots array (diameter is around 180~250 nm). The zoom-in layouts of part A, B, and C are shown in Figs. 4.5(f)-4.5(h). Silicon has been reported to generate TPEF signal [105]. Thus, the nano-wires and part A, B, and C all show TPEF signal in Fig. 4.5(a). The SHG and THG contrasts in Figs. 4.5(b) and 4.5(c) are likely due to surface effect from the silicon wafer.

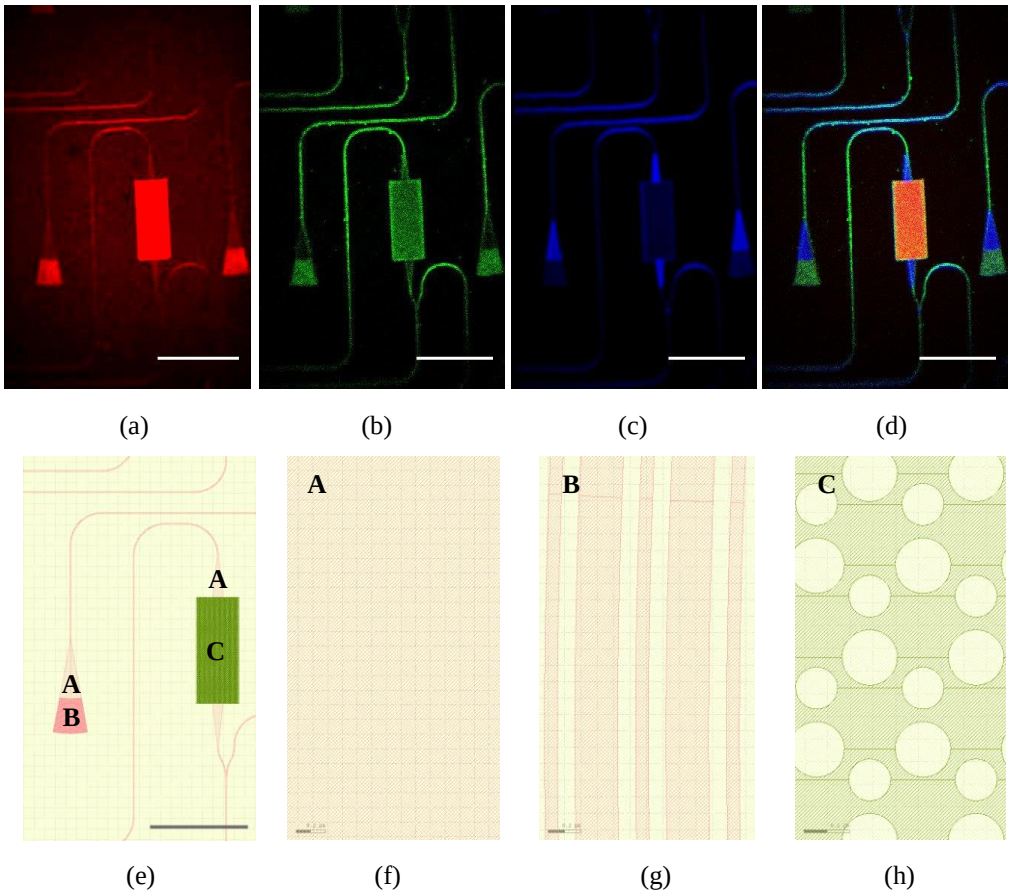

Figure 4.5 (a-d) Multimodal MPM imaging of a silicon nano-chip. (a) TPEF image. (b) SHG image. (c) THG image. (d) Merged image. Pseudocolor: TPEF in red, SHG in green, THG in blue. Scale bar is 50 μm. (e) Overall layout of the silicon nano-chip with scale bar of 50 μm. (f-h) Zoom-in layout of part A, B, and C in (e). Scale bar is 0.2 μm.

Figure 4.6 shows the TPEF, SHG, and THG signal intensity, respectively, versus the excitation power on the silicon nano-chip. The signal intensity is calculated by averaging over the pixels which have an intensity value higher than 10% of the maximum intensity. Two linear fitting lines with slope of 2 and 3, respectively, are also shown. As we can see, the TPEF and SHG signals show a quadratic dependence on the excitation power, and the THG signal shows a cubic dependence on the excitation power. This confirms that the detected TPEF and SHG are two-photon effects, and the detected THG is a three-photon effect.

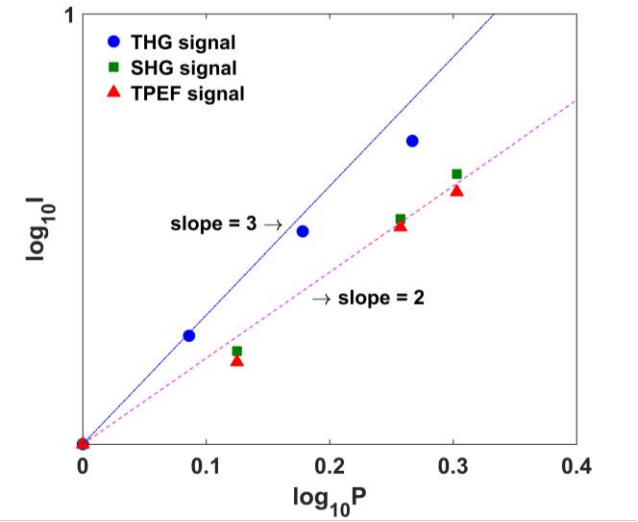

Figure 4.6 The intensity of the emitted signal versus the excitation power for TPEF (triangle), SHG (square), and THG (circle).

The width and depth of the nano-waveguide are about 500 nm and 220 nm, respectively, on the silicon nano-chip. The lateral resolution of the multimodal MPM endoscopy can be determined by measuring the lateral point spread function using the nano-waveguide. Figure 4.7 shows the TPEF, SHG, and THG intensity profile with Gaussian fitting across the nano-waveguide. The full-width-half-maximum (FWHM) of the Gaussian fit is found to be 1.1 μm, 1.0 μm, and 2.0 μm, for TPEF, SHG, and THG, respectively. Since the actual width of the nano-waveguide is much smaller than the measured values, those values could be regarded as the lateral resolution. The diffraction-limited resolution can be estimated by Rayleigh criterion as $0.61\frac{\lambda}{\mathrm{NA}}$ (λ is wavelength and NA is numerical aperture of the objective). The theoretically calculated resolution is 0.96 μm for 2PM and 1.93 μm for 3PM. The experimentally measured resolution matches well with the diffraction-limited resolution defined by Rayleigh criterion.

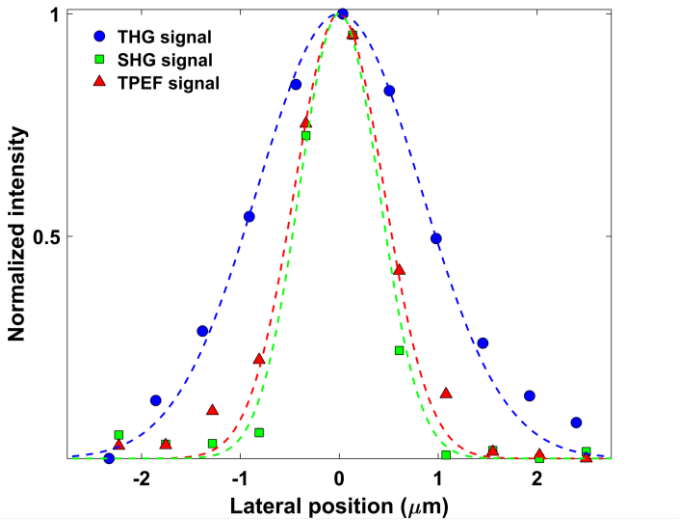

Figure 4.7 Intensity profile of TPEF (triangle), SHG (square), and THG (circle) measured across a nano-waveguide. The dash lines are the corresponding Gaussian fitting.

A challenging issue of dual-wavelength excitation in multimodal MPM is chromatic aberration or focal shift between the two excitation wavelengths [100]. Numerical simulation of the focal shift is carried out using Zemax and the result is shown in Fig. 4.8. The optical setup is shown in Fig. 4.8(a), which includes the scan lens, tube lens, and objective. The focal shift versus the excitation wavelength is plotted as the solid line in Fig. 4.8(b), where the design wavelength and zero focal shift position is at 790 nm. A focal shift of 39 μm is found between 790-nm and 1580-nm wavelength. The chromatic dispersion induced focal shift mainly comes from the objective lens and it could be compensated by designing custom achromatic objective lens with multiple lens elements. The focal shift between 790-nm and 1580-nm wavelength is also measured experimentally by imaging a thin sample plane such as the silicon nano-chip. By shifting the axial position of the sample using a linear stage (423, Newport) and micrometer (SM-13, Newport), the two imaging planes for the 790-nm and 1580-nm excitation can be overlapped. The experimental focal shift between 790-nm and 1580-nm wavelengths is measured to be ~30 μm, which is close

to the simulated focal shift. In the current experiment, the sample is manually shifted by 30 μm to match the imaging planes for the 2PM and 3PM, respectively. To address the issue of focal shift caused by two different wavelengths, A. Filippi *et al*. designed separate optical paths for adjusting the beam divergence respectively so that the focal planes were overlapped [100]. The drawback of this approach is the increased complexity and dimension of the setup, which is critical for endoscopy.

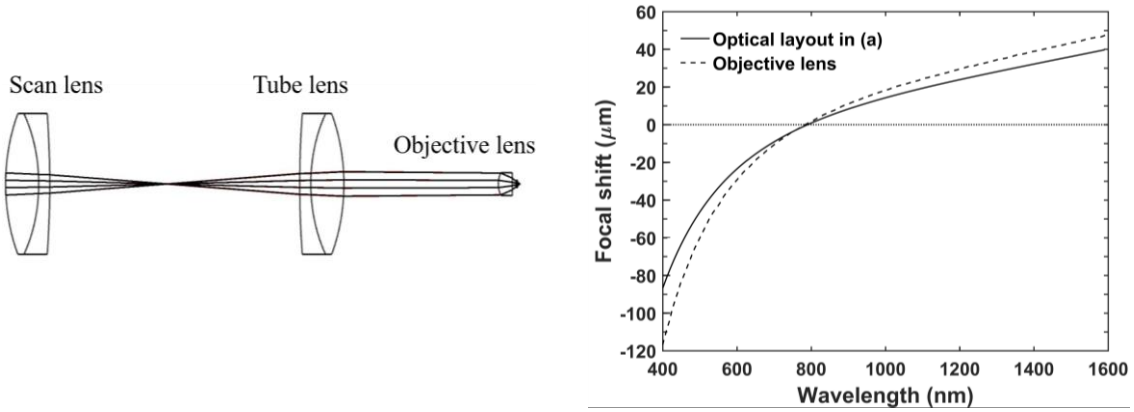

(a) (b)

Figure 4.8 Zemax simulation of focal shift. (a) Optical layout of the scan lens, tube lens, and objective lens. (b) The simulated focal shift versus wavelength. Solid line is for the three-lens system shown in (a) and the dashed line is for the objective lens alone. The zero focal shift is at 790 nm which is the design wavelength.

To overlap the focal plane for both the 790 nm and 1580 nm wavelengths, the focal shift needs to be minimized by a custom-designed, multi-element apochromatic objective lens which can specifically compensate the chromatic aberration between the 790 nm and 1580 nm wavelengths. A different strategy is to acquire 2PM and 3PM from two slightly shifted focal planes. 3D image stacks could be acquired by adding depth scanning in the endoscope, where the offset between the image stack acquired by 2PM and that acquired by 3PM could be aligned through post processing. When focusing the wavelengths to two separate planes, the laser energy

deposited into the focal volumes are also spatially separately. Therefore, laser-induced tissue damage in each focal volume can be considered separately and each wavelength could be operated to its maximum power below laser safety level to obtain high signal-to-noise ratio (SNR).

Currently the 2PM and 3PM images are acquired sequentially. The two excitation wavelengths are selected sequentially by two bandpass filters respectively. To achieve simultaneous 2PM and 3PM imaging, both the 1580-nm beam and 790-nm beam will be shined on tissue simultaneously. The TPEF, SHG, and THG signals can be separated into multiple detection channels based on their wavelength by using dichroic mirrors and bandpass filters on the detection side. For example, four detection channels can be designed, including 395±10 nm for SHG, 405-517 nm for TPEF, 527±10 nm for THG, and 537-650 nm for TPEF. The THG signal will be detected in the 527±10 nm channel but not in the 405-517 nm or the 537-650 nm channel.

Due to their different wavelengths, there is also a focal shift between the excitation and the emission wavelengths. From Fig. 4.8(b), the focal shift of the objective lens (shown as the dashed line) between 400-nm and 790-nm wavelength is found to be 114 μm. The effect of this focal shift on the collection efficiency is analyzed. Figure 4.9 shows the collection path which includes the objective lens, tube lens, collection lens, and MMF. The lens system can be analyzed according to the thin lens equation

$$\frac{1}{d_o}+\frac{1}{d_i}=\frac{1}{f} \tag{4.7}$$

where d_o is objective distance, d_i is image distance, and f is focal length. Magnification can be calculated as $M=-\frac{d_i}{d_o}$. The magnification from each lens can be calculated respectively and the total magnification can be obtained as $M=M_1M_2M_3$. When consider the 114 μm focal shift, the

total magnification is obtained as $M \approx 2.0$. For the FOV of 160 μm × 250 μm at the focal plane of the objective lens, after magnifying through the lens system, it is magnified to an area of 320 μm × 500 μm at the focus of the collection lens. In comparison, the magnified area is 285 μm × 445 μm when no focal shift is considered. Thus, the effect from the focal shift is not significant. Those areas are smaller than the cross-section of the 1500-μm-diameter collection fiber. Furthermore, the NA of the collection lens is 0.28. which is smaller than the NA of the MMF which is 0.39. Thus, all the MPM signals should be collected efficiently.

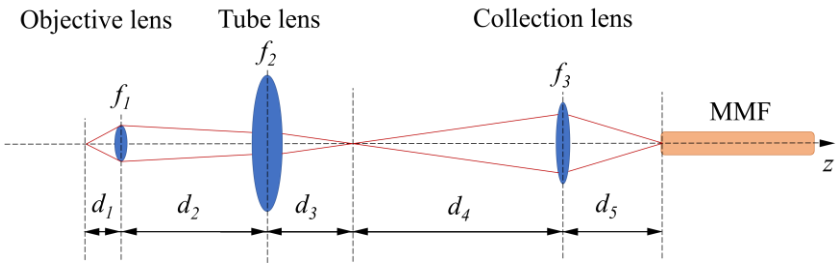

Figure 4.9 Optical layout of the collection path which includes the objective lens, tube lens, collection lens, and collection fiber. MMF: multimode fiber.

Table 4.3 summaries the system performance for the 2PM and 3PM. The resolution of the 3PM is two times worse than that of the 2PM due to the longer wavelength used in 3PM. The experimentally measured resolution matches well with the diffraction-limited resolution defined by Rayleigh criterion. In literature, Rayleigh criterion has been used to estimate the resolution of MPM [18, 106, 107]. In several other publications, it is mentioned that the 2PM resolution could be $1/\sqrt{2}$ times better and the 3PM resolution could be $1/\sqrt{3}$ times better than the one-photon resolution [30, 31]. This is not observed in our experiment. Since our objective lens is a single piece aspherical lens with no aberration compensation, the current resolution is likely not reaching the theoretical diffraction limit predicted for 2PM and 3PM.

Table 4.3 Comparison of the specifications of the 2PM and 3PM.

		2PM (Ex: 790 nm)	**3PM (Ex: 1580 nm)**
Lateral resolution (μm)	Theoretical	0.96	1.93
	Measured	1.1 (TPEF), 1.0 (SHG)	2.0
Focal shift (μm)	Theoretical	39	
	Measured	30	

4.3 Multimodal MPM imaging

The capability of the multimodal MPM endoscopy is evaluated by *ex vivo* imaging of tissue samples. It is applied to image multiple unprocessed (unstained and unfixed) biological samples. For 2PM imaging, the optical power on sample is 40 mW from 790 nm wavelength. For 3PM imaging, optical power of about 60 mW on sample is needed from the 1580 nm wavelength. Due to clipping of the 1580 nm beam by the MEMS scanner, the current setup only provides ~30 mW at the sample location. To prove the principle of multimodal MPM endoscopy, the 3PM images are acquired when the 1580 nm laser output from the fiber laser bypasses the PPLN. The 2PM and 3PM imaging are acquired at the frame rate of 0.4 frames/s with the pixel dwell time of 10 μs/pixel. Murine skin and femur bone, and rabbit femur bone samples are collected within 1 hour following euthanasia and images are taken within 2 hours following euthanasia.

Figures 4.10(a)-4.10(c) show the TPEF, SHG, and THG images, respectively, of the mouse skin. The merged image which combines all the three contrasts is shown in Fig. 4.10(d). In the skin image, the TPEF image shows the structure of elastin fibers, the SHG image shows strong signal from collagen fibers, and the THG image shows the adipocytes (fatty cells). The merged

image shows the correlation and interaction among the elastin fiber, collagen fiber, and fatty cells. As the three contrast signals capture different tissue components, more comprehensive information about the skin tissue can be acquired by the multimodal endoscopy.

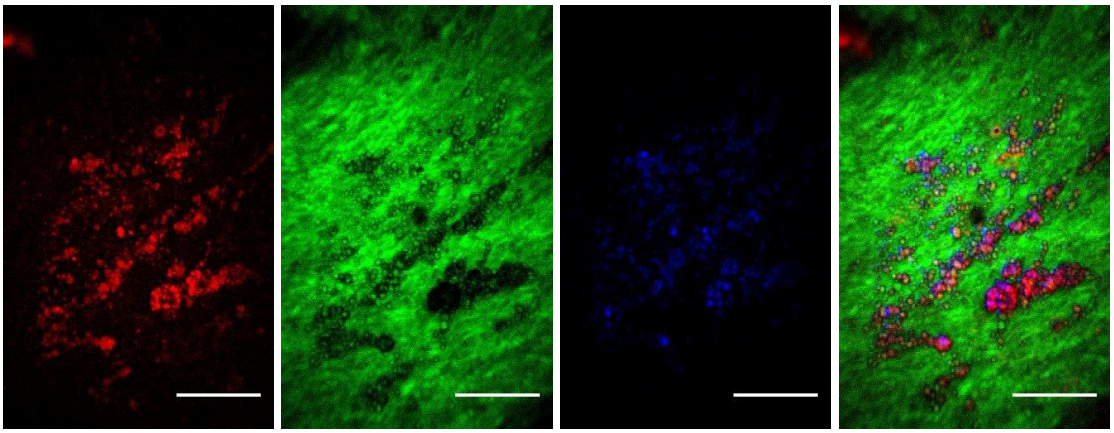

(a) (b) (c) (d)

Figure 4.10 Multimodal MPM imaging of murine skin. (a) TPEF image. (b) SHG image. (c) THG image. (d) Merged image. Pseudocolor: TPEF in red, SHG in green, THG in blue. Scale bar is 50 μm.

Figures 4.11(a)-4.11(c) show the TPEF, SHG, and THG images, respectively, of the inner surface in the mid-diaphysis of a murine femur bone. The merged image of the three different contrasts is shown in Fig. 4.11(d). In the bone sample, the TPEF image represents endogenous fluorophores and/or collagen cross-links [108], the SHG image shows lamellae collagen fibril bundles [96], and the THG image shows the interfaces in the lacuno-canalicular framework [96, 109]. The TPEF and SHG images show similar structures, which was also found in Reference [110]. When the TPEF, SHG, and THG images are merged, the Volkmann's canals can be more easily identified. The small-dotted pattern which surrounds the Volkmann's canals should be the lacuno-canalicular network [96]. Thus, the TPEF, SHG, and THG images provide complementary information on the porosity and tissue organization in the mouse femur bone.

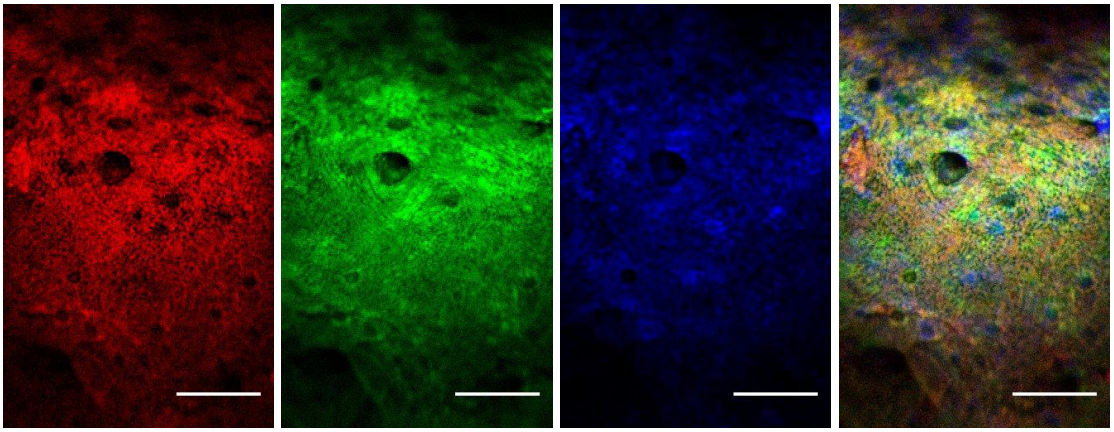

(a) (b) (c) (d)

Figure 4.11 Multimodal MPM imaging of the inner surface of a murine femur bone. (a) TPEF image. (b) SHG image. (c) THG image. (d) Merged image. Pseudocolor: TPEF in red, SHG in green, THG in blue. Scale bar is 50 μm.

Figures 4.12(a)-4.12(c) show the TPEF, SHG, and THG images, respectively, of the cross section in the mid-diaphysis of a rabbit femur bone. The merged image of the three different contrasts is shown in Fig. 4.12(d). In the bone sample, TPEF comes from endogenous fluorophores and/or collagen cross-links [108], SHG comes from lamellae collagen fibril bundles [96], and THG comes from the interfaces in the lacuno-canalicular framework [96, 109]. In the images, a Haversian canal is clearly visualized. Inside the Haversian canal, there should be blood vessels and nerve fibers. Bright contrast in the TPEF and THG channels are observed from inside the Haversian canal which could come from the blood vessels and nerve fibers.

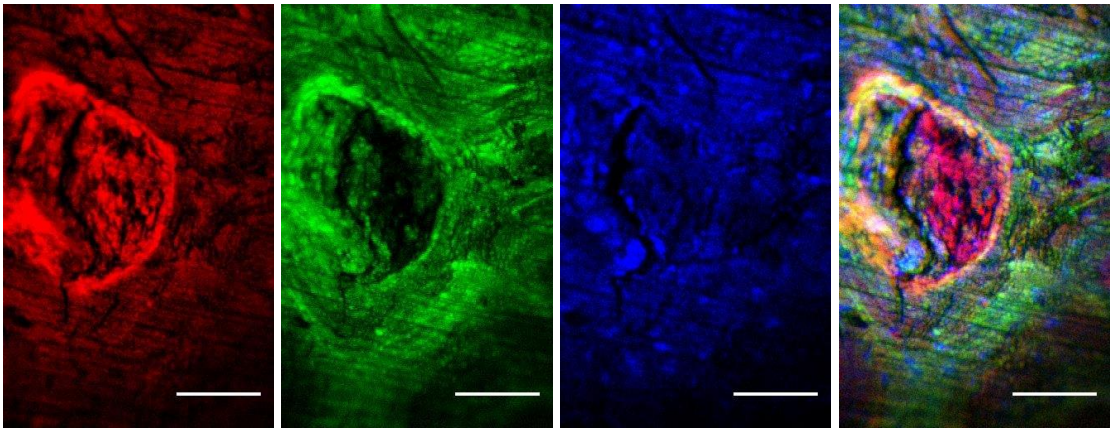

(a) (b) (c) (d)

Figure 4.12 Multimodal MPM imaging of the cross section of rabbit femur bone. (a) TPEF image. (b) SHG image. (c) THG image. (d) Merged image. Pseudocolor: TPEF in red, SHG in green, THG in blue. Scale bar is 50 μm.

4.4 Conclusions

A miniature multimodal MPM endoscopy based on dual-wavelength Er-doped fiber laser is presented. The dual-wavelength includes the fundamental pulse from the fiber laser at 1580 nm and the frequency-doubled pulse at 790 nm. The 1580 nm pulse is used to excite THG, and the 790 nm pulse is used to excite intrinsic TPEF and SHG. The laser pulse is directly coupled via a SMF to the MPM endoscopy imaging head where the 1580-nm pulse is frequency-doubled to 790-nm pulse, making the entire system highly compact and portable. Compared to other dual-wavelength laser systems used in multimodal MPMs, our design simplifies the dual-wavelength laser system and achieves fiber delivery of laser pulses. Label-free imaging by TPEF, SHG, and THG are demonstrated on biological tissues, such as skin and bone. Complementary information is obtained from intrinsic tissue fluorophores, elastin fibers, collagen fibers, lipids and interfaces. The multimodal MPM endoscopy is shown to be a powerful tool for imaging biological tissue. Its

miniature and compact design can further enable the translation of the technique into clinical applications.

Chapter 5: Summary and future work

5.1 Summary

MPM is an emerging technique that can perform histology-like high-resolution imaging of cells and tissues label-free. Traditional MPM systems have been benchtop microscopes using free-space optics. Benchtop systems are not suitable for clinical applications due to their bulky size and non-flexible free-space optical design. Translation of MPM to clinical applications has been slow due to several challenges, which include optimizing a compact laser source for efficient MPM excitation, managing femtosecond pulse delivery through optical fiber, and designing a miniature scanning probe. We have been making advancements for translating MPM into clinical applications.

First, we proposed a novel fiber-optic MPM endoscopy system design based on a frequency-doubled femtosecond Er-doped fiber laser. An Er-doped fiber laser operating at 1580 nm was delivered to the miniature imaging probe where the pulse was frequency-doubled into 790 nm through a PPLN. The 790 nm wavelength can excite intrinsic TPEF and SHG signals and no staining of tissue is required, which is critical for *in vivo* patient imaging. Frequency-doubling was achieved inside the distal end of the imaging head, and thus the fiber laser was directly connected with the imaging probe via a SMF and no fiber re-coupling was needed. By delivering the femtosecond pulse at 1580 nm, traditional SMF which has anomalous dispersion at this wavelength can be used to compensate the normal dispersion from EDF. Using this approach, an all-fiber based dispersion control was achieved by adjusting the length of EDF and SMF, and a compressed pulse was obtained at the output of the SMF. A MEMS scanner, miniature objective, and multimode collection fiber were used to make the probe compact. *Ex vivo* multiphoton imaging

of mammalian skin showed the capability of the system in imaging biological tissues. Our design not only reduced the cost of the system significantly, but also enabled all-fiber connection and dispersion management, which made the system much more portable.

Second, the fiber laser system and MPM endoscopy were optimized to increase the imaging speed which is critical for clinical applications. We optimized the frequency-doubled Er-doped fiber laser for reduced pulsewidth in order to increase the MPM excitation efficiency. MPM excitation efficiency depends quadratically on the laser power and inversely on the pulsewidth. We investigated the system optimization based on the pulsewidth and the laser power. For frequency-doubling with PPLN, a proper length of the PPLN needs to be selected. A shorter PPLN has a broader acceptance bandwidth and thus can provide a shorter pulsewidth. The MPM efficiency increases inversely with the pulsewidth when the power is the same. However, how the output power depends on the PPLN length is not that straightforward. In our study, we investigated how the average power of the frequency-doubled beam depended on the PPLN length. Under the assumptions that the bandwidth of the fundamental beam matched with the acceptance bandwidth of the PPLN and optimum focusing of the beam matched with the PPLN length, we found that the power of the frequency-doubled output was irrelevant to the PPLN length. This was analyzed theoretically and validated experimentally. Therefore, by considering both the pulsewidth and the power of the frequency-doubled Er-doped fiber laser, we concluded that the MPM efficiency grows inversely with the PPLN length. After selecting the proper PPLN length, the next step was to match the bandwidth of the Er-doped fiber laser pulse with the acceptance bandwidth of the selected PPLN. To manipulate the bandwidth of the Er-doped fiber laser, we optimized the pre-chirp fiber following the approach for pulse management in optical fiber where GVD and SPM

acted together. After the above systematic optimization, a fast MPM imaging speed at 4 frames/s was achieved.

Third, we demonstrated multimodal MPM imaging, including simultaneous two-photon microscopy and three-photon microscopy, using the frequency-doubled Er-doped fiber laser system. Dual excitation wavelengths at 1580 nm and 790 nm were obtained from the fundamental and frequency-doubled pulses of the laser system. The 1580-nm pulse was used to excite THG, and the 790-nm pulse was used to excite intrinsic TPEF and SHG. The label-free multimodal MPM imaging can acquire multiple contrasts simultaneously for obtaining comprehensive information about cells and tissues, which has great significance in clinical application. Using the miniature multiphoton endoscopy with dual-wavelength Er-doped fiber laser, label-free imaging on *ex vivo* biological samples were carried out, which demonstrated the multiple imaging contrasts obtained from different tissue constituents. Those results demonstrated the capability and potential of the multimodal MPM endoscopy for future clinical applications.

We have carried out thorough investigations on the development and implementation of femtosecond fiber laser to the MPM endoscopy. We have made contributions in the following aspects: (1) proposed a femtosecond fiber laser to replace the conventional Ti:Sapphire laser and developed a novel approach for femtosecond pulse delivery in the MPM endoscopy; (2) increased the imaging speed of the MPM endoscopy through the optimization of the Er-doped fiber laser system; (3) demonstrated simultaneous label-free two-photon and three-photon imaging by using the optimized MPM endoscopy.

There are several limitations of the current MPM endoscopy system. The imaging speed is limited to 4 frames/s, which will require further improvement for real-time imaging. The size of the MPM probe is still relatively large and a smaller packaging will be needed for imaging the oral

cavity. The resolution does not reach the theoretical estimation for 2PM and 3PM yet. The current imaging is only 2D, and 3D imaging with a depth scanning will be required for clinical applications.

5.2 Future work

Several future developments and investigations can be carried out to further improve the capability and applications of the MPM endoscopy towards *in vivo* imaging.

One limitation in our current MPM endoscopy is the imaging speed, which is critical for *in vivo* imaging to reduce motion artifacts. The current imaging speed is 4 frames/s. To further increase the imaging speed to real-time imaging, we will need to increase the mechanical scanning speed. Faster scanner and resonant scanning can be implemented to increase the imaging speed. The raster scanning speed can be increased at the cost of reduced MEMS mirror size or scanning angle, which could reduce the FOV. Additionally, resonance scanning mode which can scan much faster and provide a larger scanning angle than raster scanning can be applied to the MEMS to increase the speed. Different MEMS scanners and optimum operating conditions will be investigated for achieving high stability and repeatability. Image processing algorithms will be developed to compensate for any image distortion due to non-uniform scanning.

When the scanning speed is increased, the acquisition time per pixel drops and thus the collected MPM signal drops. Ultimately, the imaging speed will be limited by the MPM excitation efficiency which needs to be increased to match with the faster scanning speed. To increase the MPM excitation efficiency, a shorter pulsewidth is required. A shorter PPLN, for example 0.15 mm length, can potentially reduce the pulsewidth to sub-50 fs using the systematic approach

described in Chapter 3. For sub-50 fs pulses, compensating the dispersion slope is also critical, which can be achieved by using dispersion compensation fiber.

Other than pulsewidth, increasing the NA of the objective lens can also increase the MPM excitation efficiency and thus improve the imaging speed. MPM intensity is proportional to the fourth power of NA. The current objective lens is a single-element aspherical lens with NA = 0.5. The NA could be increased to 1.0 by using custom-designed, multiple-element lens with chromatic aberration and spherical aberration corrections. Thus, the MPM intensity is expected to be increased by 16 times, and the imaging speed could be largely increased to reach video rate at 24 frames/s. The real-time imaging will enable MPM endoscopy for *in vivo* imaging and clinical applications.

Depth scanning is also important in MPM endoscopy for clinical application. The current 2D MEMS scans only in XY plane. In the future, depth scanning in Z direction can be added to the MPM endoscopy by scanning the objective lens in Z direction. An electromagnetic actuator to move the objective lens in Z direction can be added in the imaging head. Additionally, a mechanical design of an attachable adapter will also be investigated and implemented at the end of the imaging head to fix its position onto skin, which can help to apply our MPM endoscopy and reduce motion artifacts during *in vivo* imaging.

Stability of the MPM endoscopy is critical when it is applied to clinical applications. During imaging, the delivery fiber which connects the fiber laser and the MPM endoscopy will be moved and bended. Currently, SMF is used, where the polarization state of the output pulse will change if the fiber is moved. This will reduce the MPM excitation power from the PPLN crystal. To maintain the polarization state, polarization-maintaining (PM) fiber could be used. In PM fiber, a built-in birefringence is made much larger than the random changes caused by stress and core-

shape variations. A PM fiber has two principal axes along which the fiber is capable of maintaining linear polarization state of the incident light. As the excitation light for MPM imaging is fs pulses, dispersion management is very critical to maintain short pulse delivery. Therefore, there are additional challenges in delivering fs pulses in PM fiber. Further investigations of controlling the dispersion in the PM delivery fiber will be needed.

With improved imaging speed and quality, the MPM endoscopy will be evaluated for *in vivo* patient imaging to detect oral cancer in the future.

Bibliography

1. W. Denk, J. H. Strickler, and W. W. Webb, "Two-photon laser scanning fluorescence microscopy". Science **248**, 73-76 (1990).
2. W. R. Zipfel, R. M. Williams, and W. W. Webb, "Nonlinear magic: multiphoton microscopy in the biosciences". Nature Biotechnology **21**, 1369-1377 (2003).
3. P. J. Campagnola and L. M. Loew, "Second-harmonic imaging microscopy for visualizing biomolecular arrays in cells, tissues and organisms". Nature Biotechnology **21**, 1356-1360 (2003).
4. A. Zoumi, A. Yeh, and B. J. Tromberg, "Imaging cells and extracellular matrix in vivo by using second-harmonic generation and two-photon excited fluorescence". Proceedings of the National Academy of Sciences **99**, 11014-11019 (2002).
5. P. J. Campagnola, M. Wei, A. Lewis, and L. M. Loew, "High-resolution nonlinear optical imaging of live cells by second harmonic generation". Biophysical Journal **77**, 3341 (1999).
6. M. Goppert-Mayer, "Elementary file with two quantum fissures". Annalen Der Physik **9**, 273-294 (1931).
7. P. A. Franken, A. E. Hill, C. W. Peters, and G. Weinreich, "Generation of optical harmonics". Physical Review Letters **7**, 118-119 (1961).
8. I. Freund, M. Deutsch, and A. Sprecher, "Connective tissue polarity. Optical second-harmonic microscopy, crossed-beam summation, and small-angle scattering in rat-tail tendon". Biophysical Journal **50**, 693-712 (1986).
9. T. G. Oertner, "Functional imaging of single synapses in brain slices". Experimental physiology **87**, 733-736 (2002).

10. T. Ladewig, P. Kloppenburg, P. M. Lalley, W. R. Zipfel, W. W. Webb, and B. U. Keller, "Spatial profiles of store-dependent calcium release in motoneurones of the nucleus hypoglossus from newborn mouse". The Journal of Physiology **547**, 775-787 (2003).

11. E. B. Brown, R. B. Campbell, Y. Tsuzuki, L. Xu, P. Carmeliet, D. Fukumura, and R. K. Jain, "In vivo measurement of gene expression, angiogenesis and physiological function in tumors using multiphoton laser scanning microscopy". Nature Medicine **7**, 864-868 (2001).

12. D. M. McDonald and P. L. Choyke, "Imaging of angiogenesis: from microscope to clinic". Nature Medicine **9**, 713-725 (2003).

13. J. C. Jung and M. J. Schnitzer, "Multiphoton endoscopy". Optics Letters **28**, 902-904 (2003).

14. M. T. Myaing, D. J. MacDonald, and X. Li, "Fiber-optic scanning two-photon fluorescence endoscope". Optics Letters **31**, 1076-1078 (2006).

15. C. J. Engelbrecht, R. S. Johnston, E. J. Seibel, and F. Helmchen, "Ultra-compact fiber-optic two-photon microscope for functional fluorescence imaging in vivo". Optics Express **16**, 5556-5564 (2008).

16. W. Jung, S. Tang, D. T. McCormic, T. Xie, Y. C. Ahn, J. Su, I. V. Tomov, T. B. Krasieva, B. J. Tromberg, and Z. Chen, "Miniaturized probe based on a microelectromechanical system mirror for multiphoton microscopy". Optics Letters **33**, 1324-1326 (2008).

17. L. Fu, A. Jain, H. Xie, C. Cranfield, and M. Gu, "Nonlinear optical endoscopy based on a double-clad photonic crystal fiber and a MEMS mirror". Optics Express **14**, 1027-1032 (2006).

18. S. Tang, W. Jung, D. McCormick, T. Xie, J. Su, Y. C. Ahn, B. J. Tromberg, and Z. Chen, "Design and implementation of fiber-based multiphoton endoscopy with

microelectromechanical systems scanning". Journal of Biomedical Optics **14**, 034005 (2009).

19. Y. R. Shen, *The Principles of Nonlinear Optics*. Wiley: New York (1984).

20. A. Diaspro, G. Chirico, and M. Collini, "Two-photon fluorescence excitation and related techniques in biological microscopy". Quarterly Reviews of Biophysics **38**, 97-166 (2005).

21. P. T. C. So, C. Y. Dong, B. R. Masters, and K. M. Berland, "Two-photon excitation fluorescence microscopy". Annual Review of Biomedical Engineering **2**, 399-429 (2000).

22. M. C. Skala, J. M. Squirrell, K. M. Vrotsos, J. C. Eickhoff, A. Gendron-Fitzpatrick, K. W. Eliceiri, and N. Ramanujam, "Multiphoton microscopy of endogenous fluorescence differentiates normal, precancerous, and cancerous squamous epithelial tissues". Cancer Research **65**, 1180-1186 (2005).

23. L. Shi, L. Lu, G. Harvey, T. Harvey, A. Rodríguez-Contreras, and R. R. Alfano, "Label-free fluorescence spectroscopy for detecting key biomolecules in brain tissue from a mouse model of Alzheimer's disease". Scientific Reports **7**, 2599 (2017).

24. W. R. Zipfel, R. M. Williams, R. Christie, A. Y. Nikitin, B. T. Hyman, and W. W. Webb, "Live tissue intrinsic emission microscopy using multiphoton-excited native fluorescence and second harmonic generation". Proceedings of the National Academy of Sciences **100**, 7075-7080 (2003).

25. Y. Barad, H. Eisenberg, M. Horowitz, and Y. Silberberg, "Nonlinear scanning laser microscopy by third harmonic generation". Applied Physics Letters **70**, 922-924 (1997).

26. N. Olivier, M. A. Luengo-Oroz, L. Duloquin, E. Faure, T. Savy, I. Veilleux, X. Solinas, D. Débarre, P. Bourgine, and A. Santos, "Cell lineage reconstruction of early zebrafish embryos using label-free nonlinear microscopy". Science **329**, 967-971 (2010).

27. F. Helmchen and W. Denk, "Deep tissue two-photon microscopy". Nature Methods **2**, 932-940 (2005).

28. A. M. D. Lee, H. Wang, Y. Yu, S. Tang, J. Zhao, H. Lui, D. I. McLean, and H. Zeng, "In vivo video rate multiphoton microscopy imaging of human skin". Optics Letters **36**, 2865-2867 (2011).

29. G. McConnell, W. Amos, and T. Wilson, *Confocal microscopy*. Elsevier (2011).

30. J. H. Yu, S.-H. Kwon, Z. Petrášek, O. K. Park, S. W. Jun, K. Shin, M. Choi, Y. I. Park, K. Park, ,H. B. Na, N. Lee, D. W. Lee, J. H. Kim, P. Schwille, and T. Hyeon, "High-resolution three-photon biomedical imaging using doped ZnS nanocrystals". Nature Materials **12**, 359-366 (2013).

31. S. Dietzel, J. Pircher, A. K. Nekolla, M. Gull, A. W. Brändli, U. Pohl, and M. Rehberg, "Label-free determination of hemodynamic parameters in the microcirculaton with third harmonic generation microscopy". PloS One **9**, e99615 (2014).

32. Y. Zhang, M. L. Akins, K. Murari, J. Xi, M.-J. Li, K. Luby-Phelps, M. Mahendroo, and X. Li, "A compact fiber-optic SHG scanning endomicroscope and its application to visualize cervical remodeling during pregnancy". Proceedings of the National Academy of Sciences **109**, 12878-12883 (2012).

33. D. R. Rivera, C. M. Brown, D. G. Ouzounov, I. Pavlova, D. Kobat, W. W. Webb, and C. Xu, "Compact and flexible raster scanning multiphoton endoscope capable of imaging unstained tissue". Proceedings of the National Academy of Sciences **108**, 17598-17603 (2011).

34. W. Piyawattanametha, E. D. Cocker, L. D. Burns, R. P. Barretto, J. C. Jung, H. Ra, O. Solgaard, and M. J. Schnitzer, "In vivo brain imaging using a portable 2.9 g two-photon

microscope based on a microelectromechanical systems scanning mirror". Optics Letters **34**, 2309-2311 (2009).

35. R. Le Harzic, I. Riemann, M. Weinigel, K. König, and B. Messerschmidt, "Rigid and high-numerical-aperture two-photon fluorescence endoscope". Applied Optics **48**, 3396-3400 (2009).

36. Y. Zhao, H. Nakamura, and R. J. Gordon, "Development of a versatile two-photon endoscope for biological imaging". Biomedical Optics Express **1**, 1159-1172 (2010).

37. G. Ducourthial, P. Leclerc, T. Mansuryan, M. Fabert, J. Brevier, R. Habert, F. Braud, R. Batrin, C. Vever-Bizet, and G. Bourg-Heckly, "Development of a real-time flexible multiphoton microendoscope for label-free imaging in a live animal". Scientific Reports **5**, 18303 (2015).

38. W. Liang, G. Hall, B. Messerschmidt, M.-J. Li, and X. Li, "Nonlinear optical endomicroscopy for label-free functional histology in vivo". Light: Science & Applications **6**, e17082 (2017).

39. F. Helmchen, M. S. Fee, D. W. Tank, and W. Denk, "A miniature head-mounted two-photon microscope: high-resolution brain imaging in freely moving animals". Neuron **31**, 903-912 (2001).

40. Y. Wu, Y. Leng, J. Xi, and X. Li, "Scanning all-fiber-optic endomicroscopy system for 3D nonlinear optical imaging of biological tissues". Optics Express **17**, 7907-7915 (2009).

41. D. M. Huland, C. M. Brown, S. S. Howard, D. G. Ouzounov, I. Pavlova, K. Wang, D. R. Rivera, W. W. Webb, and C. Xu, "In vivo imaging of unstained tissues using long gradient index lens multiphoton endoscopic systems". Biomedical Optics Express **3**, 1077-1085 (2012).

42. S. Tang, T. B. Krasieva, Z. Chen, G. Tempea, and B. J. Tromberg, "Effect of pulse duration on two-photon excited fluorescence and second harmonic generation in nonlinear optical microscopy". Journal of Biomedical Optics **11**, 020501 (2006).

43. L. E. Nelson, D. J. Jones, K. Tamura, H. A. Haus, and E. P. Ippen, "Ultrashort-pulse fiber ring lasers". Applied Physics B **65**, 277-294 (1997).

44. S. Tang, J. Liu, T. B. Krasieva, Z. Chen, and B. J. Tromberg, "Developing compact multiphoton systems using femtosecond fiber lasers". Journal of Biomedical Optics **14**, 030508 (2009).

45. G. Liu, K. Kieu, F. W. Wise, and Z. Chen, "Multiphoton microscopy system with a compact fiber-based femtosecond-pulse laser and handheld probe". Journal of Biophotonics **4**, 34-39 (2011).

46. A. Krolopp, A. Csákányi, D. Haluszka, D. Csáti, L. Vass, A. Kolonics, N. Wikonkál, and R. Szipőcs, "Handheld nonlinear microscope system comprising a 2 MHz repetition rate, mode-locked Yb-fiber laser for in vivo biomedical imaging". Biomedical Optics Express **7**, 3531-3542 (2016).

47. K. Murari, Y. Zhang, S. Li, Y. Chen, M.-J. Li, and X. Li, "Compensation-free, all-fiber-optic, two-photon endomicroscopy at 1.55 μm". Optics Letters **36**, 1299-1301 (2011).

48. G. P. Agrawal, *Nonlinear Fiber Optics*. Elsevier Science: New York (2010).

49. A. M. Weiner, *Ultrafast Optics*. Wiley (2009).

50. S. R. Kantelhardt, D. Kalasauskas, K. König, E. Kim, M. Weinigel, A. Uchugonova, and A. Giese, "In vivo multiphoton tomography and fluorescence lifetime imaging of human brain tumor tissue". Journal of Neuro-oncology **127**, 473-482 (2016).

51. C. L. Hoy, N. J. Durr, P. Chen, W. Piyawattanametha, H. Ra, O. Solgaard, and A. Ben-Yakar, "Miniaturized probe for femtosecond laser microsurgery and two-photon imaging". Optics Express **16**, 9996-10005 (2008).

52. C. F. Poh, J. S. Durham, P. M. Brasher, D. W. Anderson, K. W. Berean, C. E. MacAulay, J. J. Lee, and M. P. Rosin, "Canadian Optically-guided approach for Oral Lesions Surgical (COOLS) trial: study protocol for a randomized controlled trial". BMC Cancer **11**, 462 (2011).

53. C. F. Poh, C. E. MacAulay, D. M. Laronde, P. Michele Williams, L. Zhang, and M. P. Rosin, "Squamous cell carcinoma and precursor lesions: diagnosis and screening in a technical era". Periodontology 2000 **57**, 73-88 (2011).

54. C. F. Poh, S. P. Ng, P. M. Williams, L. Zhang, D. M. Laronde, P. Lane, C. MacAulay, and M. P. Rosin, "Direct fluorescence visualization of clinically occult high-risk oral premalignant disease using a simple hand-held device". Head & Neck: Journal for the Sciences and Specialties of the Head and Neck **29**, 71-76 (2007).

55. P. M. Lane, T. Gilhuly, P. D. Whitehead, H. Zeng, C. Poh, S. Ng, M. Williams, L. Zhang, M. Rosin, and C. E. MacAulay, "Simple device for the direct visualization of oral-cavity tissue fluorescence". Journal of Biomedical Optics **11**, 024006 (2006).

56. D. Shin, N. Vigneswaran, A. Gillenwater, and R. Richards-Kortum, "Advances in fluorescence imaging techniques to detect oral cancer and its precursors". Future Oncology **6**, 1143-1154 (2010).

57. W. M. White, M. Rajadhyaksha, S. González, R. L. Fabian, and R. R. Anderson, "Noninvasive imaging of human oral mucosa in vivo by confocal reflectance microscopy". Laryngoscope **109**, 1709-1717 (1999).

58. K. C. Maitland, A. M. Gillenwater, M. D. Williams, A. K. El-Naggar, M. R. Descour, and R. R. Richards-Kortum, "In vivo imaging of oral neoplasia using a miniaturized fiber optic confocal reflectance microscope". Oral Oncology **44**, 1059-1066 (2008).

59. P. S.-P. Thong, M. C. Olivo, K.-W. Kho, K. Mancer, W. Zheng, M. R. Harris, and K. C. Soo, "Laser confocal endomicroscopy as a novel technique for fluorescence diagnostic imaging of the oral cavity". Journal of Biomedical Optics **12**, 014007 (2007).

60. S. E. Hallani, C. F. Poh, C. Macaulay, M. Follen, M. Guillaud, and P. M. Lane, "Ex vivo confocal imaging with contrast agents for the detection of oral potentially malignant lesions". Oral Oncology **49**, 582-590 (2013).

61. M. C. Skala, K. M. Riching, A. Gendron-Fitzpatrick, J. Eickhoff, K. W. Eliceiri, J. G. White, and N. Ramanujam, "In vivo multiphoton microscopy of NADH and FAD redox states, fluorescence lifetimes, and cellular morphology in precancerous epithelia". Proceedings of the National Academy of Sciences **104**, 19494-19499 (2007).

62. S. K. Teh, W. Zheng, S. Li, D. Li, Y. Zeng, Y. Yang, and J. Y. Qu, "Multimodal nonlinear optical microscopy improves the accuracy of early diagnosis of squamous intraepithelial neoplasia". Journal of Biomedical Optics **18**, 036001 (2013).

63. S. Tang, Y. Zhou, K. K. H. Chan, and T. Lai, "Multiscale multimodal imaging with multiphoton microscopy and optical coherence tomography". Optics Letters **36**, 4800-4802 (2011).

64. A. N. S. Institute, *American national standard for safe use of lasers*. Laser Institute of America (2007).

65. R. W. Waynant, *Lasers in medicine*. CRC press (2001).

66. A. Vogel, J. Noack, G. Hüttman, and G. Paltauf, "Mechanisms of femtosecond laser nanosurgery of cells and tissues". Applied Physics B **81**, 1015-1047 (2005).

67. S. L. Jacques, "Optical properties of biological tissues: a review". Physics in Medicine and Biology **58**, R37-61 (2013).

68. D. H. Sliney and J. Mellerio, *Safety with lasers and other optical sources: a comprehensive handbook*. Springer US (2013).

69. B. A. Flusberg, J. C. Jung, E. D. Cocker, E. P. Anderson, and M. J. Schnitzer, "In vivo brain imaging using a portable 3.9 gram two-photon fluorescence microendoscope". Optics Letters **30**, 2272-2274 (2005).

70. F. Helmchen, W. Denk, and J. N. D. Kerr, "Miniaturization of two-photon microscopy for imaging in freely moving animals". Cold Spring Harbor Protocols 2013 **10**, 904-913 (2013).

71. W. Göbel, A. Nimmerjahn, and F. Helmchen, "Distortion-free delivery of nanojoule femtosecond pulses from a Ti:sapphire laser through a hollow-core photonic crystal fiber". Optics Letters **29**, 1285-1287 (2004).

72. J. Yu, H. Zeng, H. Lui, J. S. Skibina, G. Steinmeyer, and S. Tang, "Characterization and application of chirped photonic crystal fiber in multiphoton imaging". Optics Express **22**, 10366-10379 (2014).

73. J. R. Unruh, E. S. Price, R. G. Molla, L. Stehno-Bittel, C. K. Johnson, and R. Hui, "Two-photon microscopy with wavelength switchable fiber laser excitation". Optics Express **14**, 9825-9831 (2006).

74. W. Chun, D. Do, and D.-G. Gweon, "Design and demonstration of multimodal optical scanning microscopy for confocal and two-photon imaging". Review of Scientific Instruments **84**, 013701 (2013).

75. D. M. Huland, M. Jain, D. G. Ouzounov, B. D. Robinson, D. S. Harya, M. M. Shevchuk, P. Singhal, C. Xu, and A. K. Tewari, "Multiphoton gradient index endoscopy for evaluation of diseased human prostatic tissue ex vivo". Journal of Biomedical Optics **19**, 116011 (2014).

76. M. Hofer, M. E. Fermann, F. Haberl, M. H. Ober, and A. J. Schmidt, "Mode locking with cross-phase and self-phase modulation". Optics Letters **16**, 502-504 (1991).

77. K. Tamura, L. E. Nelson, H. A. Haus, and E. P. Ippen, "Soliton versus nonsoliton operation of fiber ring lasers". Applied Physics Letters **64**, 149-151 (1994).

78. L. E. Myers, R. C. Eckardt, M. M. Fejer, R. L. Byer, W. R. Bosenberg, and J. W. Pierce, "Quasi-phase-matched optical parametric oscillators in bulk periodically poled LiNbO3". Journal of the Optical Society of America B **12**, 2102-2116 (1995).

79. G. D. Boyd and D. A. Kleinman, "Parametric Interaction of Focused Gaussian Light Beams". Journal of Applied Physics **39**, 3597-3639 (1968).

80. K. Moutzouris, F. Adler, F. Sotier, D. Träutlein, and A. Leitenstorfer, "Multimilliwatt ultrashort pulses continuously tunable in the visible from a compact fiber source". Optics Letters **31**, 1148-1150 (2006).

81. L. Gruner-Nielsen, M. Wandel, P. Kristensen, C. Jorgensen, L.V. Jorgensen, B. Edvold, B. Palsdottir, and D. Jakobsen, "Dispersion-compensating fibers". Journal of Lightwave Technology **23**, 3566-3579 (2005).

82. Y. Zhao, M. Sheng, L. Huang, and S. Tang, "Design of a fiber-optic multiphoton microscopy handheld probe". Biomedical Optics Express **7**, 3425-3437 (2016).

83. P. C. Cheng, B.-L. Lin, F.-J. Kao, C.-K. Sun, Y.-S. Wang, T.-M. Liu, Y. Wang, J. Chen, M.-K. Huang, and I. Johnson, "Multiphoton fluorescence spectroscopy of flourescent bioprobes and biomolecules". SPIE proc. (Photonics Taiwan 2000) **4082**, 87-91 (2000).

84. N. G. Horton, K. Wang, D. Kobat, C. G. Clark, F. W. Wise, C. B. Schaffer, and C. Xu, "In vivo three-photon microscopy of subcortical structures within an intact mouse brain". Nature Photonics **7**, 205-209 (2013).

85. L. Huang, A. K. Mills, Y. Zhao, D. J. Jones, and S. Tang, "Miniature fiber-optic multiphoton microscopy system using frequency-doubled femtosecond Er-doped fiber laser". Biomedical Optics Express **7**, 1948-1956 (2016).

86. C. Xu and W. W. Webb, "Measurement of two-photon excitation cross sections of molecular fluorophores with data from 690 to 1050 nm". Journal of The Optical Society of America B **13**, 481-491 (1996).

87. M. M. Fejer, G. A. Magel, D. H. Jundt, and R. L. Byer, "Quasi-phase-matched second harmonic generation: tuning and tolerances". IEEE Journal of Quantum Electronics **28**, 2631-2654 (1992).

88. F. Tauser, A. Leitenstorfer, and W. Zinth, "Amplified femtosecond pulses from an Er:fiber system: Nonlinear pulse shortening and selfreferencing detection of the carrier-envelope phase evolution". Optics Express **11**, 594-600 (2003).

89. M. E. Fermann, V. I. Kruglov, B. C. Thomsen, J. M. Dudley, and J. D. Harvey, "Self-similar propagation and amplification of parabolic pulses in optical fibers". Physical Review Letters **84**, 6010-6013 (2000).

90. J. W. Nicholson, A. D. Yablon, P. S. Westbrook, K. S. Feder, and M. F. Yan, "High power, single mode, all-fiber source of femtosecond pulses at 1550 nm and its use in supercontinuum generation". Optics Express **12**, 3025-3034 (2004).

91. M. J. Levene, D. A. Dombeck, K. A. Kasischke, R. P. Molloy, and W. W. Webb, "In vivo multiphoton microscopy of deep brain tissue". Journal of Neurophysiology **91**, 1908-1912 (2004).

92. S.-J. Lin, S.-H. Jee, C.-J. Kuo, R.-J. Wu, W.-C. Lin, J.-S. Chen, Y.-H. Liao, C.-J. Hsu, T.-F. Tsai, Y.-F. Chen, and C.-Y. Dong, "Discrimination of basal cell carcinoma from normal dermal stroma by quantitative multiphoton imaging". Optics Letters **31**, 2756-2758 (2006).

93. P. J. Campagnola, M. D. Wei, A. Lewis, and L. M. Loew, "High-resolution nonlinear optical imaging of live cells by second harmonic generation". Biophysical Journal **77**, 3341-3349 (1999).

94. C. Xu, W. Zipfel, J. B. Shear, R. M. Williams, and W. W. Webb, "Multiphoton fluorescence excitation: new spectral windows for biological nonlinear microscopy". Proceedings of the National Academy of Sciences **93**, 10763-10768 (1996).

95. B. Weigelin, G.-J. Bakker, and P. Friedl, "Intravital third harmonic generation microscopy of collective melanoma cell invasion: principles of interface guidance and microvesicle dynamics". IntraVital **1**, 32-43 (2012).

96. R. Genthial, E. Beaurepaire, M.-C. Schanne-Klein, F. Peyrin, D. Farlay, C. Olivier, Y. Bala, G. Boivin, J.-C. Vial, D. Débarre, and A. Gourrier, "Label-free imaging of bone multiscale porosity and interfaces using third-harmonic generation microscopy". Scientific Reports **7**, 3419 (2017).

97. K. Kieu, S. Mehravar, R. Gowda, R. A. Norwood, and N. Peyghambarian, "Label-free multi-photon imaging using a compact femtosecond fiber laser mode-locked by carbon nanotube saturable absorber". Biomedical Optics Express **4**, 2187-2195 (2013).

98. D. G. Ouzounov, T. Wang, M. Wang, D. D. Feng, N. G. Horton, J. C. Cruz-Hernández, Y.-T. Cheng, J. Reimer, A. S. Tolias, N. Nishimura, and C. Xu, "In vivo three-photon imaging of activity of GCaMP6-labeled neurons deep in intact mouse brain". Nature Methods **14**, 388-390 (2017).

99. D. Débarre, W. Supatto, A.-M. Pena, A. Fabre, T. Tordjmann, L. Combettes, M.-C. Schanne-Klein, and E. Beaurepaire, "Imaging lipid bodies in cells and tissues using third-harmonic generation microscopy". Nature Methods **3**, 47-53 (2006).

100. A. Filippi, E. Dal Sasso, L. Iop, A. Armani, M. Gintoli, M. Sandri, G. Gerosa, F. Romanato, and G. Borile, "Multimodal label-free ex vivo imaging using a dual-wavelength microscope with axial chromatic aberration compensation". Journal of Biomedical Optics **23**, 091403 (2018)

101. D. M. Small, J. S. Jones, I. I. Tendler, P. E. Miller, A. Ghetti, and N. Nishimura, "Label-free imaging of atherosclerotic plaques using third-harmonic generation microscopy". Biomedical Optics Express **9**, 214-229 (2018).

102. F. Akhoundi, Y. Qin, N. Peyghambarian, J. K. Barton, and K. Kieu, "Compact fiber-based multi-photon endoscope working at 1700 nm". Biomedical Optics Express **9**, 2326-2335 (2018).

103. W. Nagourney, *Quantum electronics for atomic physics and telecommunication*. Oxford University Press (2014).

104. B. E. A. Saleh, M. C. Teich, *Fundamentals of photonics*. Wiley: New York, **22** (1991).

105. A. D. Bristow, N. Rotenberg, and H. M. Van Driel, "Two-photon absorption and Kerr coefficients of silicon for 850–2200 nm". Applied Physics Letters **90**, 191104 (2007).

106. M. Born and E. Wolf, *Principles of optics: electromagnetic theory of propagation, interference and diffraction of light*. Elsevier (2013).

107. M. D. Young, J. J. Field, K. E. Sheetz, R. A. Bartels, and J. Squier, "A pragmatic guide to multiphoton microscope design". Advances in Optics and Photonics **7**, 276-378 (2015).

108. J. C. Mansfield and C. Peter Winlove, "A multi-modal multiphoton investigation of microstructure in the deep zone and calcified cartilage". Journal of Anatomy **220**, 405-416 (2012).

109. D. Oron, D. Yelin, E. Tal, S. Raz, R. Fachima, and Y. Silberberg, "Depth-resolved structural imaging by third-harmonic generation microscopy". Journal of Structural Biology **147**, 3-11 (2004).

110. R. Kumar, K. M. Grønhaug, C. L. Davies, J. O. Drogset, and M. B. Lilledahl, "Nonlinear optical microscopy of early stage (ICRS Grade-I) osteoarthritic human cartilage". Biomedical Optics Express **6**, 1895-1903 (2015).